

Ben-Gurion University of the Negev

Faculty of Engineering Sciences

Department of Mechanical Engineering



Rheological model for tumor cell progression and metastasis

Thesis submitted in partial fulfilment of
the requirements for the degree of
"MASTER OF SCIENCE"

By

Liav Daraf

UNDER THE SUPERVISION OF

Dr. Yuri Feldman

June 2022

Ben-Gurion University of the Negev
Faculty of Engineering Sciences
Department of Mechanical Engineering



Rheological model for tumor cell progression and metastasis

Thesis submitted in partial fulfilment of
the requirements for the degree of
"MASTER OF SCIENCE"

Submitted by:

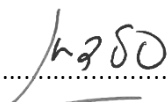
Liav Daraf

Supervised by:

Dr. Yuri Feldman

Author:


Date: 08/06/2022

Supervisor:


Date: 08/06/2022

Chairman of Graduate Studies Committee:

Date:

.....

June 2022

Abstract

Tumor cell progression and metastasis are complex phenomena, which involve ongoing molecular and cellular changes. Despite the significant progress made in the fundamental understanding of the biological and genetic events driving both phenomena, much remains to be elucidated regarding the influence of the tumor microenvironment on tumor initiation and progression as well as response to treatment. As such, the development of a theory correlating tumor cell progression and metastasis with biomechanical abnormalities in tumors and their microenvironment due to the continuous buildup of mechanical stresses may be viewed as a timely – and indeed urgent – need.

The main purpose of this study is to develop a realistic, physical, and multifunctional numerical tool, based on fluid mechanics and governed by the Navier-Stokes equations, that can be used to simulate different types of cancer cell dynamic scenarios and will provide mechanistic theory correlating complex biological phenomena with continuous rheological events within the colony of cancer cells.

By using the developed numerical tool, we propose a theory that provides a new insight into the mechanisms of the tumor development. The theory explains complex biological phenomena, such as the growth priorities given to individual cells during the tumor development in terms of minimizing the mechanic energy stored within the growing tumor. In addition, the performed study provides a new insight to the indistinct-choice-mechanism of the “leaders” and “followers” cells described in the literature by reconstructing the fingering structure typical of the tumor periphery, by only using the principle of minimization of the mechanical energy.

Acknowledgments

I would like to take this opportunity to express my immense gratitude to all those who have given their invaluable support and assistance. In particular, I am profoundly indebted to my supervisor, Dr. Yuri Feldman, for his professional and knowledgeable support in the physical, computational, and numerical fields. Especially, I would like to thank him for his endless patience and his close supervision during the writing of this presented scientific manuscript.

No less, I would like to thank my commander, LCDR Yuval Friedlander, for his support and patience.

Finally, my honest appreciation to my family and friends, for their spiritual support and encouragement along the way. Especially, to my partner, for her sacrifice and generosity.

Table of Contents

ABSTRACT	3
ACKNOWLEDGMENTS	4
TABLE OF CONTENTS.....	5
LIST OF FIGURES.....	7
LIST OF TABLES.....	9
LIST OF SYMBOLS	10
1. INTRODUCTION	12
2. THEORETICAL BACKGROUND	19
2.1. MODELING AN INDIVIDUAL CELL IN A DEVELOPING TUMOR.....	20
2.1.1. Individual cell growth	21
2.2. GOVERNING EQUATIONS	26
2.1.4. Normalizing a spring constant.....	28
2.2. NUMERICAL METHODS.....	29
2.2.1. Discrete Dirac delta function.....	29
2.2.2. Interpolation and regularization	30
2.2.3. SIMPLE scheme	31
2.2.4. Discretization using the finite volume method	32
2.2.5. Immersed boundary method (IBM)	35
2.2.6. Gradient decent	37
2.2.7. Two-phase flow model	37
3. VERIFICATION STUDY	44
3.1. LID-DRIVEN CAVITY FLOW.....	44
3.2. MOVING CYLINDER	50
3.3. GRADIENT DESCENT	52
3.4. TWO PHASE FLOW – DROP UNDER SHEAR FLOW	57
4. PARAMETRIC STUDY	59
4.1. RESOLUTION OF THE GRID	59

4.2.	CYTOKINESIS CALIBRATION	61
4.3.	CELL GROWTH CALIBRATION.....	62
4.4.	GOVERNING PARAMETERS	62
5.	VALIDATION STUDY, RESULTS, AND DISCUSSION	65
5.1.	AREA CONSERVATION AFTER THE CELL DIVISION	66
5.2.	THE CELL AREA DOUBLING TIME	66
5.3.	THE DURATION OF THE CYTOKINESIS PROCESS	67
5.4.	TIME EVOLUTION OF THE PROLIFERATION AND THE TUMOR AREA	68
6.	NUMERICAL DESIGN AND ANALYSIS OF THE BIOLOGICAL TISSUE.....	70
6.1.	TUMOR ENERGY RELAXATION	70
6.2.	NUMERICAL MODEL FOR THE CELL HETEROGENEITY	75
6.2.1.	Algorithm review	76
6.2.2.	Algorithm summary.....	80
6.2.3.	Results	81
6.3.	ENERGETIC PRIORITIZATION FOR MITOSIS INITIATION	89
7.	SUMMARY AND CONCLUSIONS.....	92
8.	BIBLIOGRAPHY	94

List of Figures

Figure 1.1 - Schematic description of metastasis process	13
Figure 1.2 - Digital images of cellular tissues obtained by agent-based models.....	17
Figure 2.1 - A schematic of a small cluster of 4 cells.....	19
Figure 2.2 - The computational domain with an arbitrary immersed boundary.....	21
Figure 2.3 – Singular Lagrangian source located in the geometric center of the cell	22
Figure 2.4 - Mitosis process	24
Figure 2.5 - Reconstruction of the cell boundary	25
Figure 2.6 - Adhesion links.	26
Figure 2.7 - The staggered grid used in the current solver.....	33
Figure 2.8 - Schematic description of two-phase configuration.	38
Figure 3.1 - Lid-driven cavity flow, physical model.	45
Figure 3.2 – Comparison of the presently obtained steady state values of velocity component in x direction	47
Figure 3.3 - Comparison of the presently obtained steady state values of velocity component in y direction.....	48
Figure 3.4 - Comparison between the results obtained on the uniform grid and on the non-uniform grid.....	49
Figure 3.5 - Uniform and non-uniform grids.....	49
Figure 3.6 – Maximum velocity divergence at each time step.....	50
Figure 3.7 - Moving cylinder: physical model.....	51
Figure 3.8 - Comparison between the time evolutions of drag coefficient	52
Figure 3.9 – Rearrangement of randomly distributed particles by the gradient decent algorithm for the open boundaries test case	54
Figure 3.10 - Rearrangement of randomly distributed particles by the gradient decent algorithm for the closed boundaries test case	55
Figure 3.11 - Rearrangement of randomly distributed particles by the gradient decent algorithm for the closed boundaries jammed test case	56
Figure 3.12 - Initial configuration of drop under shear stress	58
Figure 3.13 - A comparison between the final shape of the drop obtained by our simulations to an independent data	58

Figure 4.1 – Duration of the mitosis process as a function of grid resolution for different frequencies of reconstruction of the cell boundary points.	60
Figure 4.2 – The cytokinesis duration versus the contractile spring rigidity as obtained from the numerical simulations	62
Figure 4.3 – The duration of the cell area doubling versus the source strength.	62
Figure 5.1 – Tumor development, from its very early stage to a well-developed tumor containing 680 cells.	65
Figure 5.2 - Values of the daughter cell area measured immediately after division of the mother cell.....	66
Figure 5.3 - Time required for doubling of individual cells	67
Figure 5.4 - Time required for completing the cytokinesis process	68
Figure 5.5 - Time evolution of the proliferation and the tumor area	69
Figure 6.1 - Potential energy stored in a adhesive spring as a function of X_i-X_j	71
Figure 6.2 - Results obtained for the tissue consisting of 24 cells	74
Figure 6.3 - The rate of energy decrease and the rate of spatial expansion of the tumor versus number of cells entering the tumor.	75
Figure 6.4 - Comparison between the addition and the multiplication methodologies applied to the sources update	80
Figure 6.5 - Results yielded by a single activation of the algorithm for the tumor built of 232 cells	82
Figure 6.6 – Sample example for post-processing	84
Figure 6.7 – Average doubling time obtained for 8 different simulations at different locations within the tumor	85
Figure 6.8 – Visualization of the tissue fractional number with respect to a given partition.	86
Figure 6.9 – Relative part of mitotic cells per tissue area as a function of the distance from the center of the tumor	89
Figure 6.10 - Digital image of the tumor obtained using the mechanism of mitosis initiation based on ensuring the minimum increase in tumor kinetic energy	90

List of tables

Table 3.1 - Comparison of the values of velocity component in x direction obtained along vertical centerline of the cavity. The results were calculated on 160×160 uniform grid....	45
Table 3.2 - Comparison of the values of velocity component in y direction obtained along a horizontal centerline of the cavity. The results were calculated on uniform grid	46
Table 3.3 - Mass loss [%] at the obtained final drop shape.	58
Table 4.1 - Summary of parameters value and its normalizing factor	63

List of Symbols

Roman Letters	UNITS	Description
X	$[cm]$	Spatial coordinates of the immersed boundary
c	-	Coordinate along to the immersed boundary
t	$[s]$	Time
S	$\left[\frac{g}{s}\right]$	Singular fluid source
s	$\left[\frac{g}{s}\right]$	Distributed fluid source
h	$\left[\frac{1}{cm}\right]$	Grid size
x	$[cm]$	Spatial coordinate in the Eulerian grid
F	$[dyn]$	Singular Lagrangian force
f	$\left[\frac{dyn}{cm^3}\right]$	Body force vector
ℓ	$[cm]$	Spring free length
k	$\left[\frac{g}{cm \cdot s^2}\right]$	Spring rigidity
r_{adh}	$[cm]$	Adhesion connection range
u	$\frac{cm}{s}$	Fluid velocity vector
ρ	$\left[\frac{g}{cm^3}\right]$	Fluid density
p	$\left[\frac{dyn}{cm^2}\right]$	Pressure
μ	$\left[\frac{g}{cm \cdot s}\right]$	Fluid dynamic viscosity
\mathcal{R}	$\left[\frac{1}{cm^2}\right]$	Regularization \mathcal{R} operator
\mathcal{J}	$\left[\frac{1}{cm^2}\right]$	Interpolation operator

Greek Letters	Description
Γ	Interface of the immersed body
Ω	Computational domain
δ	Discrete Dirac delta function

1. Introduction

A distinctive feature of biological systems is their great ability to adjust themselves to their changing environment [1] [2]. Cellular tissues are subjected to a wide range of changes in their environmental condition during their lifetime. Those changes can be very slow, e.g., general increase in annual temperatures, periodically changing like day and night cycle, or rapidly and randomly changing e.g., unpredictable nutrient loading or unpredictable nutrient type [3]. The above changes are associated with several types of adaptative strategies, for example with increase or decrease in the number and size of tissue cells, change in the activities of pre-existing enzyme molecules [4], as well as complete change in their functionality which facilitates the survival of cells.

In addition to biochemical changes, cells are also subjected to changing mechanical environmental conditions. Experimental evidence shows that in a growing tumor, two different regions develop. One region is a dense and solid area within the center of the tumor, and the second is an invasive region at the outside boundaries of the tumor. The hypothesis is that when the cells in the dense area are stressed by their neighbors, due to a lack of space for them to grow, they start to divide at a smaller size compared to their mother cell (until they completely stop to grow and divide). As a tumor grows, cells in the invasive region may detach from the tumor and invade surrounding tissues.

The ability to adapt is a crucial feature of the mechanism of the progression of cancer tumors known as a process of metastasis [2]. Metastasis is a complex cell-biological event that involves continuous molecular and cellular changes in carcinoma cells as extensively reviewed in [5],[6]. During the metastasis, individual cells detach from their colonies, invade blood vessels, and start new colonies at different locations [7]. Through this process, the cells are subjected to a wide range of mechanical and biochemical changes in their micro-environment, many cells die during the invasion of the blood vessels due to a lethal deformation. It is now broadly recognized that cancer pathogenesis is characterized by the multistep progression of carcinomas, whose increased invasiveness depends on the activation epithelial to mesenchymal transition (EMT) [8-11].

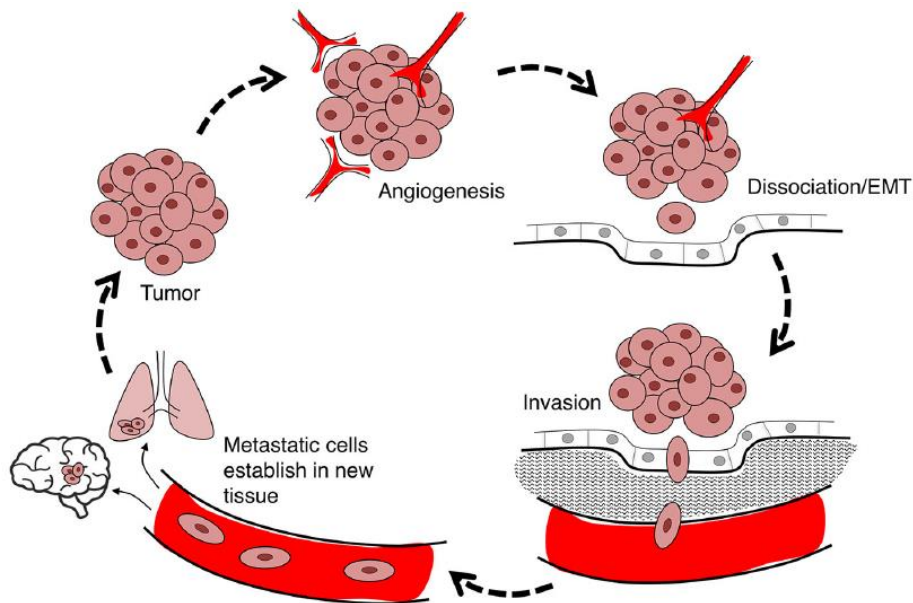


Figure 1.1 - Schematic description of metastasis process [7].

The epithelial is one out of the four types of biological tissues, it is the most common tissue in animals, and it is located at the outer surface of organs and blood vessels. Mesenchymal cells are mostly non-functional cells that can transform into different kinds of other tissues. The EMT involves loss of cell-to-cell adhesion, which enables the separation of an individual cell from its colony, and morphology changes which facilitates cell plasticity and amplifies its resistance to apoptosis and chemotherapies [2],[12]. EMT is typically characterized by elongation of the cell which benefits its cell invasion ability.

Despite a considerable progress achieved in the fundamental understanding of biological and genetic events governing tumor cell progression and metastasis, a mechanistic theory correlating both phenomena with a continuous buildup of mechanical stresses within the colony of cancer cells still does not exist. In light of the crucial roles that mechanosensing and mechanotransduction play in the regulation of cancer events, when closely cooperating with biochemical cues (such as $TGF-\beta$) [13], the development of such mechanistic theory is critical for gaining a comprehensive understanding of cancer pathogenesis. Specifically, the theory should allow for correlating formally the effect of continuous buildup of mechanical stresses within cell

tissue with onset and progression of EMT, as a key measure of metastatic potential of the cancer cell colony.

Quantifying the mechanical properties (i.e., normal and shear stresses) in active motile tissues is still an open problem. The apparent reason that this problem has not been resolved lies, first, in the large quantity of controversial experimental results acquired by using different experimental setups, namely, confined vs open systems, and second, in the large diversity of the measuring techniques used in experiments, resulting in different definitions of stresses and pressures.

For a confined system (i.e., a system whose rigid or elastic boundaries are in direct contact with the periphery of a cell colony), in vitro experiments show that dense cell cultures (in which all of the cells may be in contact) contain cells of different sizes [14-16], allowing to characterize the system by introducing cell size distribution function (SDF). Although the initial SDF narrows with the evolution of the cell colony, the relative dispersion (the ratio of the SDF dispersion to the mean cell area) remains substantial, thereby indicating the existence of cells characterized by a wide range of sizes and shapes, even at the end of an experiment [17]. As a result of this high scatter, it is difficult to pinpoint shape and deformation factors determining the EMT of specific cells.

In contrast, in an open system (i.e., a system whose rigid boundaries do not contact with the periphery of the cell colony and the boundary effect on the cell colony is negligible), the SDF indicates that the cells at the periphery are larger than those deep inside the colony [17]. It is commonly agreed [14] that most of the invasive post-EMT cells are located at the tissue periphery. These cells are more motile and are characterized by elongated shape compared to cancer cells from the same colony that have not undergone EMT.

Three different techniques are currently commonly used for determining the mechanical properties of tumor cells. The first is traction force microscopy (TFM), which is one of the most popular tools used for 'translating' deformations (both temporal and spatial) of soft substrates into the dynamic forces exerted by cells on substrates [18], [19]. For setups in which traction forces are balanced by intercellular interactions, the

measurements are typically supported by finite-element analysis, facilitating the building of stress maps characterizing the dynamical, heterogeneous landscape of both normal and shear stresses [18-21]. The TFM approach is based on the assumption that the cell layer can be treated as a continuum linear elastic material [19].

The second family of the methods focusing on the prediction of mechanical stresses within static cell tissues relies on advances in imaging techniques that provide a spatially resolved view of tissue development during morphogenesis, with visualization of the cell boundaries of 2D cell sheets [22], [23]. The technique is based on the assumption of mechanical equilibrium, from which the tensions along cell edges and pressures within each cell can be inferred from the cell configurations. Although the method is capable of resolving mechanical stresses at individual cell resolution, it provides only a “frozen,” i.e., stationary, distribution of mechanical stresses within the cell tissue and therefore cannot address temporal stress fluctuations arising from the non-equilibrium physics of the tissue.

The third category of commonly used methods utilizes homeostatic pressure as a quantitative metric for indicating the metastatic potential of a tumor [24]. The pressure is defined as the force per unit area that a confined tissue would exert on a moving piston permeable to fluid, and hence it represents an active osmotic cellular pressure. The method is thus applicable for highly non-equilibrium systems that break time-reversal symmetry [25]. In addition to the above methods, there are others that have been developed for measuring mechanical stresses in living tissues for both 2D and 3D geometries; these are based on the use of micro-pillar arrays [26], suspended monolayers [27],[28], laser ablation [29] as extensively reviewed in [30].

Despite the diversity of experimental methods available for the measurement of stresses within living tissues, there is no technique that may be regarded as universal—suitable for cells of any type or of any size. Therefore, there is a timely – and urgent – need to develop a reliable unified theoretical framework that can be easily calibrated against the experimental results produced by any of the above techniques. The major challenge in developing such a framework is to adequately model the interplay between individual cells of the tissue, while taking into account the biological complexity of the tissue and resolving the various scales involved. At present, there are two major families

of models for the numerical simulation of cells and tissue mechanics—continuum models and agent-based models. In models based on the continuum approach, the individual character of the cells is neglected, and the tissue dynamics is derived from mesoscopic or macroscopic conservation and constitutive laws. Therefore, the continuum approach is inapplicable of achieving the research objectives of the current study because it will not be able to produce a microscale observation over each individual cell. In contrast, agent-based models directly represent the cell itself, which positions them as natural candidates for investigating tissue dynamics by focusing on the interplay of individual cells. An extensive review of the state of the art of agent-based models is given in [31]. Here, we describe in brief two of the most popular agent-based models, namely, the deformable cell model (DCM) and the vertex model (VM), that are relevant to the current study.

The key idea of both the DCM and the VM is to enable modeling of the dynamics of cells of arbitrary shape and to give detailed information of the mechanical signals (tensile, contraction and shear forces) transmitted to the cell by the ECM via integrin receptors linked to the cell cytoplasm (the material within the cell, excluding the nucleus) and cytoskeleton (microscopic network of protein filaments and tubules in the cytoplasm). In the DCM, the cell body is discretized by a number of nodes, which are connected by viscoelastic elements interacting via pairwise functions, typically (but not necessarily) represented by linear springs. The whole tissue is modeled by interconnecting individual cells, which is, again, implemented by introducing linear springs. The forces in the DCM originate from both cell–cell interactions and intracellular interactions as modeled by elastic springs and viscous dissipation of the momentum governed by incompressible Navier Stokes (NS) equations, which govern global cell properties such as cell volume and surface area [32-34]. The VM [35-37], with its recently modified self-propelled Voronoi version [38-39], differs from the DCM in the ways the cell boundaries are constructed for static tissues and then later relocated when modeling motile tissues. In VM, the tissues are constructed on the basis of a polygonal tessellation (typically Voronoi), while the transport of every individual cell in the tissue is governed by a balance of junctional tensions and pressure differences.

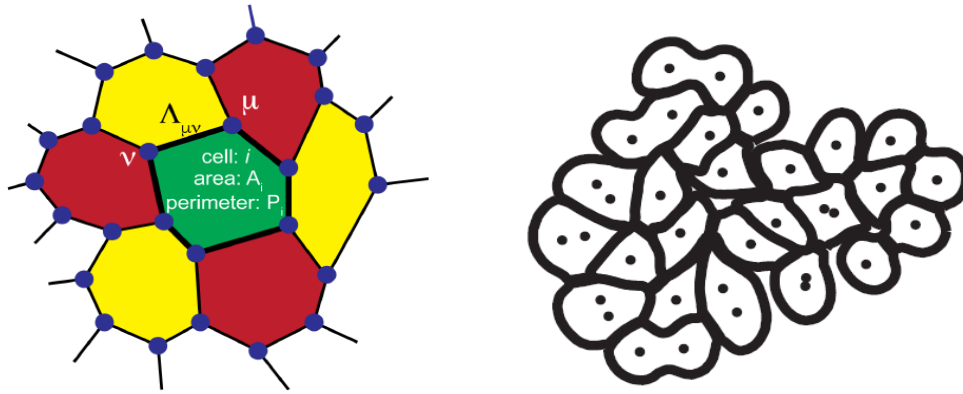


Figure 1.2 - Digital images of cellular tissues obtained by agent-based models. (a) VM model. (b) DCM.

Generally speaking, both the DCM and the VM are applicable for the objectives of the proposed study because: they are both suitable for tightly packed cell ensembles with small intercellular spaces; they can both incorporate spatial and temporal deformations of the tissue and of cell-cell adhesion; and they can both be generalized – with a reasonable computational effort – to account for cell proliferation, apoptosis (a type of cell death), and polarization. The main disadvantage of the VM is that it requires intensive tuning and calibration with experimental results to provide physically correct results, including explicit introducing and tuning of the area conservation constant and the non-trivial procedure of adapting spring force parameters to macroscopic constants [40]. This drawback makes parameter sensitivity analysis very constrained and results in very tedious parameter inference. In contrast, the DCM is intrinsically based on the solution of continuity and NS equations and thus automatically satisfies the conservation of mass and momentum within a tissue. In addition, in the DCM, the cell dynamics is typically implemented by the well-established interface tracking approach [41], and, most importantly, the model is governed solely by the Reynolds number and the source intensity, which determine the viscous dissipation of momentum and the rate of the cell growth, respectively. The calibration of the model to the experimental results is quite straightforward and requires only fitting of the source strength to the whole process of mitosis (cell division) and of the division spring constant to the duration of cytokinesis (cytoplasmic division of a cell at the end of mitosis), see e.g., [32],[33]. The drawback of using this model derives from the need to solve the full system of NS equations, which has – until now – restricted the application of the DCM to the analysis of tissues consisting of only a few hundreds of cells.

As follows from the above review the need of developing unified reliable theoretical framework, capable of convenient calibration with experimental results provided by any of existing techniques is extremely timely and is the first goal of the current study. The second goal of the current study is to use the developed framework to substantiate the hypothesis that connects the purely mechanistic characteristics of the tumor with its further proliferation and development. At the first stage the focus is on developing DCM based on the principles of fluid mechanics and validating the developed model by comparing the obtained results with quantitative characteristics available in the literature, including cell growth time, mass conservation after cell division, duration of cytokinesis, and overall rate of tumor progression. For the above tests relationships will be established between parameters that control cell growth and cytokinesis and between constitutive forces introduced to model the physiological behavior of tumor tissue.

After the developed theoretical and numerical methodologies are extensively validated, we turn to the second goal of the current study. In particular, the focus is on numerical replication and investigation of the size distribution function (SDF) and the fingering structure, characterizing the invasive region of a developing tumor. We hypothesize and provide theoretical evidence that in addition to chemical and genetic events, basic mechanical principles such as minimum mechanical energy may determine the development and progression of tumor tissue. It is believed that the currently performed study will contribute to a more comprehensive understanding of the mechanisms responsible for the tumor cell progression and metastasis.

2. Theoretical Background

This chapter presents the basic model of the cell's proliferation, including the main outlines and the mathematical formulation of the model which are explained in detail. The basic model, as introduced for the first time by Rejniak [32] consists of individual cells and discrete sources. The cells are filled and surrounded by Newtonian, incompressible and homogenous fluid. The discrete sources, responsible for the cell's growth, are placed within geometric center of the cells. Surface tension, division, and microenvironment mechanosensing of the cells are modelled by introducing additional forces individually computed for any given configuration of the cell's cluster. The presented modeling does not take into account the structure of cell cytoskeleton within the cell membrane, and therefore stresses and deformations transport through the cell only by the momentum diffusion and the mass conservation mechanisms.

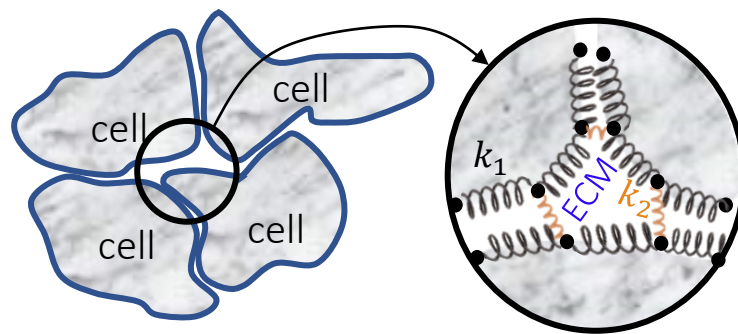


Figure 2.1 - A schematic of a small cluster of 4 cells. The cell boundary determined by a series of discrete points (black circles) connected by preloaded linear springs of stiffness coefficient k_1 . Separate cells are connected by the adherent links modelled by linear springs of stiffness coefficient k_2 . The cell cytoplasm enclosed by the plasma membrane as well as the ECM are modelled as a viscous incompressible homogeneous Newtonian fluid.

Biological tissues are well known for their viscoelastic stress-strain relation. Therefore, when aiming to study rheological behavior for biological tissues, introducing the viscoelastic properties is critical for capturing the realistic physics. As described above, the presented model incorporates series of linear springs embedded within a Newtonian fluid. This approach provides the overall linear viscoelastic behavior of the simulated tissue at the

mesoscale level. Although real tissues show a power-law viscoelastic behavior, we believe that at the current stage of this research a linear behavior provides reliable results.

Mitotic individual cells within the tumor significantly contribute to the tumor progression. The mitosis process refers to the growth and further division of an individual mother cell into two daughter cells. To mimic accurately the experimental observations corresponding to the beginning of tumor growth (i.e., small tumors), characterized by only a small fraction of the tumor cells dividing at any given time [42], the presently developed model has adopted the strategy of initiating a mitosis process every 10 minutes in a single randomly selected cell. In this model mitosis initiation includes activation of a fluid source, attached to the geometric center of the cell, and causes membrane expansion of the cell. Meanwhile, the cells not yet involved into mitosis preserve their volume while contributing to the adjacent microenvironment by exerting adhesive and surface tension forces.

Utilizing the above strategy, as proposed by Rejniak [1], provides a random orientation of the growing direction and irregular outline of the tumor, which would otherwise have grown symmetrically acquiring a close to spheroidal shape due to the lack of external constraints. We further extend this basic model while proposing considerations based on the minimization of mechanical energy stored within the tumor as a criterion for mitosis initiation and growth rate.

2.1. Modeling an individual cell in a developing tumor

The basic model presented in this study is inspired by the model previously formulated by Rejniak [32] based on fundamental principles of fluid mechanics and the immersed boundary method (IBM). The model is governed by the N-S equations for Newtonian, incompressible fluid. The membrane of each individual cell is modelled by a series of points immersed within the fluid. In accordance with the IBM formalism, the interaction of each individual cell with the surrounding environment, as well as the cytokinesis events (i.e., activation of contractile forces for cell division) are implemented by applying external forces at each point of the cell boundary. The forces are calculated by employing the stress-strain constitutive relation for linear springs.

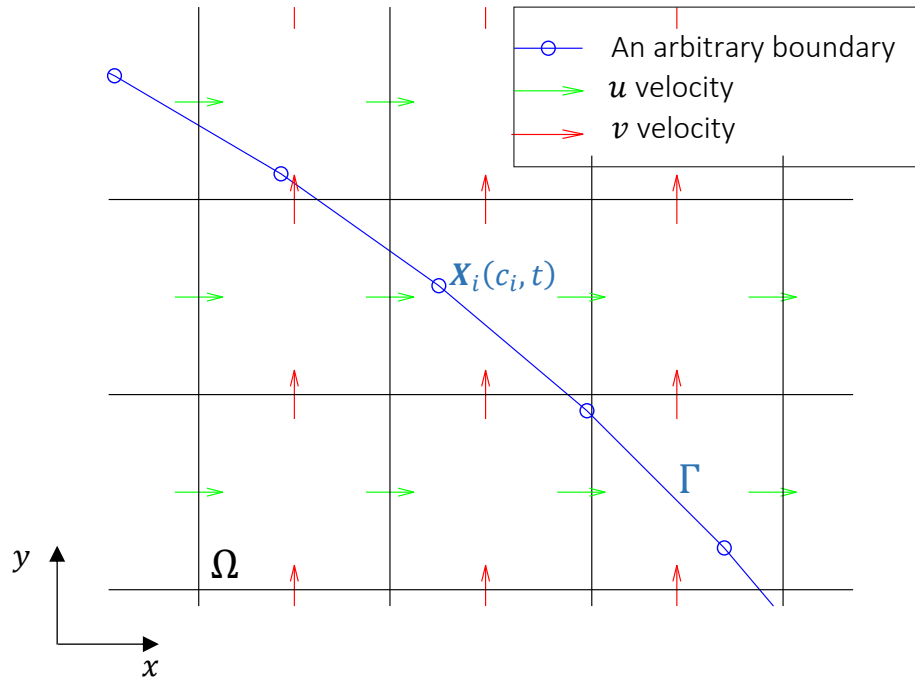


Figure 2.2 - The computational domain Ω (for the fluid velocity) with an arbitrary immersed boundary Γ determined by the series of boundary points $\mathbf{X}_i(c_i, t) = [x_i(c_i, t), y_i(c_i, t)]$, where c is a coordinate along the curve Γ and t is time.

2.1.1. Individual cell growth

The growth of individual cell is modelled by embedding a singular fluid-source within the cell membrane to result in expansion of the cell (see Figure 2.3). The source is implemented by a single Lagrangian point located in the geometric center of each cell. Note that during the cell growth the cell membrane changes its shape by expanding and moving with the velocity equal to that of the surrounding fluid, so that also the location of the geometric center of the cell moves. It is also noteworthy that as a result of the cell membrane expansion, the cell surface area (the cell perimeter for 2D configuration) increases. Thus, in accordance with the limitations implied by the IBM, the series of the cell boundary points must be reconstructed during the simulations in order to preserve an even spacing (needs to be approximately equal to the grid step h .) between the adjacent points (Figure 2.5).

In order to solve the NS equations, the source strength S is smeared from the Lagrangian point onto the underlying Eulerian grid. In practice, the discrete Dirac delta function is used for this purpose as will be explained in detail in section 2.2.1. The impact of a singular Lagrangian source on the Eulerian surrounding is calculated as follows:

$$s(\mathbf{x}, t) = \sum_{\Omega} S \delta^2(\mathbf{x} - \mathbf{x}_s) \quad (2.1)$$

Where s reads for the distributed Eulerian source, \mathbf{x} is a coordinate on the Eulerian grid, S is a singular Lagrangian source, $\delta^2(\mathbf{r})$ is the two-dimensional discrete delta function and \mathbf{x}_s is the Lagrangian coordinate of the source.

In this basic model, that will be extended in the following chapters, the source magnitude is binary, i.e., it depends on whether the cell is growing or not:

$$S = \begin{cases} S_{mitosis} & \text{the cell is growing} \\ 0 & \text{the cell is currently not growing} \end{cases} \quad (2.2)$$

The decision regarding which cell will start to grow next is made randomly, i.e., every 10 minutes a random cell is chosen to start its mitosis.

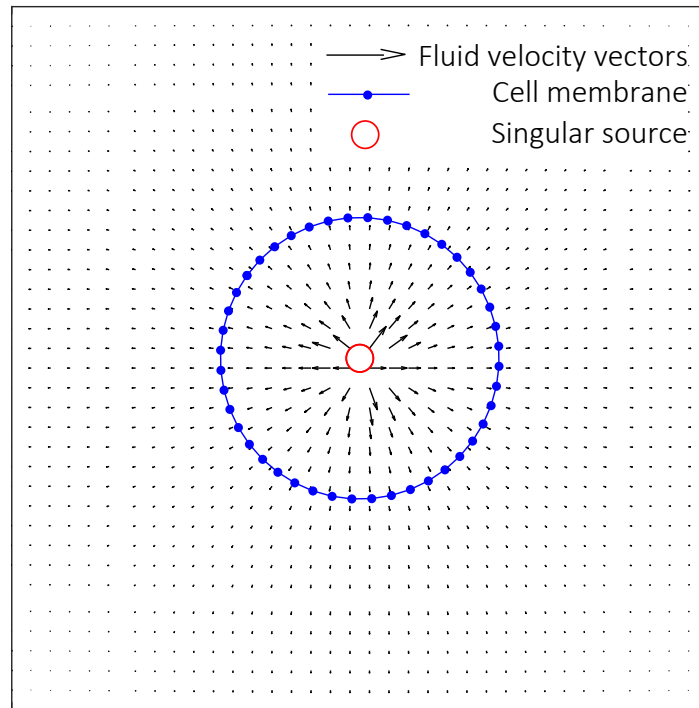


Figure 2.3 – Singular Lagrangian source located in the geometric center of the cell. The source and the cell are immersed within Newtonian incompressible fluid.

2.1.1. Surface tension

In the current model it was assumed that the physical properties of the ECM and cell cytoskeleton are close to each other. Yet, surface tension force should be considered to model the interaction between the two phases. The surface tension force is modeled by introducing linear springs connecting two adjacent points of the cell membrane.

The mathematical formulation of the surface tension forces is based on Hooke's law:

$$\mathbf{F}_{ST}(\mathbf{X}_{c_2}, t) = k_{ST} \frac{\mathbf{X}(c_1, t) - \mathbf{X}(c_2, t)}{\|\mathbf{X}(c_1, t) - \mathbf{X}(c_2, t)\|} (\|\mathbf{X}(c_1, t) - \mathbf{X}(c_2, t)\| - \ell_{ST}) \quad (2.3)$$

When $\mathbf{X}(c_i, t)$ is a boundary point on the cell membrane, k_{ST} is the rigidity of linear spring, ℓ_{ST} is the spring free length and $\mathbf{F}_{ST}(c_2, t)$ is the Lagrangian force acting at point $\mathbf{X}(c_2, t)$ playing the role of surface tension force acting between the cell membrane and the extracellular matrix.

Following the IBM formalism the Lagrangian, surface tension force is smeared to the underlying Eulerian grid, by utilizing the discrete Dirac delta function:

$$\mathbf{f}_{ST}(\mathbf{x}, t) = \sum_{\Omega} \mathbf{F}_{ST}(\mathbf{X}_{c_i}, t) \delta^2(\mathbf{x} - \mathbf{X}_{c_i}) \quad (2.4)$$

When \mathbf{f}_{ST} is the distributed surface tension force, \mathbf{x} is a coordinate on the Eulerian grid, \mathbf{F}_{ST} is the Lagrangian surface tension force, $\delta^2(\mathbf{r})$ is the two-dimensional discrete Dirac delta function and \mathbf{X}_{c_i} is the Lagrangian coordinate at which the surface tension force is applied.

2.1.2. Cell cytokinesis

The process of the cell division (cytokinesis), in course of which a single mother cell splits into two separate daughter cells is modeled in three steps: first, at a certain point the singular source is split into two separate sources, each characterized by a flow rate value, which is half of the flow rate of the original source (at this current study we chose to model a symmetric division). We chose to perform the source separation when the cell expands to 160% of its initial size in order to enable the sources enough time to polarize the cell before it doubles its size. The two sources are placed within the cell along its longest axis. In this step the mother cell is polarized which models the polarization process typical of the realistic biological cells in course of which the genetic code is replicated into

two counter poles right before the cell division [43]. The second step initiates after the cell doubles its size – the sources turn off and a contractile ring, attached to the cell membrane, shrinks the cell membrane [43]. This step is modeled by introducing a series of linear springs attached to the cell membrane along the shortest axis of the cell and creating a cleavage furrow that partitions the cell into two lobes. Finally, when the two sides of the cell that connected with the linear springs are close enough to each other (3 grid steps), the mother cell is divided into two daughter cells (Figure 2.4).

The mathematical formulation of the contractile forces is based on the Hooke's law:

$$\mathbf{F}_{cyto}(\mathbf{X}_{c_2}, t) = k_{cyto} \frac{\mathbf{X}(c_1, t) - \mathbf{X}(c_2, t)}{\|\mathbf{X}(c_1, t) - \mathbf{X}(c_2, t)\|} (\|\mathbf{X}(c_1, t) - \mathbf{X}(c_2, t)\| - \ell_{cyto}), \quad (2.5)$$

where $\mathbf{X}(c_i, t)$ is a boundary point of the dividing cell, k_{cyto} is the spring rigidity, ℓ_{cyto} is the spring free length and $\mathbf{F}_{cyto}(\mathbf{X}_{c_2}, t)$ is the Lagrangian contractile force acting at point $\mathbf{X}(c_2, t)$.

Following the IBM formalism, the contractile force is smeared to the underlying Eulerian grid, by utilizing discrete Dirac delta function:

$$\mathbf{f}_{cyto}(\mathbf{x}, t) = \sum_{\Omega} \mathbf{F}_{cyto}(\mathbf{X}_{c_i}, t) \delta^2(\mathbf{x} - \mathbf{X}_{c_i}) \quad (2.6)$$

where \mathbf{f}_{cyto} is the distributed force, \mathbf{x} is a coordinate on the Eulerian grid, \mathbf{F}_{cyto} is contractile Lagrangian force, $\delta^2(\mathbf{r})$ is two-dimensional delta function and \mathbf{X}_{c_i} is the Lagrangian coordinate at which the contractile force is applied.

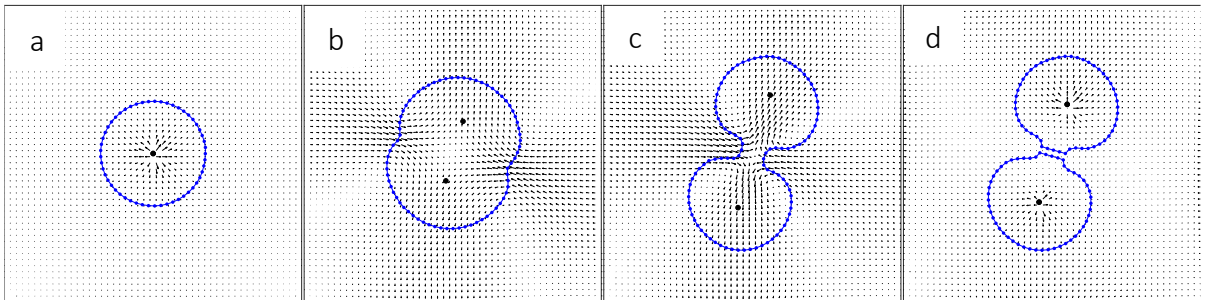


Figure 2.4 - Mitosis process. (a) growth of an individual cell, modeled by a single source placed in the geometrical center of the cell; (b) initiating of cytokinesis process for cell that has doubled its size. The cytokinesis is modeled by an activation of a division spring tied up to two opposite boundaries of the cell; (c) final contour of the cell at the end of cytokinesis process prior to its division; (d) two daughter cells at the end of the mitosis process.

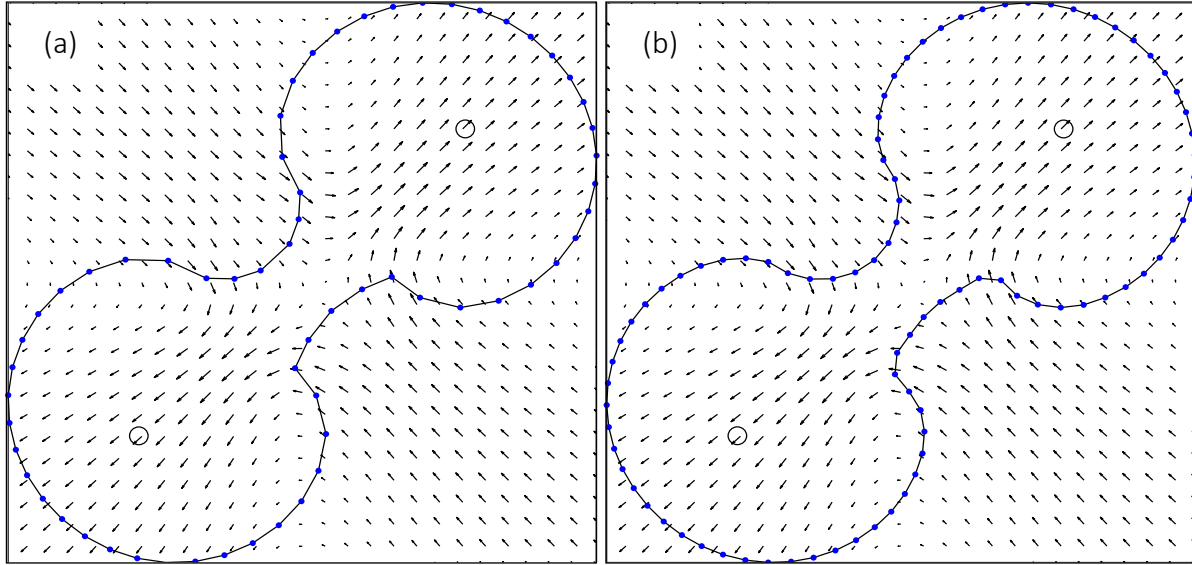


Figure 2.5 - Reconstruction of the cell boundary. In course of cytokinesis the surface area (perimeter) of the cell increases. As a result, a reconstruction procedure should be activated in order to preserve even spaces, approximately equal to the grid step h , between two adjacent points as a requirement for correct interpolation and smearing procedures implemented by utilizing the discrete Dirac delta function being the part of IBM: (a) before the reconstruction, average distance between two adjacent points is $1.4341h$; (b) after the reconstruction, average distance between two adjacent points is $1.0076h$.

2.1.3. Cell-to-cell adhesion

Adhesion forces connecting the given cell with the nearby cells play a key role in the mechanosensing of the cell with its micro-environment. In this model, the adhesion links are modeled as a linear spring that connects between boundary points of the neighbor cells. Our algorithm allows only for a single connection for each boundary point at a time, while the connection is created between the two closest points as long as they are located within the connection range r_{adh} equal to 3 grid steps (Figure 2.6). Reconnections are made each time the configuration of the boundaries changes significantly, for example, after cell division or during cytokinesis.

The adhesion forces are calculated by utilizing the linear spring formulation:

$$\mathbf{F}_{adh}(\mathbf{X}_{c_2}, t) = k_{adh} \frac{\mathbf{X}(c_1, t) - \mathbf{X}(c_2, t)}{\|\mathbf{X}(c_1, t) - \mathbf{X}(c_2, t)\|} (\|\mathbf{X}(c_1, t) - \mathbf{X}(c_2, t)\| - \ell_{adh}) \quad (2.7)$$

where $\mathbf{X}(c_i, t)$ is a Lagrangian boundary point of one of the two neighbor cells, k_{adh} is the spring rigidity, ℓ_{adh} is the spring free length (equal to $1.9h$) and $\mathbf{F}_{adh}(c_2, t)$ is the Lagrangian adhesion force acting at point $\mathbf{X}(c_2, t)$.

Following the IBM formalism, the Lagrangian adhesion force is smeared to the underlying Eulerian grid, by utilizing discrete Dirac delta function:

$$f_{adh}(\mathbf{x}, t) = \sum_{\Omega} \mathbf{F}_{adh}(\mathbf{X}, t) \delta^2(\mathbf{x} - \mathbf{X}), \quad (2.8)$$

where \mathbf{f}_{adh} is the distributed force, \mathbf{x} is a coordinate on the Eulerian grid, \mathbf{F}_{adh} is the Lagrangian adhesion force, $\delta^2(r)$ is two-dimensional Discrete delta function and X is the Lagrangian coordinate of the Lagrangian force

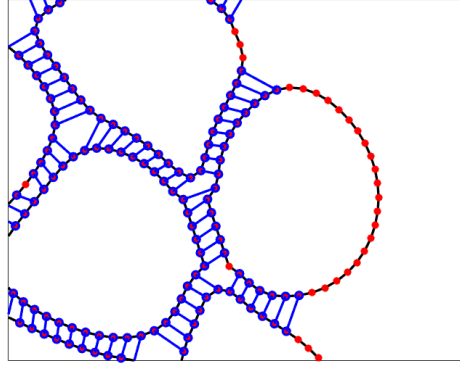


Figure 2.6 - Adhesion links.

2.2. Governing equations

The governing equations for the incompressible Newtonian fluid with source term added for the implementation of the cell growth [44] are given by:

$$\rho \left(\frac{\partial \mathbf{u}}{\partial t} + \nabla \cdot (\mathbf{u}\mathbf{u}) \right) = -\nabla p + \mu \nabla^2 \mathbf{u} + \frac{\mu}{3\rho} \nabla s + \mathbf{f}, \quad (2.9)$$

$$\rho \nabla \cdot \mathbf{u} = s, \quad (2.10)$$

where $\rho \left[\frac{gr}{cm^3} \right]$ is the fluid density, $\mathbf{u} \left[\frac{cm}{s} \right]$ is the fluid velocity, $p \left[\frac{dyn}{cm^2} \right]$ is the pressure field, $\mu \left[\frac{gr}{cm \cdot s} \right]$ is the fluid dynamic viscosity and $s \left[\frac{g}{cm^3 \cdot s} \right]$ is the volumetric flow rate source.

Eq's. (2.9) and (2.10) are normalized by using the characteristic scales for length, time, velocity, volumetric flow rate source, pressure, and force respectively:

$$\begin{aligned}
x &= \bar{x} \cdot L & t &= \tau \cdot T & \mathbf{u} &= \bar{\mathbf{u}} \cdot U & s &= \bar{s} \cdot S & p &= \bar{p} \cdot P \\
\mathbf{f} &= \bar{\mathbf{f}} \cdot F
\end{aligned} \tag{2.11}$$

Plugging these expressions back into the momentum equation (2.9) gives:

$$\rho \left(\frac{\partial \bar{\mathbf{u}}}{\partial \tau} \cdot \frac{U}{T} + \nabla \cdot (\bar{\mathbf{u}}\bar{\mathbf{u}}) \cdot \frac{U^2}{L} \right) = -\nabla \bar{p} \cdot P \cdot \frac{1}{L} + \mu \nabla^2 \bar{\mathbf{u}} \cdot \frac{U}{L^2} + \frac{\mu}{3\rho} \nabla \bar{s} \cdot \frac{S}{L} + \bar{\mathbf{f}} \cdot F, \tag{2.12}$$

and after rearrangement:

$$\frac{\partial \bar{\mathbf{u}}}{\partial \tau} + \nabla \cdot (\bar{\mathbf{u}}\bar{\mathbf{u}}) \cdot \frac{UT}{L} = -\nabla \bar{p} \cdot P \cdot \frac{T}{\rho UL} + \nabla^2 \bar{\mathbf{u}} \cdot \frac{\mu T}{\rho L^2} + \frac{\mu}{3\rho} \nabla \bar{s} \cdot \frac{TS}{\rho UL} + \bar{\mathbf{f}} \cdot F \cdot \frac{T}{\rho U} \tag{2.13}$$

Using the identity:

$$T \equiv \frac{L}{U} \tag{2.14}$$

$$[S] = \left[\frac{\rho}{T} \right] = \left[\frac{\rho U}{L} \right] \tag{2.15}$$

in Eq.(2.13) yields:

$$\begin{aligned}
\frac{\partial \bar{\mathbf{u}}}{\partial \tau} + \nabla \cdot (\bar{\mathbf{u}}\bar{\mathbf{u}}) &= -\nabla \bar{p} \cdot P \cdot \frac{1}{\rho U^2} + \nabla^2 \bar{\mathbf{u}} \cdot \frac{\mu}{\rho UL} + \frac{\mu}{3\rho} \nabla \bar{s} \cdot S \cdot \frac{1}{\rho U^2} \cdot \frac{L}{L} + \bar{\mathbf{f}} \cdot F \\
&\cdot \frac{L}{\rho U^2}
\end{aligned} \tag{2.16}$$

Whereas the non-dimensional momentum equation reads:

$$\frac{\partial \bar{\mathbf{u}}}{\partial \tau} + \nabla \cdot (\bar{\mathbf{u}}\bar{\mathbf{u}}) = -\nabla \bar{p} + \frac{1}{Re} \left(\nabla^2 \bar{\mathbf{u}} + \frac{1}{3} \nabla \bar{s} \right) + \bar{\mathbf{f}}, \tag{2.17}$$

and the non-dimensional continuity equation is rewritten as:

$$\nabla \cdot \bar{\mathbf{u}} = \bar{s}, \tag{2.18}$$

where the non-dimensional scales for the rate of volumetric source, pressure, force density and velocity are:

$$S = \frac{\rho U}{L} \quad P = \rho U^2 \quad F = \frac{\rho U^2}{L} \quad U = \frac{L}{T}. \tag{2.19}$$

Here T and L are the characteristic time and length typical of the given physical phenomenon.

2.1.4. Normalizing a spring constant

Some of the forces that are utilized in the mathematical model are modeled by spring with a stiffness coefficient $k \left[\frac{g}{cm \cdot s^2} \right]$, which must be normalized consistently with the characteristic scales given above.

Recalling that:

$$\mathbf{f} = \mathcal{R}(k\Delta l\Delta s) = k \left[\frac{g}{cm \cdot s^2} \right] \Delta l [cm] \Delta s [cm] \frac{1}{h^2} \left[\frac{1}{cm^2} \right] \cdot \frac{1}{1 [cm]} \delta^2 \left(\frac{x - x_0}{h} \right), \quad (2.20)$$

where \mathcal{R} is the regularization operator (will be explained in detail in section 2.2.2), Δl is the spring elongation, Δs is the surface area to which the force is applied (for 2D configuration Δs is approximately equal to the grid step due to the limitations imposed by the IBM as will be explained in detail in 2.2.5) h is the grid spatial step and δ^2 is the two-dimensional discrete Dirac delta function.

Note that the expression $k\Delta l\Delta s$ is a resultant force having a unit [dyn], and needs to be converted to the volumetric force (or the force density) to be consistent with the units of NS equations, i.e., $\left[\frac{dyn}{cm^3} \right]$. The conversion is made by employing the regularization operator implemented by utilizing the two-dimensional Dirac delta function of unit $\left[\frac{1}{cm^2} \right]$ which for the 2D configuration should be additionally multiplied by a unit length of $\left[\frac{1}{cm} \right]$.

The following procedure is applied when normalizing the force:

$$\bar{\mathbf{f}} = \mathcal{R}(\bar{k}\bar{\Delta l}\bar{\Delta s}) = \bar{k} \frac{\Delta l}{L} \frac{\Delta s}{L} \cdot \frac{1}{h^2/L^2} \cdot \frac{1}{1/L} \cdot \delta^2 \left(\frac{x - x_0}{h} \right) \quad (2.21)$$

Then using the scaling factor determined in Eq. (2.19) the force is rendered non-dimensionally as:

$$\bar{\mathbf{f}} = \mathbf{f} \frac{L}{\rho U^2},$$

which leads to:

$$\bar{k} \frac{\Delta l \Delta s}{L L} \cdot \frac{1}{h^2/L^2} \cdot \frac{1}{1/L} \cdot \phi^2 \left(\frac{x - x_0}{h} \right) = k \left[\frac{g}{cm \cdot s^2} \right] \Delta l [cm] \Delta s [cm] \frac{1}{h^2} \left[\frac{1}{cm^2} \right] \cdot \frac{1}{1 [cm]} \phi^2 \left(\frac{x - x_0}{h} \right) \frac{L}{\rho U^2} \quad (2.22)$$

$$\bar{k} \frac{11}{L L} \cdot \frac{L^2}{1} L = k \left[\frac{g}{cm \cdot s^2} \right] \cdot \frac{1}{1 [cm]} \frac{L}{\rho U^2} \quad (2.23)$$

$$\bar{k} = k \left[\frac{g}{cm \cdot s^2} \right] \cdot \frac{1}{\rho U^2} \left[\frac{cm \cdot s^2}{g} \right]. \quad (2.24)$$

Therefore, the scaling factor of the spring stiffness K is given by:

$$K = \rho U^2 \quad (2.25)$$

2.2. Numerical methods

In this chapter, the methodology used for the solution of the governing equations will be explained in detail. In general, an exact analytical solution for the Navier-Stokes equation can be performed only for a few simplified cases and geometries. Therefore, we use numerical methods to solve the governing equations.

The standard second order finite volume method and second order backward finite difference are utilized to discretize the governing equations in space and time, respectively. The SIMPLE (Semi-Implicit Method for Pressure-Linked Equations) approach [45] is utilized for the pressure-velocity coupling. For the representation of complex moving cell geometry, we use the IBM, which was originally introduced by Peskin [46] in order to simulate a blood flow through the heart. This method allows to use a regular Eulerian grid whereas the impact of the cell boundaries on the surrounding flow is introduced by smearing the Lagrangian forces acting at the Lagrangian points onto the Eulerian grid by utilizing the discrete Dirac delta function.

2.2.1. Discrete Dirac delta function

In order to smear the Lagrangian forces or the volumetric flow rate source from a Lagrangian to Eulerian grid, we chose a discrete Dirac delta function supported over 3 cells. This delta function is commonly used in simulations using IBM [47] and gained its popularity

for being specifically designed for staggered grids. In 2D configurations the delta function is defined as a multiplication of two one-dimensional delta functions:

$$\delta_h^2(\mathbf{x} - \mathbf{x}_0) = \delta_h^1(x - x_0)\delta_h^1(y - y_0), \quad (2.26)$$

where h is the grid step, and:

$$\delta_h^1(x - x_0) = \frac{1}{h}\phi\left(\frac{x - x_0}{h}\right), \quad (2.27)$$

and $\phi(r)$ is a continuous function:

$$\phi(r) = \begin{cases} \frac{1}{3}(1 + \sqrt{-3r^2 + 1}) & |r| \leq 0.5 \\ \frac{1}{6}(5 - 3|r| - \sqrt{-3(1 - |r|)^2 + 1}) & 0.5 \leq |r| \leq 1.5 \\ 0 & \textit{otherwise} \end{cases} \quad (2.28)$$

There are also other options for choosing $\phi(r)$, as long as they meet a number of basic requirements:

- a. $\phi(r)$ is continuous for all real numbers r .
- b. $\phi(r) = 0, |r| \geq n\left(\frac{x-x_0}{h}\right)$, n is a number of grid cells (may be a fraction).
- c. $\sum_i \phi(r - i) = 1, \forall r$
- d. $\sum_i (r - i)\phi(r - i) = 0, \forall r$
- e. $\sum_i [\phi(r - i)]^2 = \frac{1}{2}, \forall r$

when all the sums are performed for the integers, i such that $-\infty < i < \infty$. Note that being i an integer number implies that the distance between each pair of adjacent Lagrangian points should be equal, i.e., all the Lagrangian points determining the surface of the immersed body should be equally spaced.

2.2.2. Interpolation and regularization

By utilizing the discrete Dirac delta function, we define two conjugate operators, namely, the interpolation \mathcal{I} and regularization \mathcal{R} operators. The interpolation operator is used to interpolate data from the Eulerian to Lagrangian points and is formulated as:

$$C(\mathbf{X}) \equiv \mathcal{I}(\mathbf{X}, c(\mathbf{x})) \equiv \sum_{\Omega} c(\mathbf{x}) \delta_h^2(\mathbf{x} - \mathbf{X}), \quad (2.29)$$

where C is the quantity interpolated to the Lagrangian point, \mathbf{X} is the coordinate of the Lagrangian point, c is the corresponding quantity determined on the Eulerian grid, \mathbf{x} is the Eulerian grid coordinate, Ω is the computational domain, and δ_h^2 is the two-dimensional discrete delta function.

The regularization operator smears the data from the Lagrangian to the Eulerian grid and is formulated as:

$$c(\mathbf{x}) \equiv \mathcal{R}(\mathbf{X}, C(\mathbf{X})) \equiv \sum_{\Gamma} C(\mathbf{X}) \delta_h^2(\mathbf{x} - \mathbf{X}), \quad (2.30)$$

where C is the quantity determined in the Lagrangian point, \mathbf{X} is the coordinate of Lagrangian point, c is the corresponding quantity determined on the Eulerian grid, \mathbf{x} is the Eulerian grid coordinate, Γ is the immersed boundary, and δ_h^2 is the two-dimensional discrete delta function.

2.2.3. SIMPLE scheme

In order to perform solution of the system of governing equations, we utilize the SIMPLE algorithm [45]. According to the SIMPLE formalism, coupling between the pressure and the velocity fields is implemented in two steps: the first step is a predictor approximation of the velocity field via the momentum equation (using the pressure computed in the previous time step); the second step includes correction and projection procedures, correcting the pressure field obtained by the solution of Poisson equation derived from the continuity equation and projecting the predicted non-solenoidal velocity on the divergence-free subspace.

Consider the non-dimensional system of N-S and the continuity equations (the focus is on the reduced form of Eq's. (2.17) and (2.18) without the source terms):

$$\frac{\partial \mathbf{u}}{\partial \tau} + \nabla \cdot (\mathbf{u}\mathbf{u}) = -\nabla p + \frac{1}{Re} \nabla^2 \mathbf{u} \quad (2.31)$$

$$\nabla \cdot \mathbf{u} = 0 \quad (2.32)$$

The non-solenoidal approximated velocity, \mathbf{u}^* , is obtained by solving the momentum equation while taking the pressure field and the non-linear terms as known from the previous time step:

$$\frac{\mathbf{u}^* - \mathbf{u}^n}{\Delta\tau} + \nabla \cdot (\mathbf{u}\mathbf{u})^n = -\nabla p^n + \frac{1}{Re} \nabla^2 \mathbf{u}^* \quad (2.33)$$

Assuming that the velocity \mathbf{u}^{n+1} is the solution for the Eq. (2.31) at the next time step:

$$\frac{\mathbf{u}^{n+1} - \mathbf{u}^n}{\Delta\tau} + \nabla \cdot (\mathbf{u}\mathbf{u})^n = -\nabla p^{n+1} + \frac{1}{Re} \nabla^2 \mathbf{u}^* \quad (2.34)$$

We can next subtract Eq. (2.33) from Eq. (2.34) to obtain:

$$\frac{\mathbf{u}^{n+1} - \mathbf{u}^*}{\Delta\tau} = -\nabla(p^{n+1} - p^n) \equiv -\nabla p' \quad (2.35)$$

Taking the divergence from both sides of Eq.(2.35) yields:

$$\frac{1}{\Delta\tau} (\nabla \cdot \mathbf{u}^{n+1} - \nabla \cdot \mathbf{u}^*) = -\nabla^2 p' \quad (2.36)$$

Next by utilizing the continuity equation (2.32) it follows that $\nabla \cdot \mathbf{u}^{n+1} = 0$ which yields the Poisson equation for the pressure correction p' :

$$\nabla^2 p' = \frac{1}{\Delta\tau} \nabla \cdot \mathbf{u}^* \quad (2.37)$$

After the pressure correction field is obtained, we next proceed to the correction and projection steps, for the pressure and the velocity fields, respectively:

$$p^{n+1} \equiv p' + p^n \quad (2.38)$$

$$\mathbf{u}^{n+1} = \mathbf{u}' - \Delta\tau \cdot \nabla p^* \quad (2.39)$$

2.2.4. Discretization using the finite volume method

To solve the system of N-S equations, the computational domain is discretized by utilizing staggered grid, characterized by a half grid step offset of the pressure and the velocity component fields relatively to each other. The discretized domain allows for determining finite volumes surrounding each discrete pressure and velocity component values as shown in Figure 2.7.

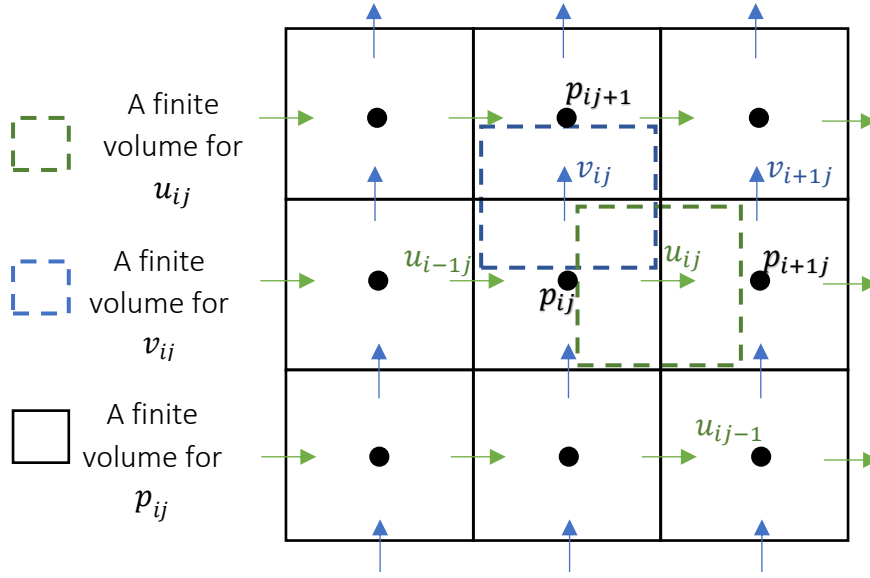


Figure 2.7 - The staggered grid used in the current solver.

The N-S and Poisson equations are next can be integrated over the corresponding finite volumes. The momentum equations (in x and y directions) are integrated over the finite volumes surrounding u and v velocity components, respectively. The Poisson equation is integrated over the finite volume surrounding the pressure. Without losing generality, the equations are analyzed without the source term as appears in equations (2.9) and (2.10). Adding the source term is straight forward and omitted here for sake of conciseness. Discretization of the body force in the momentum equation reflecting the impact of immersed body on the surrounding flow will be explained in section 2.2.5:

$$\int_{V_u} \left[\frac{\partial(\mathbf{u})}{\partial t} + \nabla \cdot (\mathbf{u}\mathbf{u}) \right] dV = \int_{V_u} \left[-\nabla p + \frac{1}{Re} \nabla^2 \mathbf{u} \right] dV \quad (2.40)$$

$$\nabla^2 p' = \frac{1}{\Delta \tau} \nabla \cdot \mathbf{u}^* \quad (2.41)$$

After using divergence theorem, the convection term in Eq. (2.40) can be rewritten in terms of momentum flux passing through the finite volume boundaries, which yields:

$$\int_{V_u} \frac{\partial(\mathbf{u})}{\partial t} dV + \int_{S_u} \mathbf{u}\mathbf{u} \cdot \hat{n} dS = \int_{V_u} \left[-\nabla p + \frac{1}{Re} \nabla^2 \mathbf{u} \right] dV \quad (2.42)$$

All the linear terms (except for the pressure term) are treated implicitly. Detailed formulation of all the discretized terms of the momentum equation is next presented for the equation in x direction:

i. the time derivative term:

$$\int_{V_u} \frac{\partial u}{\partial t} dV = \frac{u_{ij}^* - u_{ij}^n}{\Delta t} \Delta x \Delta y \quad (2.43)$$

ii. The diffusion term:

$$\int_{V_u} \frac{1}{Re} \nabla^2 u dV = \frac{1}{Re} \left(\frac{u_{i+1j}^* - 2u_{ij}^* + u_{i-1j}^*}{\Delta x^2} + \frac{u_{ij+1}^* - 2u_{ij}^* + u_{ij-1}^*}{\Delta y^2} \right) \Delta x \Delta y \quad (2.44)$$

Note that the index "*" denotes the approximation of the velocity at time step $n + 1$ as explained in section (2.2.3).

The rest terms of the momentum equation are determined explicitly:

iii. The pressure term:

$$\int_{c.v} -\nabla p dV = \frac{p_{i+1j}^n - p_{ij}^n}{\Delta x} \Delta x \Delta y \quad (2.45)$$

iv. The convection term:

$$\begin{aligned} \int_{S_u} \mathbf{u} \cdot \hat{n} dS &= \int_{S_u} [u; v] \cdot [n_x; n_y] dS \\ &= u_{i+\frac{1}{2}j} \cdot u_{i+\frac{1}{2}j} \cdot \Delta y + u_{ij+\frac{1}{2}} \cdot v_{i+\frac{1}{2}j} \cdot \Delta x - u_{i-\frac{1}{2}j} \cdot u_{i-\frac{1}{2}j} \cdot \Delta y \\ &\quad - u_{ij-\frac{1}{2}} \cdot v_{i+\frac{1}{2}j-1} \cdot \Delta x, \end{aligned} \quad (2.46)$$

Where:

$$\begin{aligned} u_{i+\frac{1}{2}j} &= \frac{u_{i+1j} + u_{ij}}{2} & u_{ij+\frac{1}{2}} &= \frac{u_{ij+1} + u_{ij}}{2} & v_{i-\frac{1}{2}j+1} &= \frac{v_{ij+1} + v_{i-1j+1}}{2} \\ u_{i-\frac{1}{2}j} &= \frac{u_{i-1j} + u_{ij}}{2} & u_{ij-\frac{1}{2}} &= \frac{u_{ij-1} + u_{ij}}{2} & v_{i-\frac{1}{2}j} &= \frac{v_{ij} + v_{i-1j}}{2} \end{aligned}$$

Note that from here on, the non-linear term is denoted by $N(u_{ij}^n)$ for the sake of conciseness. Plugging in all the discretized terms back into Eq.(2.42) yields the discretized momentum equation:

$$\begin{aligned} & \left(-\frac{1}{\Delta t} \Delta x \Delta y - \frac{2\Delta y}{Re\Delta x} - \frac{2\Delta x}{Re\Delta y} \right) u_{ij}^* + \frac{\Delta x \Delta y}{Re} \frac{u_{i+1j}^* + u_{i-1j}^*}{\Delta x^2} \\ & + \frac{\Delta x \Delta y}{Re} \frac{u_{ij+1}^* + u_{ij-1}^*}{\Delta y^2} = \frac{-u_{ij}^n}{\Delta t} \Delta x \Delta y + N(u_{ij}^n) \end{aligned} \quad (2.47)$$

The left hand side of Eq. (2.47) constitutes the Helmholtz operator $H(u_{ij}^*)$ so that Eq. (2.47) can be formulated as follows:

$$H(u_{ij}^*) = -\Delta x \Delta y \nabla p - \frac{\Delta x \Delta y}{\Delta t} u_{ij}^n + N(u_{ij}^n) \quad (2.48)$$

v. Mass conservation

The Poisson equation, Eq.(2.37) for the pressure correction field is discretized as:

$$\begin{aligned} & \frac{p'_{i+1j} - 2p'_{ij} + p'_{i-1j}}{\Delta x^2} + \frac{p'_{ij+1} - 2p'_{ij} + p'_{ij-1}}{\Delta y^2} \\ & = -\frac{1}{\Delta t} \left(\frac{u_{i+1j}^* - u_{ij}^*}{\Delta x} + \frac{v_{ij+1}^* - v_{ij}^*}{\Delta y} \right) \end{aligned} \quad (2.49)$$

2.2.5. Immersed boundary method (IBM)

The IBM was introduced for the first time by Peskin [46], for implementation of complex and moving boundaries immersed within the fluid. This method discretizes the N-S equations on a fixed Eulerian grid, even though the computational domain can contain moving, complex boundaries immersed into the fluid. The IBM helps to reduce computational costs due to the use of fixed numerical operators. In most cases, the IBM is used in order to enforce the kinematic constraint of no-slip for the fluid velocity at the immersed boundary. In the current study, the cell's membrane plays the role of immersed boundary and used for the calculation of the surface tension forces developing at a membrane of each cell and its interaction with the surrounding fluid and other cells. In this chapter the formulation of the IBM is explained in detail.

Let $\mathbf{X}(s) = (x(s), y(s))$ be the Lagrangian points forming the set of points determining the surface of immersed body. The points are located above underlying Eulerian grid and move with velocity $V(\mathbf{X})$. To achieve the highest accuracy and to reduce stiffness of the discrete operators, the distance between the adjacent Lagrangian points should be

approximately equal to the grid step of the underlying Eulerian grid (see Figure 2.2.). The IBM formalism enforcing the non-slip kinematic constraint on the surface of immersed body incorporated within the SIMPLE algorithm (section 2.2.3) is as follows:

- i. Obtaining the intermediate predicted velocity by utilizing Eq.(2.33) (without considering the presence of immersed body):

$$\frac{\mathbf{u}^{*-\frac{1}{2}} - \mathbf{u}^n}{\Delta\tau} + \nabla \cdot (\mathbf{u}\mathbf{u})^n = -\nabla p^n + \frac{1}{Re} \nabla^2 \mathbf{u}^{*-\frac{1}{2}} \quad (2.50)$$

- ii. Calculating the fluid intermediate velocity at the Lagrangian points using the interpolation operator as described in section 2.2.2:

$$\mathbf{V}'(\mathbf{X}) = \mathcal{J} \left(\mathbf{X}, \mathbf{u}^{*-\frac{1}{2}}(\mathbf{x}) \right) \quad (2.51)$$

- iii. Calculating the Lagrangian forces acting on the fluid at the surface points to account for the presence of immersed body:

$$\mathbf{F}(\mathbf{X}) = \frac{\mathbf{V}(\mathbf{X}) - \mathbf{V}'(\mathbf{X})}{\Delta\tau} \quad (2.52)$$

- i. Smearing the Lagrangian forces to the corresponding locations on the Eulerian grid using the regularization operator as described in section 2.2.2:

$$\mathbf{f}(\mathbf{x}) = \mathcal{R}(\mathbf{X}, \mathbf{F}(\mathbf{X})) \quad (2.53)$$

- ii. Solving the momentum equation with a modified RHS, to find the predicted non-solenoidal velocity:

$$\frac{\mathbf{u}^* - \mathbf{u}^n}{\Delta\tau} + \nabla \cdot (\mathbf{u}\mathbf{u})^n = -\nabla p^n + \frac{1}{Re} \nabla^2 \mathbf{u}^* + \mathbf{f}(\mathbf{x}) \quad (2.54)$$

- iii. Solving the Poisson equation for the pressure correction and updating the pressure and the velocity fields as described in section 2.2.3 (see Eq's. (2.37)-(2.39)).

If the Lagrangian forces are calculated by employing constitutive laws as is performed in the current study, the stages ii-iii are replaced by the procedure described in sections 2.1.1 - 2.1.3.

2.2.6. Gradient decent

The gradient descent method is used to find a local extremum of a given function. In the current study the key idea was to propagate repeatedly in the opposite direction of the function gradient until convergence with a given tolerance is reached to find the local minimum of the function.

Let V be an arbitrary scalar function of set of n parameters:

$$V = f(x_1 \dots x_n) \quad (2.55)$$

The gradient of V is given by:

$$\nabla V = \left(\frac{\partial V}{\partial x_1} \dots \frac{\partial V}{\partial x_n} \right) \quad (2.56)$$

The iteration sequence that should be performed to find the local minimum, closest to the initial state, is defined as:

$$(x_1 \dots x_n)^{k+1} = (x_1 \dots x_n)^k - \alpha \nabla V^n \quad (2.57)$$

Parameter α can be chosen intelligently by using several strategies, a detailed discussion of which remained beyond the scope of the current study.

2.2.7. Two-phase flow model

A wide range of physical phenomena contains interactions between two or more fluid phases. Currently we present a two-phase numerical model that was developed by incorporating immersed boundary and front tacking methods. The model also accounts for the surface tension forces acting at interface between the two phases. Although two-phase modeling was not an inherent part of the current study, it might be used in future studies.

Consider two Newtonian, incompressible fluids A and B within rectangular domain Ω . The interface between the two fluids Γ is determined by the boundary points $\mathbf{X}(c, t)$ forming a closed contour. Far from the interface the two phases have their own densities $\rho_{1,2}$ and viscosities $\mu_{1,2}$ while close to the interface there is a smooth transition between the properties of the two phases.

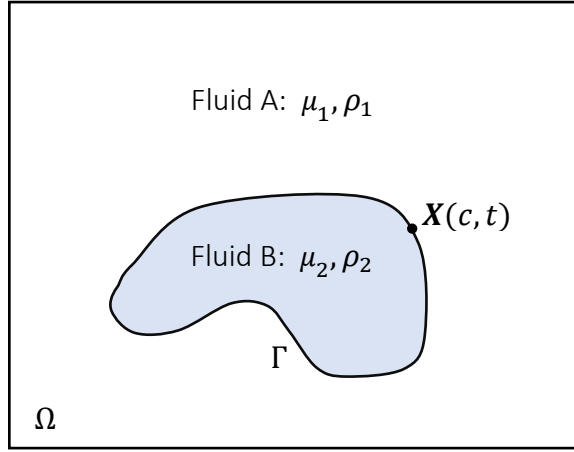


Figure 2.8 - schematic description of two-phase configuration.

The transition is resolved by introducing scalar indicator function $I(\mathbf{x}, t)$ allowing to determine the fluid density and dynamic viscosity as:

$$\rho(\mathbf{x}, t) = \rho_1 + (\rho_2 - \rho_1) \cdot I(\mathbf{x}, t) \quad (2.58)$$

$$\mu(\mathbf{x}, t) = \mu_1 + (\mu_2 - \mu_1) \cdot I(\mathbf{x}, t) \quad (2.59)$$

where $I(\mathbf{x}, t)$ is equal to 0 or 1 for liquids A and B, respectively and lies in the range between 0 and 1 in close to the interface region.

The indicator function is related to the interface geometry as:

$$\nabla I = \int_{\Gamma} \mathbf{n}_k(X_k(c, t)) \delta^2(\mathbf{x} - X_k(c, t)) ds, \quad (2.60)$$

where Γ is the interface curve separating between the two fluids, c is a coordinate along the fluid interface, \mathbf{n}_k is a unit vector normal to interface at point $\mathbf{X}_k(s, t)$ and δ is the Dirac delta function.

We next take the divergence of both sides of Eq. (2.60) yielding the Poisson equation for the indicator function I :

$$\nabla^2 I = \nabla \int_{\Gamma} \mathbf{n}_k(X_k(c, t)) \delta^2(\mathbf{x} - X_k(c, t)) ds \equiv \nabla n \quad (2.61)$$

Eq. (2.61) is discretized on the grid coinciding with that used for the pressure field as can be seen in Figure 2.7. The solution was obtained by the Gauss–Seidel method, while boundary conditions for I field were imposed in grid cells at which the value of ∇n was equal to $\mathbf{0}$ and were set to 0 or 1 for liquids A and B, respectively.

Given the calculated indicator function, the non-dimensional governing equations for the described two-phase model are as follows:

$$\bar{\rho}(I) \left(\frac{\partial \mathbf{u}}{\partial \tau} + \nabla \cdot (\mathbf{u}\mathbf{u}) \right) = -\nabla p + \frac{1}{Re} [\nabla \cdot (\bar{\mu}(I)(\nabla \mathbf{u} + (\nabla \mathbf{u})^T))], \quad (2.62)$$

$$+ \frac{1}{We} \mathbf{f}_\sigma + \frac{\bar{e}_y \bar{\rho}(I)}{Fr^2}$$

$$\nabla \cdot \mathbf{u} = 0, \quad (2.63)$$

where $\bar{\rho}(I)$ and $\bar{\mu}(I)$ are the non-dimensional fluid density and viscosity defined in Eq's. (2.58) and (2.59) and normalized by ρ_{min} and μ_{min} values, $Re = \frac{\rho_{min} UL}{\mu_{min}}$ is the Reynolds number, $We = \frac{\rho_{min} U^2 L}{\sigma}$ and $Fr = \frac{U}{\sqrt{gL}}$ are the Weber and the Froude numbers, σ is the two phases surface tension coefficient, \mathbf{f}_σ is the surface tension force, and \mathbf{g} is the gravitational acceleration.

The surface tension force is computed explicitly and related to the local curvature of the interface as:

$$\mathbf{f}_\sigma = \int_{\Gamma} \sigma \frac{\partial^2 X(c, t)}{\partial c^2} \delta^2(x - X(c, t)) dc. \quad (2.64)$$

Eq's.(2.62) and (2.63) are solved by utilizing the SIMPLE algorithm as detailed in section 2.2.3. Note that, the viscous term of Eq.(2.62) accounts for the spatial variation of the viscosity field, which requires additional processing when performing its discretization. Utilizing the divergence theorem, the viscous term of Eq. (2.62) can be rewritten as:

$$\int_{c.v} \nabla \cdot (\mu(I)(\nabla \mathbf{u} + (\nabla \mathbf{u})^T)) dv = \int_{c.s} [\mu(I)(\nabla \mathbf{u} + (\nabla \mathbf{u})^T)] \cdot \hat{\mathbf{n}} ds, \quad (2.65)$$

Where the gradient of the velocity field $\nabla \mathbf{u}$ is defined as:

$$\nabla \mathbf{u} = \begin{pmatrix} \frac{\partial}{\partial x} \\ \frac{\partial}{\partial y} \end{pmatrix} (u \quad v) = \begin{bmatrix} \frac{\partial u}{\partial x} & \frac{\partial v}{\partial x} \\ \frac{\partial u}{\partial y} & \frac{\partial v}{\partial y} \end{bmatrix}, \quad (2.66)$$

and therefore:

$$(\nabla u + (\nabla u)^T) = \begin{bmatrix} 2 \frac{\partial u}{\partial x} & \frac{\partial v}{\partial x} + \frac{\partial u}{\partial y} \\ \frac{\partial u}{\partial y} + \frac{\partial v}{\partial x} & 2 \frac{\partial v}{\partial y} \end{bmatrix} \quad (2.67)$$

Using Eq. (2.67) in x direction (top row), and integrating over the control volume surrounding u velocity component (the same can be straight forwardly repeated for y direction) leads to:

$$\begin{aligned} \int_{c.s} \mu(I) \left[2 \frac{\partial u}{\partial x} \frac{\partial v}{\partial x} + \frac{\partial u}{\partial y} \right] \cdot \hat{n} ds \\ = \mu(I_{i+1j}) \cdot 2 \frac{\partial u}{\partial x} \Big|_{i+\frac{1}{2}j} \Delta y_{v_{j-1}} + \mu \left(I_{i+\frac{1}{2}j+\frac{1}{2}} \right) \\ \cdot \left(\frac{\partial v}{\partial x} \Big|_{i+\frac{1}{2}j} + \frac{\partial u}{\partial y} \Big|_{ij+\frac{1}{2}} \right) \Delta x_{v_i} - \mu(I_{ij}) \cdot 2 \frac{\partial u}{\partial x} \Big|_{i-\frac{1}{2}j} \Delta y_{v_{j-1}} \\ - \mu \left(I_{i+\frac{1}{2}j-\frac{1}{2}} \right) \cdot \left(\frac{\partial v}{\partial x} \Big|_{i+\frac{1}{2}j-1} + \frac{\partial u}{\partial y} \Big|_{ij-\frac{1}{2}} \right) \Delta x_{v_i}, \end{aligned} \quad (2.68)$$

where:

$$I_{i+\frac{1}{2}j+\frac{1}{2}} = \frac{1}{4} (I_{ij} + I_{ij+1} + I_{i+1j+1} + I_{i+1j}), \quad (2.69)$$

$$I_{i+\frac{1}{2}j-\frac{1}{2}} = \frac{1}{4} (I_{ij} + I_{ij-1} + I_{i+1j-1} + I_{i+1j}), \quad (2.70)$$

and:

$$\frac{\partial u}{\partial x} \Big|_{i+\frac{1}{2}j} = \frac{1}{\Delta x_{u_i}} (u_{i+1j} - u_{ij}) \quad (2.71)$$

$$\frac{\partial v}{\partial x} \Big|_{i+\frac{1}{2}j} = \frac{1}{\Delta x_{v_i}} (v_{i+1j} - v_{ij}) \quad (2.72)$$

$$\frac{\partial u}{\partial y} \Big|_{ij+\frac{1}{2}} = \frac{1}{\Delta y_{u_j}} (u_{ij+1} - u_{ij}) \quad (2.73)$$

$$\frac{\partial u}{\partial x} \Big|_{i-\frac{1}{2}j} = \frac{1}{\Delta x_{u_{i-1}}} (u_{ij} - u_{i-1j}) \quad (2.74)$$

$$\left. \frac{\partial v}{\partial x} \right|_{i+\frac{1}{2}j-1} = \frac{1}{\Delta x_{v_i}} (v_{i+1j-1} - v_{ij-1}) \quad (2.75)$$

$$\left. \frac{\partial u}{\partial y} \right|_{ij-\frac{1}{2}} = \frac{1}{\Delta y_{u_{j-1}}} (u_{ij} - u_{ij-1}) \quad (2.76)$$

Plugging in the above expressions into Eq.(2.68) reads:

$$\begin{aligned} & \int_{c.s} \mu(I) \left[2 \frac{\partial u}{\partial x} \frac{\partial v}{\partial x} + \frac{\partial u}{\partial y} \right] \cdot \hat{n} ds \\ &= \mu(I_{i+1j}) \cdot 2 \frac{\Delta y_{v_{j-1}}}{\Delta x_{u_i}} (u_{i+1j} - u_{ij}) + \mu \left(I_{i+\frac{1}{2}j+\frac{1}{2}} \right) \\ & \cdot \left((v_{i+1j} - v_{ij}) + \frac{\Delta x_{v_i}}{\Delta y_{u_j}} (u_{ij+1} - u_{ij}) \right) - \mu(I_{ij}) \\ & \cdot 2 \frac{\Delta y_{v_{j-1}}}{\Delta x_{u_{i-1}}} (u_{ij} - u_{i-1j}) - \mu \left(I_{i+\frac{1}{2}j-\frac{1}{2}} \right) \\ & \cdot \left((v_{i+1j-1} - v_{ij-1}) + \frac{\Delta x_{v_i}}{\Delta y_{u_{j-1}}} (u_{ij} - u_{ij-1}) \right) \end{aligned} \quad (2.77)$$

$$\begin{aligned} & \left[-2\mu(I_{i+1j}) \cdot \frac{\Delta y_{v_{j-1}}}{\Delta x_{u_i}} - \mu \left(I_{i+\frac{1}{2}j+\frac{1}{2}} \right) \cdot \frac{\Delta x_{v_i}}{\Delta y_{u_j}} - 2 \frac{\Delta y_{v_{j-1}}}{\Delta x_{u_{i-1}}} \mu(I_{ij}) - \mu \left(I_{i+\frac{1}{2}j-\frac{1}{2}} \right) \cdot \frac{\Delta x_{v_i}}{\Delta y_{u_{j-1}}} \right] u_{ij} \\ & + \left[2\mu(I_{i+1j}) \frac{\Delta y_{v_{j-1}}}{\Delta x_{u_i}} \right] u_{i+1j} + \left[2 \frac{\Delta y_{v_{j-1}}}{\Delta x_{u_{i-1}}} \mu(I_{ij}) \right] u_{i-1j} \\ & + \left[\mu \left(I_{i+\frac{1}{2}j+\frac{1}{2}} \right) \frac{\Delta x_{v_i}}{\Delta y_{u_j}} \right] u_{ij+1} + \left[\mu \left(I_{i+\frac{1}{2}j-\frac{1}{2}} \right) \frac{\Delta x_{v_i}}{\Delta y_{u_{j-1}}} \right] u_{ij-1} \\ & + \mu \left(I_{i+\frac{1}{2}j+\frac{1}{2}} \right) (v_{i+1j} - v_{ij}) - \mu \left(I_{i+\frac{1}{2}j-\frac{1}{2}} \right) (v_{i+1j-1} - v_{ij-1}) \end{aligned}$$

Which can be rewritten in a more convenient manner as:

$$A_u u_{ij} + B_u u_{i+1j} + C_u u_{i-1j} + D_u u_{ij+1} + E_u u_{ij-1} + F_v, \quad (2.78)$$

where:

$$A_u = -2\mu(I_{i+1j}) \cdot \frac{\Delta y_{v_{j-1}}}{\Delta x_{u_i}} - \mu \left(I_{i+\frac{1}{2}j+\frac{1}{2}} \right) \cdot \frac{\Delta x_{v_i}}{\Delta y_{u_j}} - 2 \frac{\Delta y_{v_{j-1}}}{\Delta x_{u_{i-1}}} \mu(I_{ij}) - \mu \left(I_{i+\frac{1}{2}j-\frac{1}{2}} \right) \cdot \frac{\Delta x_{v_i}}{\Delta y_{u_{j-1}}}$$

$$B_u = 2\mu(I_{i+1j}) \frac{\Delta y_{v_{j-1}}}{\Delta x_{u_i}}$$

$$C_u = 2 \frac{\Delta y_{v_{j-1}}}{\Delta x_{u_{i-1}}} \mu(I_{ij})$$

$$D_u = \mu \left(I_{i+\frac{1}{2}j+\frac{1}{2}} \right) \frac{\Delta x_{v_i}}{\Delta y_{u_j}}$$

$$E_u = \mu \left(I_{i+\frac{1}{2}j-\frac{1}{2}} \right) \frac{\Delta x_{v_i}}{\Delta y_{u_{j-1}}}$$

$$F_v = \left(I_{i+\frac{1}{2}j+\frac{1}{2}} \right) (v_{i+1j} - v_{ij}) - \mu \left(I_{i+\frac{1}{2}j-\frac{1}{2}} \right) (v_{i+1j-1} - v_{ij-1})$$

Note that A_u, B_u, C_u, D_u, E_u can be determined implicitly, while F_v must be determined explicitly as a consequence of the varying viscosity field. The final discretized form of momentum equation to be solved is as follows:

$$\begin{aligned} \left[\frac{\Delta x \Delta y}{\Delta t} \rho(I) - \frac{1}{Re} A_u \right] u_{ij}^* - \frac{1}{Re} [B_u u_{i+1j}^* + C_u u_{i-1j}^* + D_u u_{ij+1}^* + E_u u_{ij-1}^*] \\ = \Delta x \Delta y (-\nabla p^n + We^{-1} f_\sigma^n) - \rho(I) \cdot N(u_{ij}^n) + \frac{1}{Re} F_v^n. \end{aligned} \quad (2.79)$$

The pressure correction scheme also requires a further modification because of the inhomogeneous distribution of the density field. As a result, Eq. (2.35) is rewritten as:

$$\frac{\mathbf{u}^{n+1} - \mathbf{u}^*}{\Delta t} = -\nabla(p^{n+1} - p^n) \frac{1}{\rho^n} \equiv -\nabla p' \cdot \frac{1}{\rho^n}. \quad (2.80)$$

Taking the divergence of both sides of the equation yields:

$$\frac{1}{\Delta t} \nabla \cdot \mathbf{u}^* = \nabla \cdot \left(\nabla p' \cdot \frac{1}{\rho^n} \right) \quad (2.81)$$

The RHS of Eq. (2.81) is then discretized by assuming linear variation of the density field in the adjacent to the interface region:

$$\begin{aligned}
\nabla \cdot \left(\nabla p' \cdot \frac{1}{\rho^n} \right) = & - \left(\frac{2}{(\rho_{ij}^n + \rho_{i+1j}^n) \Delta x_{v_i} \Delta x_{u_{i-1}}} + \frac{2}{(\rho_{ij}^n + \rho_{i-1j}^n) \Delta x_{v_{i-1}} \Delta x_{u_{i-1}}} \right. \\
& + \left. \frac{2}{(\rho_{ij}^n + \rho_{ij+1}^n) \Delta y_{u_j} \Delta y_{v_{j-1}}} + \frac{2}{(\rho_{ij}^n + \rho_{ij-1}^n) \Delta y_{u_{j-1}} \Delta y_{v_{j-1}}} \right) p_{ij} \\
& + \frac{2}{(\rho_{ij}^n + \rho_{i+1j}^n) \Delta x_{v_i} \Delta x_{u_{i-1}}} p_{i+1j} \\
& + \frac{2}{(\rho_{ij}^n + \rho_{i-1j}^n) \Delta x_{v_{i-1}} \Delta x_{u_{i-1}}} p_{i-1j} \\
& + \frac{2}{(\rho_{ij}^n + \rho_{ij+1}^n) \Delta y_{u_j} \Delta y_{v_{j-1}}} p_{ij+1} \\
& + \frac{2}{(\rho_{ij}^n + \rho_{ij-1}^n) \Delta y_{u_{j-1}} \Delta y_{v_{j-1}}} p_{ij-1}
\end{aligned} \tag{2.82}$$

Using the solution obtained for the Poisson equation (2.81), the projection of predicted non-solenoidal velocity to the divergence free subspace is performed by:

$$\mathbf{u}^{n+1} = \mathbf{u}^* - \nabla p' \cdot \frac{\Delta t}{\rho^n} \tag{2.83}$$

3. Verification Study

In this study, a solver for simulation of incompressible, Newtonian, unsteady flow with an incorporated IBM capability was developed. This chapter presents the verification study of the developed solver by comparing the presently obtained numerical results with the independent data known from literature for three benchmark problems.

To prove the correctness of the implementation of the developed solver we simulate the flow for a number of benchmark configurations. A good agreement between the independent and the presently obtained results provides a solid basis for asserting that the flow currently simulated for novel configurations, by using the presently developed solver, is accurate and physically correct. The test cases presented in this chapter examine the accuracy of the Navier-Stokes equations solver for shear driven flow, the correctness and accuracy of implementation of the IBM, and the implementation of the gradient descent algorithm for finding the local minima of the given function. In addition, non-uniform grid solver which has been also used for the numerical experiments in this study needs a separate verification. The results obtained by the non-uniform grid solver are presented for two out of three benchmarks, while a comparison between the solutions obtained on uniform and non-uniform grids is presented for the first benchmark.

3.1. Lid-Driven cavity flow

The first benchmark, lid-driven cavity flow, is aimed at verifying the capability of the developed solver to simulate shear driven flows. A physical model including geometry and boundary conditions for the lid-driven cavity configuration are presented in Figure 3.1 . The flow was simulated for three different values of Re number.

The physical model is governed by Eq.(2.31) and Eq. (2.32). No-slip boundary condition for all the velocity components was applied at all the cavity boundaries. The top lid was held at constant horizontal velocity u_{lid} . The Re number represents the ratio of the inertia to the viscous force and for the scales typical of the present physical model is defined as:

$$Re = \frac{\rho u_{lid} L}{\mu}, \quad (3.1)$$

where ρ is the fluid density, L is the side length of square cavity, μ is the fluid dynamic viscosity and u_{lid} is the velocity of the cavity top lid.

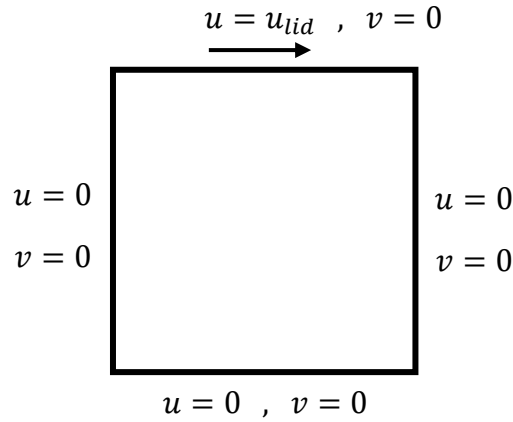


Figure 3.1 - Lid-driven cavity flow, physical model.

The data collected for the quantitative verification includes the values of the horizontal and vertical velocity components taken along vertical and horizontal centerlines. A good agreement between the presently obtained results and the data reported in [48] is observed for the entire range of Re numbers as detailed in Table 3.1 and 3.2. The maximal deviations between the results are observed at locations where the value of the corresponding velocity component is close to zero. Note that the same trend is also observed with respect to the grid independence study. For all other locations, the relative deviations between the independent and the presently obtained results do not exceed 5%. Distributions of velocity components in x and y directions along the vertical centerline calculated on 50×50 and 160×160 uniform grids for $Re = 100$ are presented in Figure 3.2 and in 3.3, respectively.

Table 3.1 - comparison of the values of velocity component in x direction obtained along vertical centerline of the cavity. The results were calculated on 160×160 uniform grid

y	Re = 100			Re = 1000			Re = 5000		
	Ref.	Results	Error %	Ref.	Results	Error %	Ref.	Results	Error %
-	1.0000	1.0000	0	1.0000	1.0000	0.00	1.0000	1.0000	0
1.0000	0.8412	0.8436	-0.29	0.6593	0.6623	0.46	0.4822	0.4855	-0.68
0.9766	0.7887	0.7919	-0.4	0.5749	0.5787	0.65	0.4612	0.4634	-0.48
0.9688	0.7372	0.7404	-0.43	0.5112	0.5138	0.52	0.4599	0.4613	-0.30
0.9609									

y	Re = 100			Re = 1000			Re = 5000		
0.9531	0.6872	0.6908	-0.53	0.4660	0.4677	0.36	0.4604	0.4618	-0.30
0.8516	0.2315	0.2365	-2.15	0.3330	0.3324	-0.19	0.3356	0.3374	-0.54
0.7344	0.0033	0.0041	-23.61	0.1872	0.1859	-0.68	0.2009	0.1979	1.49
0.6172	-0.1364	-0.1387	-1.71	0.0570	0.0561	-1.65	0.0818	0.0783	4.28
0.5000	-0.2058	-0.2090	-1.53	-0.0608	-0.0613	0.87	-0.0303	-0.0316	-4.29
0.4531	-0.2109	-0.2138	-1.37	-0.1065	-0.1068	0.29	-0.0740	-0.0743	-0.41
0.2813	-0.1566	-0.1576	-0.61	-0.2781	-0.2772	-0.30	-0.2285	-0.2291	-0.26
0.1719	-0.1015	-0.1017	-0.22	-0.3829	-0.3839	0.25	-0.3305	-0.3277	0.85
0.1016	-0.0643	-0.0644	-0.13	-0.2973	-0.2967	-0.19	-0.4043	-0.4048	-0.12
0.0703	-0.0478	-0.0466	2.37	-0.2222	-0.2207	-0.67	-0.4364	-0.4282	1.88
0.0625	-0.0419	-0.0420	-0.12	-0.2020	-0.2005	-0.73	-0.4290	-0.4178	2.61
0.0547	-0.0372	-0.0372	-0.15	-0.1811	-0.1798	-0.73	-0.4117	-0.3984	3.23
0	0	0	0	0	0	0	0	0	0

Table 3.2 - comparison of the values of velocity component in y direction obtained along a horizontal centerline of the cavity. The results were calculated on uniform grid

x	Re = 100			Re = 1000			Re = 5000		
-	Ref.	Results	Error %	REF.	Results	Error %	REF.	Results	Error %
1.0000	0	0	0	0	0	0	0	0	0
0.9766	-0.0591	-0.0622	-0.0531	-0.2279	-0.2255	1.05	-0.4977	-0.4970	0.14
0.9688	-0.0739	-0.0780	-0.0551	-0.2937	-0.2908	0.97	-0.5506	-0.5467	0.71
0.9609	-0.0886	-0.0934	-0.0538	-0.3553	-0.3524	0.82	-0.5540	-0.5499	0.74
0.9531	-0.1031	-0.1085	-0.0524	-0.4104	-0.4066	0.93	-0.5287	-0.5249	0.72
0.8516	-0.1691	-0.1770	-0.0468	-0.5264	-0.5207	1.09	-0.4144	-0.4179	-0.84
0.7344	-0.2245	-0.2337	-0.0411	-0.4265	-0.4227	0.88	-0.3621	-0.3652	-0.86
0.6172	-0.2453	-0.2534	-0.0328	-0.3202	-0.3164	1.19	-0.3001	-0.3013	-0.40
0.5000	0.0545	0.0575	-0.0549	0.0258	0.0259	-0.47	0.0095	0.0115	-21.05
0.4531	0.1753	0.1794	-0.0237	0.3254	0.3221	0.99	0.2728	0.2730	-0.07
0.2813	0.1751	0.1792	-0.0236	0.3340	0.3306	1.02	0.2807	0.2810	-0.11
0.1719	0.1608	0.1647	-0.0242	0.3769	0.3719	1.33	0.3537	0.3549	-0.34

x	$Re = 100$			$Re = 1000$			$Re = 5000$		
0.1016	0.1232	0.1263	-0.0253	0.3330	0.3281	1.49	0.4295	0.4268	0.63
0.0703	0.1089	0.1117	-0.0253	0.3099	0.3053	1.48	0.4365	0.4316	1.12
0.0625	0.1009	0.1035	-0.0253	0.2963	0.2917	1.53	0.4333	0.4270	1.45
0.0547	0.0923	0.0947	-0.0255	0.2807	0.2763	1.58	0.4245	0.4171	1.74
0	0	0	0	0	0	0	0	0	0

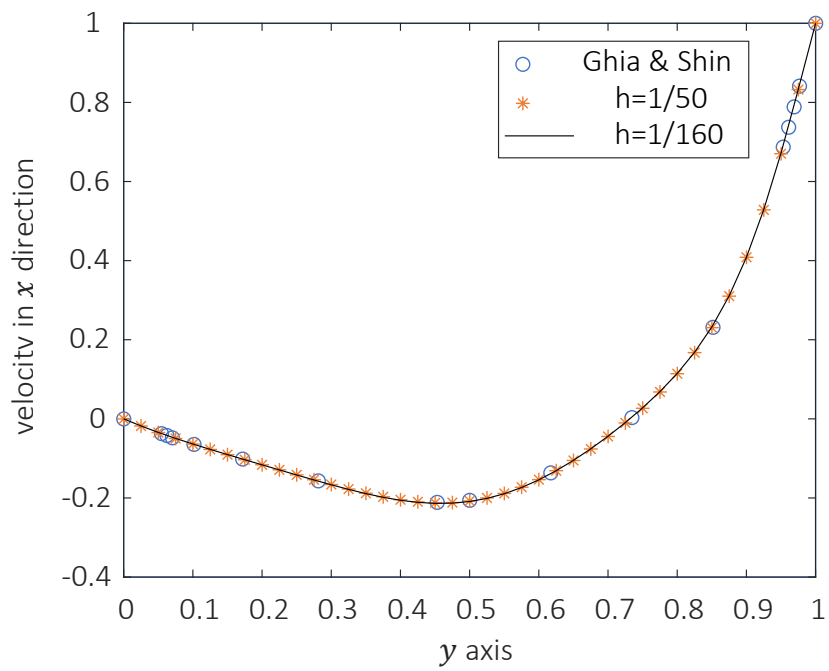


Figure 3.2 – Comparison of the presently obtained steady state values of velocity component in x direction calculated on 50×50 (*) and 160×160 (solid line) grids with the data reported by Ghia & Shin data [48] (o) for $Re = 100$.

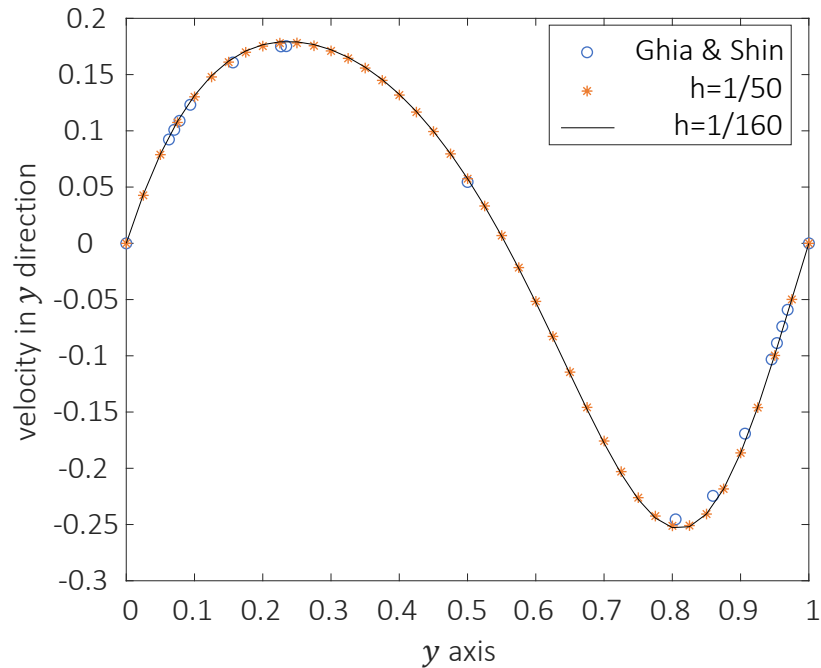


Figure 3.3 - Comparison of the presently obtained steady state values of velocity component in y direction calculated on 50×50 (*) and 160×160 (solid line) grids with the data reported by Ghia & Shin data [48] (o) for $Re = 100$

The maximum relative deviation between the velocity values obtained on both grids does not exceed 5.5% and 8.2% for the velocity values in x and y directions, respectively, which successfully verifies the grid independence of the results.

Additionally, a comparison between the results obtained on uniform grid and these calculated on non-uniform (stretched) grid is shown in Figure 3.4. For the lid-driven cavity configuration, the solver should be capable of resolving the flow characterized by high velocity gradients typical of the vicinity of the cavity walls. Therefore, we investigated the performance of the solver when utilizing non-uniform grids stretched towards the cavity walls. The simulation was performed on non-uniform 70×70 grid whose first step next to the cavity boundary was equal to $h = 1/100$ (instead of $h = 1/70$ characterizing that of the uniform grid).

The capability to perform simulations on non-uniform (stretched) grid is critical for the configurations involving large computational domains compared to the regions characterized by high values of gradients of the flow characteristics. Without the above capability, the simulations can often be computationally prohibited.

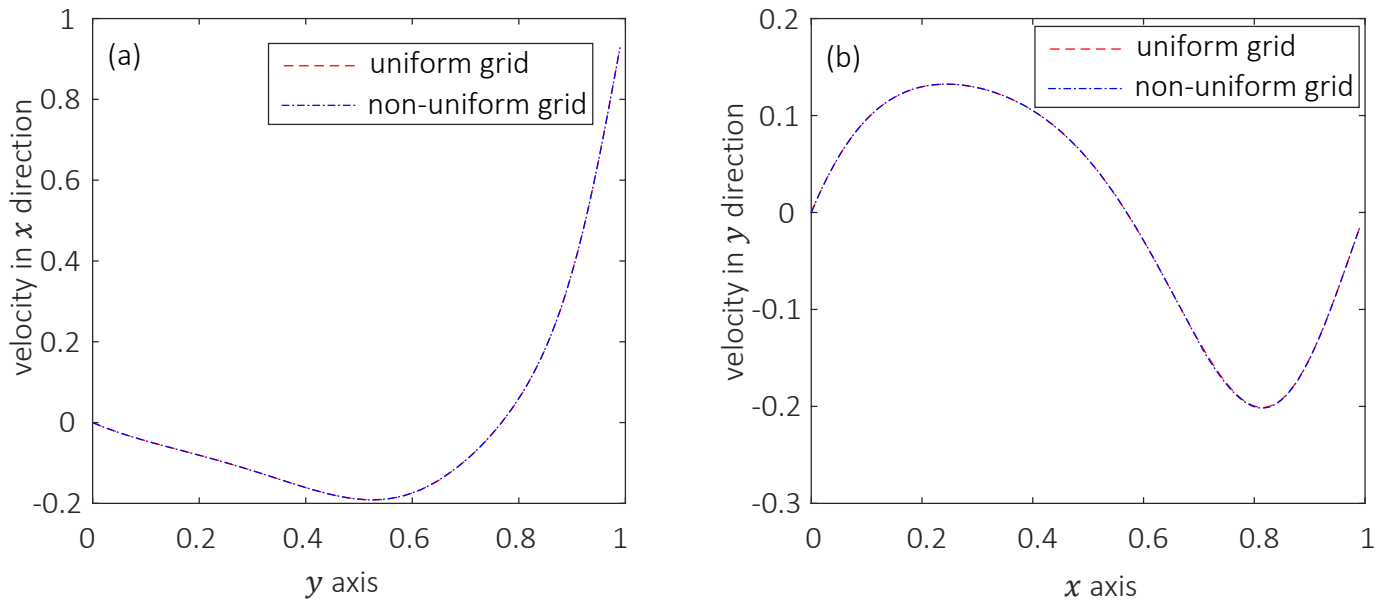


Figure 3.4 - comparison between the results obtained on the uniform grid and on the non-uniform (stretched) grid: (a) velocity in x direction (b) velocity in y direction.

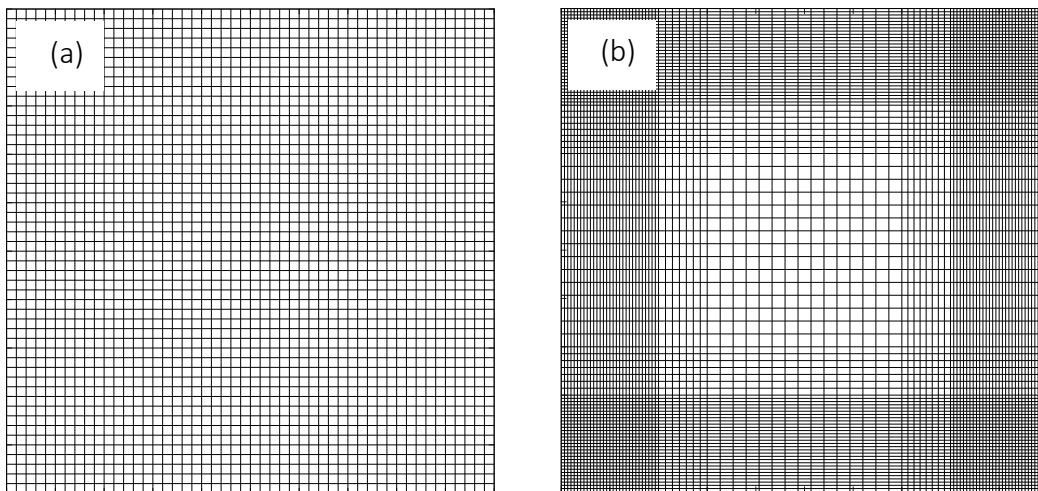


Figure 3.5 – (a) uniform and (b) non-uniform (stretched) grids.

We summarize the verification procedure for the lid driven cavity flow by verifying that the obtained velocity field is divergence free. The time evolution of the maximum value of the velocity divergence calculated at each time step is presented in Figure 3.6.

It can be seen that the maximum value of the divergence velocity was obtained at the beginning of the simulation and was close $5 \cdot 10^{-9}$. The maximum value of the divergence of the velocity decreases as the simulation progresses by about an order of

magnitude, which successfully verifies the correctness of imposing the incompressibility constraint.

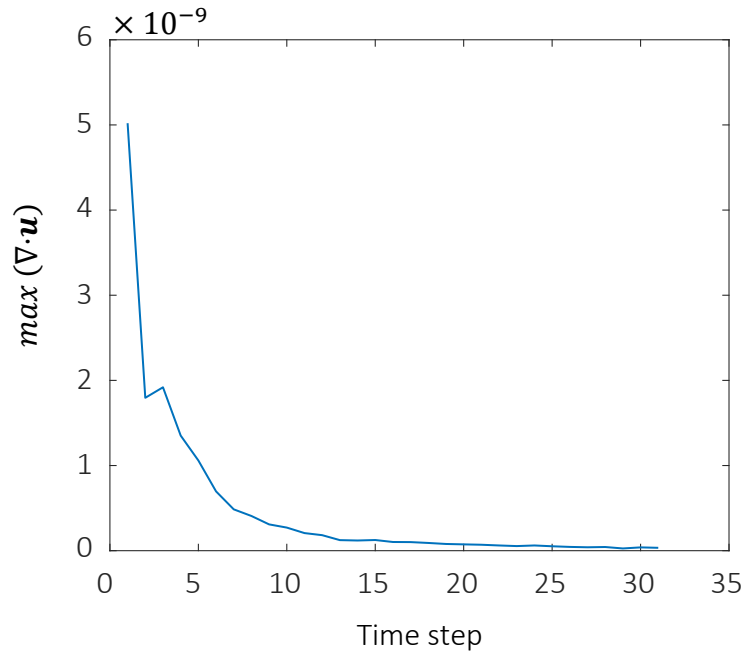


Figure 3.6 – maximum velocity divergence at each time step.

3.2. Moving cylinder

The second benchmark, focusing on the flow around cylinder at spontaneous start, is aimed at verifying the presently implemented IBM capability for the transient flows. The verification was performed by simulating a circular cylinder moving across the cavity after spontaneous start. Physical model including geometry and boundary conditions of the above configuration are shown in Figure 3.7. The flow was simulated for two different values of the Re number.

The physical model is governed by Eq. (2.31) and Eq. (2.32) which includes additional body force stemming from forces exerted from the cylinder to the surrounding fluid as determined by the IBM formalism described in section 2.2.5. No-slip boundary condition for all the velocity components was applied at all the cavity boundaries. All through the simulation the velocity of the cylinder in horizontal direction was set to the value of u_D while the initial values of the velocity within the cavity was set to $u = v = 0$. The Re number is based on the scales typical of the current configuration and is defined as:

$$Re = \frac{\rho u_D L}{\mu} \quad (3.2)$$

The simulations were performed on a non-uniform grid with resolution 420×240 and grid step equal to $h = \frac{1}{50}$ near the cylinder boundary. The time step value was set to $\Delta t = 10^{-4}$.

The time evolution of the drag coefficient C_d was used for verification study. An excellent agreement between the presently obtained results and the data reported in [49], [50] and [51] is observed for both values of Re numbers as shown in Figure 3.8. The fluctuations that persist in the time evolution history are attributed to the numerical noise, similar to that reported in [49]. The noise can be reduced by using smaller time steps, or by using a smoothing technique for discrete Dirac delta functions [52].

The drag coefficient C_d was calculated by taking advantage of the IBM formalism, as given in Eq.(2.52), explicitly yielding the values of singular forces $F(\mathbf{X}(s))$ acting at the points of the immersed surface:

$$C_d = -\frac{\sum F_x(\mathbf{X}(s))}{2} \quad (3.3)$$

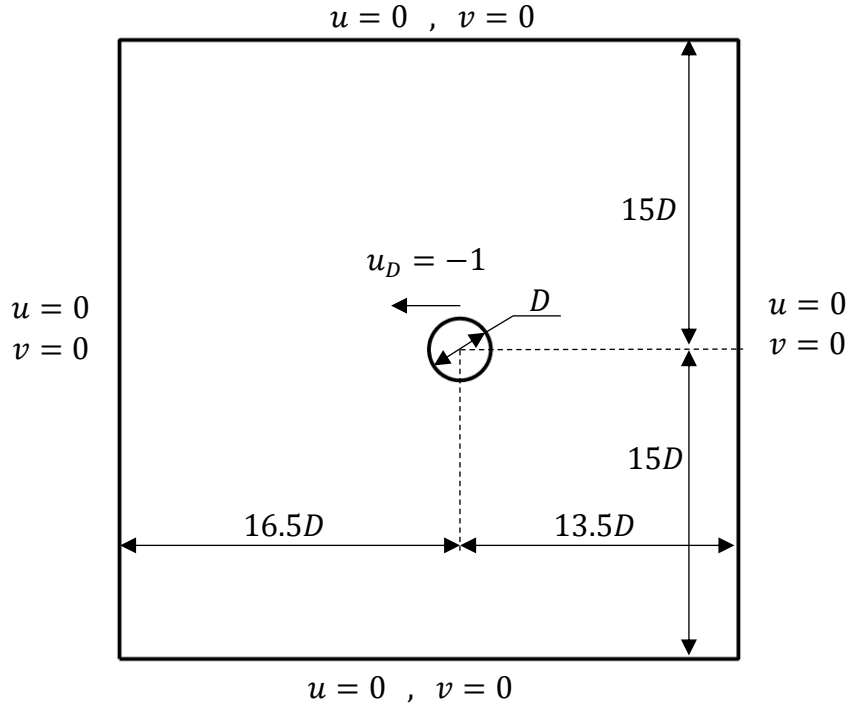


Figure 3.7 - Moving cylinder: physical model.

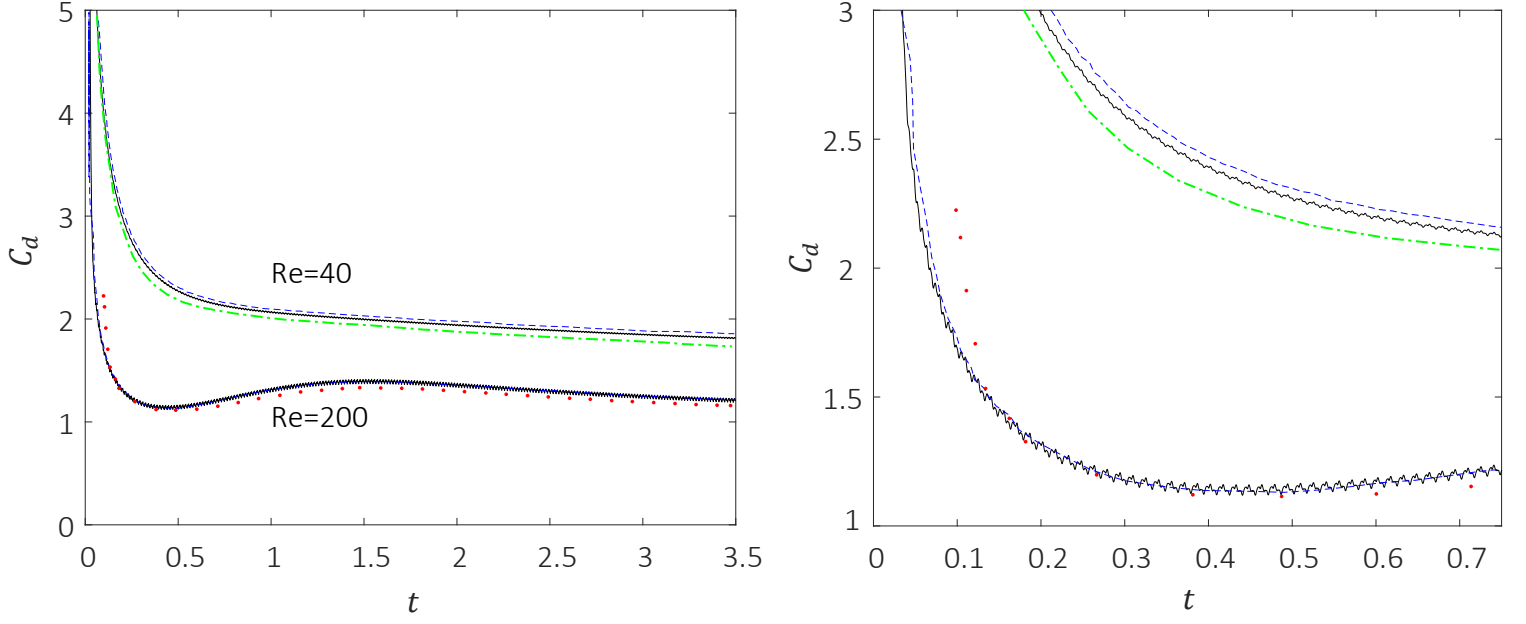


Figure 3.8 - Comparison between the time evolutions of drag coefficient, obtained by the presented solver for $Re = 40, 200$ (—) and the numerical results reported by in [48] ($Re = 40, 200$, - -), [49] ($Re = 40$, · - ·) and [50] ($Re = 200$, ···) [50].

3.3. Gradient descent

In the current study, the gradient descent method is used in order to find the local minimum of several objective functions. In this section the implemented methodology has been validated based on three general test cases.

All test cases consider N circular particles with random radii $0.01 < r_i < 0.1$ (dimensionless) and random initial location $\mathbf{x}_i = (x_i, y_i)$ inside square domain $L \times L$. The energy stored between any pair of particles is given by [53]:

$$e_{ij} = \begin{cases} \epsilon(1 - d_{ij}/\sigma_{ij})^\beta / \beta & d_{ij} < \sigma_{ij} \\ 0 & d_{ij} \geq \sigma_{ij} \end{cases} \quad (3.4)$$

Where ϵ is the characteristic energy scale of the interaction, $d_{ij}(\mathbf{x}_i, \mathbf{x}_j)$ is the separation between the center of the particles i and j , and $\sigma_{ij} = r_i + r_j$. The total energy of a given configuration is:

$$V = \sum e_{ij} \quad (3.5)$$

The presented test cases used $\epsilon = 1$ and $\beta = 2$ (for repulsive harmonic springs). In each test case the gradient descent method has been used, as described in section 2.2.6, in order to get to the local minimum value of V :

$$(\mathbf{x}_1 \dots \mathbf{x}_n)^{k+1} = (\mathbf{x}_1 \dots \mathbf{x}_n)^k - \alpha \nabla V^n \quad (3.6)$$

For the first test, the algorithm has been used without imposing any constraints on the particles' location. The simulation started from a random distribution of overlapping 60 particles, presented in Figure 3.9 (a). At the final stage, the algorithm reached a non-overlapped distribution while the total energy of the system decreased monotonically and until reaching a zero value. As discussed in section 2.2.6, the parameter α can be adjusted in order to accelerate convergence of the algorithm, although no adjustments were made for the present case as the total energy converged rapidly to zero by setting a constant value of $\alpha = 1$.

For the second test, a similar configuration of 60 randomly distributed particles with random radii was chosen. In this case the location of the particles was limited in a way that the particles circumference cannot get out of the square $L \times L$ domain at any time (Figure 3.10). Similarly, to the first test, the energy decreased monotonically and reached zero value, although it took almost twice as many iterations.

The third test case was similar to the second one with only difference that it was performed with additional 10 particles (70 particles in total). In this configuration the energy decrease was characterized by fluctuations and converged to the finite value higher than zero (see Figure 3.11) which indicates the existence of overlapped regions between some of particles.

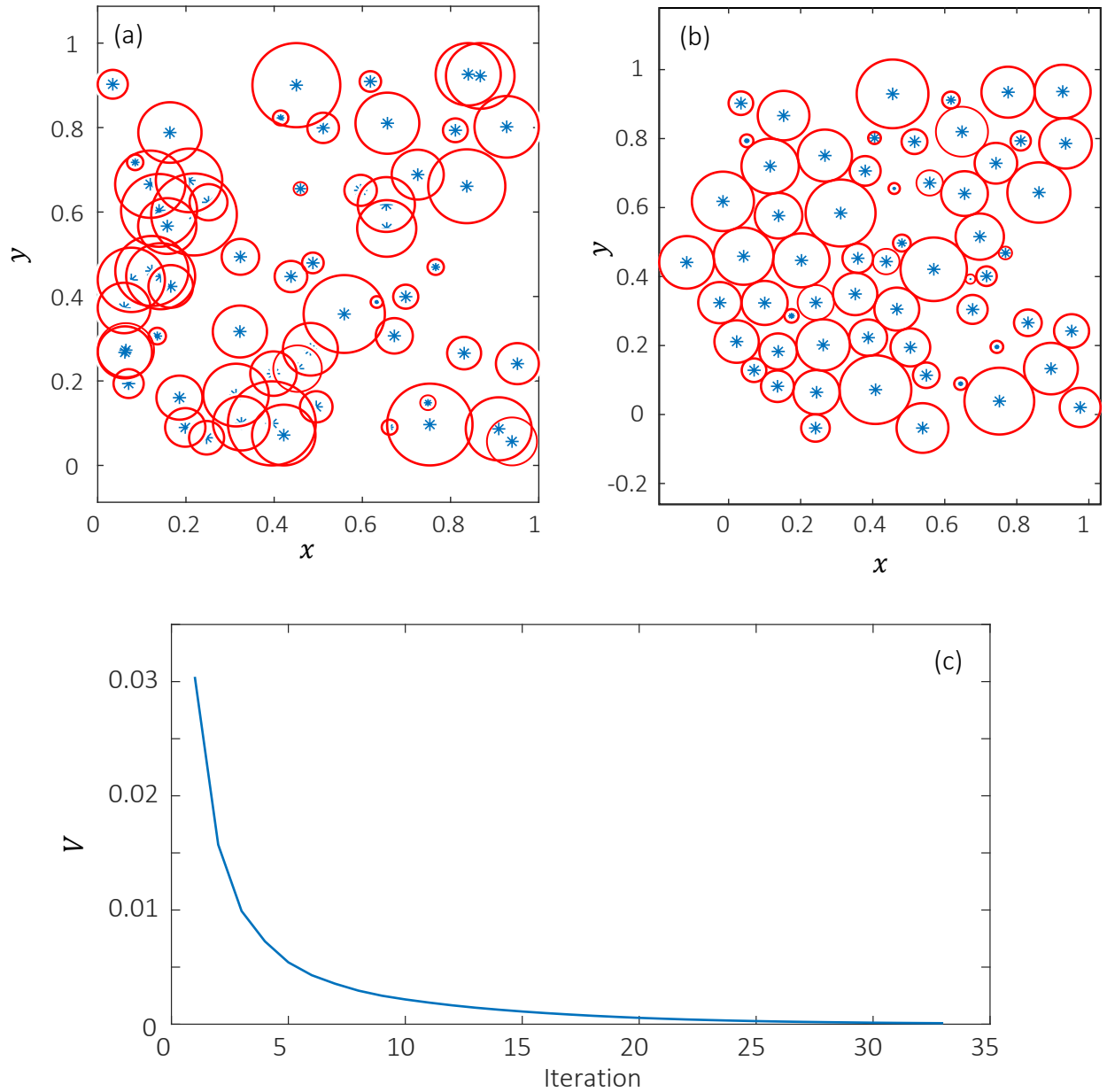


Figure 3.9 – Rearrangement of randomly distributed particles by the gradient decent algorithm for the open boundaries test case: (a) initial random distribution of 60 cylinders with random radii ($0.01 \leq r \leq 0.1$) located within square domain of $L \times L$; (b) rearranged distribution of the cylinders after applying the gradient decent algorithm; (c) iterations evolution of the energy.

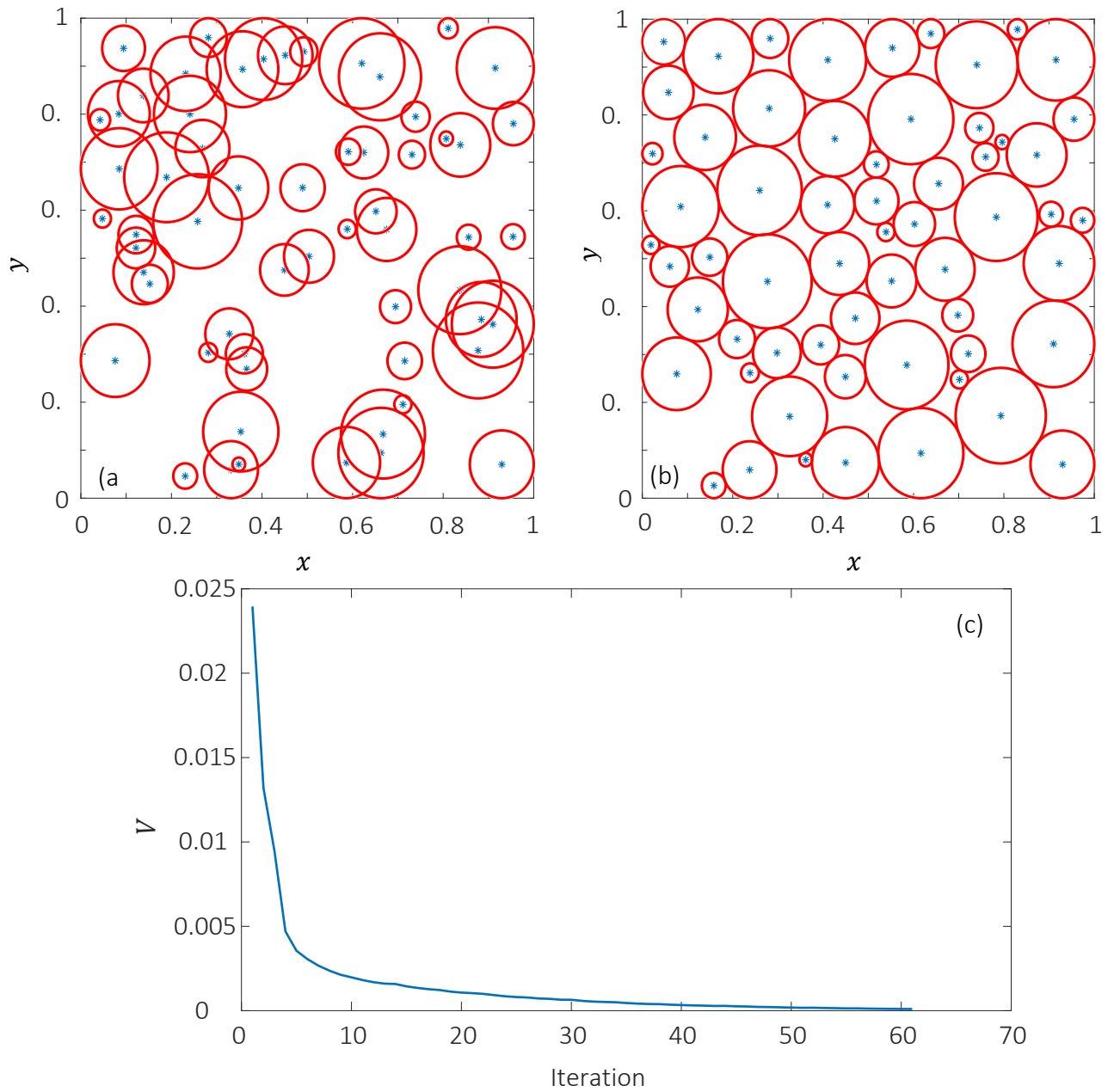


Figure 3.10 - Rearrangement of randomly distributed particles by the gradient decent algorithm for the closed boundaries test case: (a) initial random distribution of 60 cylinders with random radii ($0.01 \leq r \leq 0.1$) located within square domain of $L \times L$; (b) rearranged distribution of the cylinders after applying the gradient decent algorithm together with the closed boundaries constraint; (c) iteration evolution of the energy.

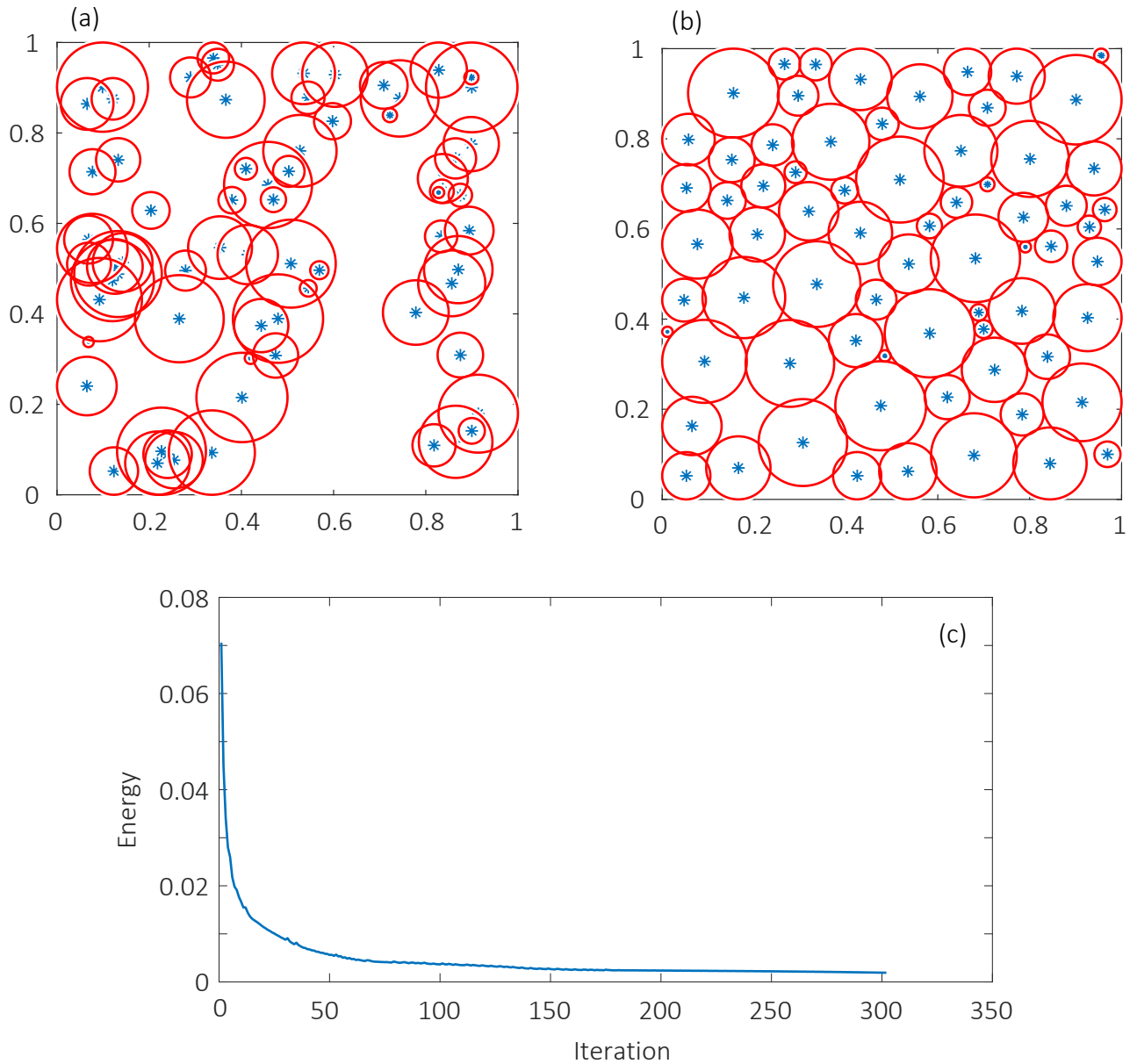


Figure 3.11 - Rearrangement of randomly distributed particles by the gradient decent algorithm for the closed boundaries jammed test case: (a) initial random distribution of 70 cylinders with random radii ($0.01 \leq r \leq 0.1$) located within square domain of $L \times L$; (b) rearranged distribution of the cylinders after applying the gradient decent algorithm together with the closed boundaries constraint; (c) iteration evolution of the energy.

3.4. Two phase flow – drop under shear flow

Although two-phase modeling was not an inherent part of the current study, it might be used in future studies. Hence, we focused on analysis of the configuration of bubble under a shear flow, which is the last test case used for the verification of two-phase model presented in section 2.2.7.

The initial state of the problem is given in Figure 3.12. The circular drop is immersed into fully developed Couette flow and subjected to pure shear stress, while the gravity force is neglected. Under the action of shear stresses, the drop undergoes deformation until the increasing surface tension forces become equal to the shear forces and the drop shape reaches equilibrium. The square box domain is of dimensions $[2D, 2D]$, and the center of the immersed circular drop with diameter D coincides with the geometrical center of the box (point $[D, D]$).

The simulations were performed for four different values of Reynolds number, $Re = 1, 10, 50$, and 100 . The viscosity ratio inputted to the simulation is $\mu_2/\mu_1 = 10$ and the relation between the viscous and surface tension forces is defined by the capillary number Ca :

$$Ca = \frac{Re}{We}, \quad (3.7)$$

which was currently set to be $Ca = 0.2, 0.4$. The boundary conditions applied to the simulations were:

$$\begin{aligned} u(x, y = 2D) &= u(x, y = 0) = U \\ v(x, y = 2D) &= v(x, y = 0) = 0. \end{aligned} \quad (3.8)$$

Periodic boundary conditions were applied for the velocity and pressure fields in the horizontal direction.

A comparison between the final shape of the drop obtained by our simulations to an independent data, reported in [54], is presented in Figure 3.13. The mass loss obtained at the final drop shape is detailed in Table 3.3. It can be seen that the maximum value of the mass loss obtained is **0.0628%**, which indicates an appropriate implementation of the procedure providing the solver incompressibility and the reconstruction technique (see Figure 2.5).

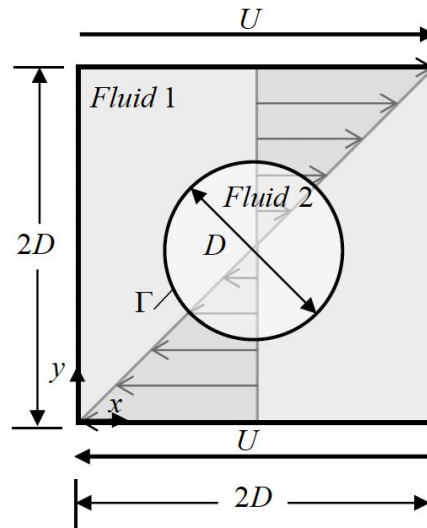


Figure 3.12 - Initial configuration of drop under shear stress [55].

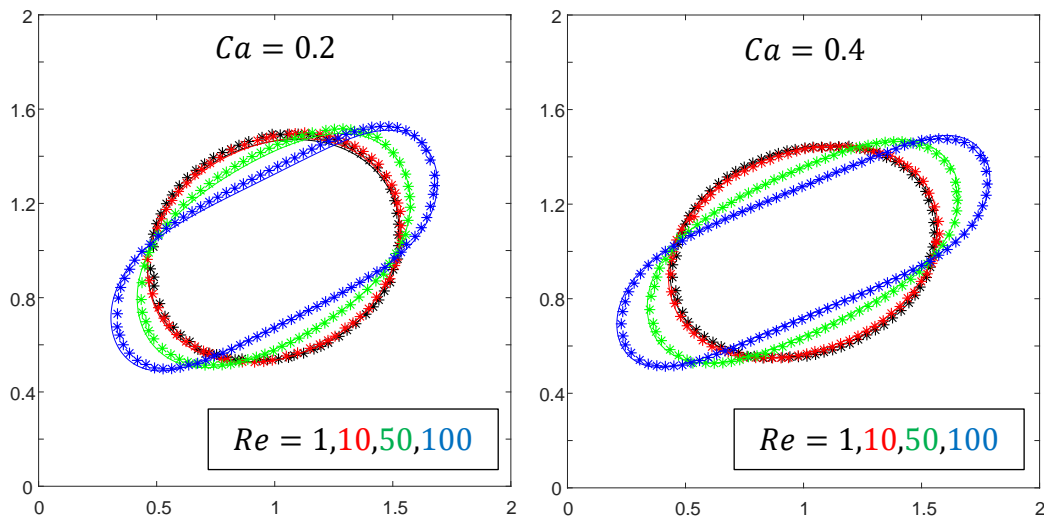


Figure 3.13 - A comparison between the final shape of the drop obtained by our simulations to an independent data. Solid line (-) refers to the presented results, stars (*) refers to data reported in [54].

Table 3.3 - mass loss [%] at the obtained final drop shape.

Re	$Ca = 0.2$	$Ca = 0.4$
1	0.0355	0.029
10	0.0115	0.0084
50	0.0628	0.0168
100	0.013	0.0363

4. Parametric study

In order to ensure that the developed model provides physical results, two parameters must be calibrated: the source strength - $s_{mitosis} \left[\frac{g}{s} \right]$ and the contractile spring stiffness - $k_{cyto} \left[\frac{g}{cm \cdot s^2} \right]$. Although both parameters are artificial and do not have immediate physical analogue to the characteristics of realistic cell, they directly affect the duration of the mitosis process and therefore strongly correlate with proliferation rate. In addition, we will perform the grid independence study for the obtained results.

4.1. Resolution of the grid

This section presents the grid independence study. Resolution of the uniform grid is defined as $r = N/L$, where N is the number of steps in any direction of a quadratic domain with edge length L . The grid independence study was performed by performing the simulations on a number of representative grids, while the time required to complete the mitosis process (growth and division) of the first individual cell was measured on each grid. It turned out that the times measured on the different grids can differ significantly. The reason for the observed deviation between the times is related to the ability of the developed solver to preserve the cell volume (a key factor for any incompressible model) throughout the entire simulation when continuously rearranging the points of the cell boundary. We recall that in accordance with the IBM formalism the rearrangement procedure aimed at preserving an equal distance between the adjacent boundary points is required to provide the highest precision for obtained results. The points rearrangement on the cell boundary (see Figure 2.5) was performed every fixed number of time steps. In our experiments 3 values for the rate of the points rearrangement, namely every 3, 6 and 9 time steps, were chosen.

The volume loss is an inherent part of the boundary rearrangement process and can be minimized either by using a more sophisticated rearrangement scheme or by higher grid resolution. Our numerical experiments revealed that overly frequent boundary reconstruction can increase the volume loss. For this reason, an effort was made to find a balance between the requirement to maintain an equal distance between the IB points and the need to accurately preserve the mass conservation of each individual cell.

The mitosis process (see Figure 2.4) has been simulated for a number of grid resolutions and the time required to complete the entire process was sampled. In addition to the grid resolution, the effect of the frequency of reconstruction of the cell boundary was examined. All the data collected shown in Figure 4.1, clearly demonstrates that the duration of the mitosis process decreases monotonically with increasing grid resolution when the location of the cell boundary points is updated every 3 time steps. For more frequent reconstruction of the points the mitosis duration remains almost unchanged with respect to the grid resolution. Note also that when the grid resolution is characterized by the value of $N \geq 260$ the duration of the mitosis stabilizes for all the cell reconstruction frequencies.

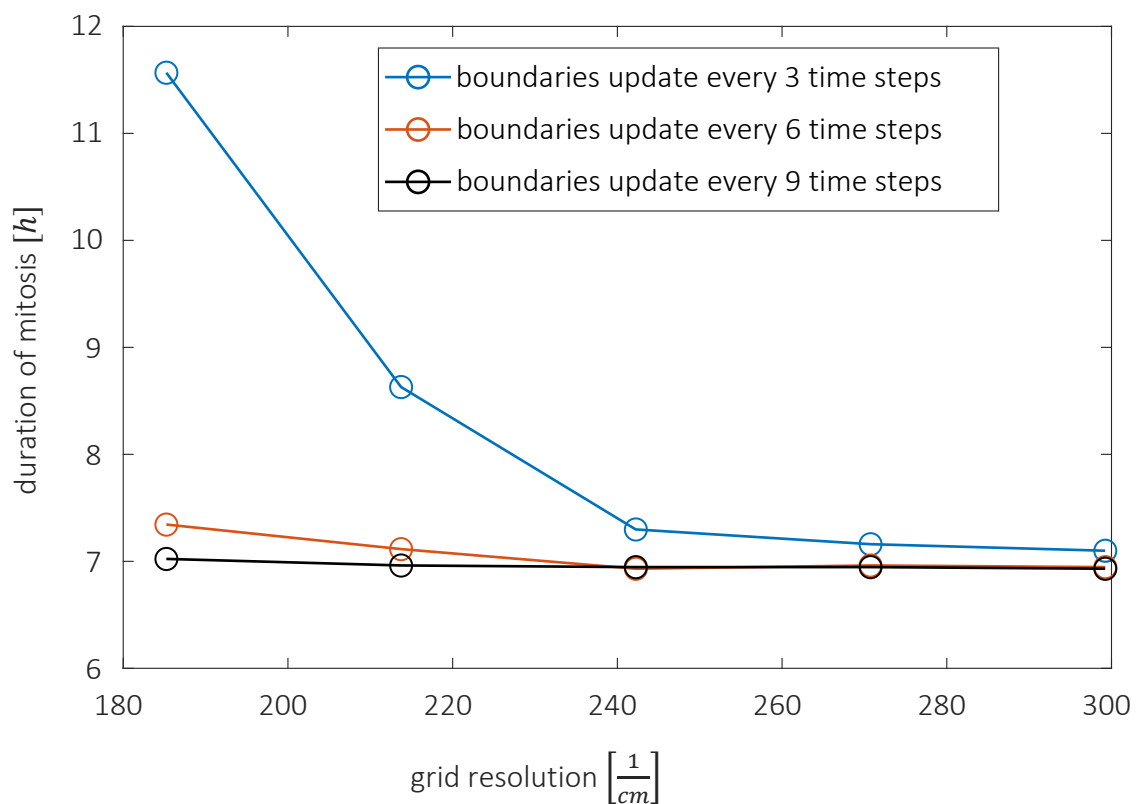


Figure 4.1 – Duration of the mitosis process as a function of grid resolution for different frequencies of reconstruction of the cell boundary points.

To sum up, the conclusion coming up from the performed analysis, is that the reconstruction rate of every 9 time steps and grid with resolution of $N = 300$ can safely be chosen to provide a self-consistent duration of the mitosis process. We next focus on the calibration of the developed model with respect to cytokinesis and the cell growth duration.

4.2. Cytokinesis calibration

Calibration of the developed model starts with the calibration of the cytokinesis process. According to [32], the cytokinesis process is much shorter compared to the complete mitosis process and takes no more than 50 min. The parameter governing the cytokinesis duration is the value of the contractile spring constant k_{cyto} , activated when the mother cell doubles its size, and the cell division process starts.

To precisely calibrate the developed model, a set of simulations correlating between k_{cyto} and duration of cytokinesis process was performed and the results are presented in Figure 4.2. It is important to note that as a result of cells interactions inherent to the growing tissue whose specific randomly chosen cells undergo cytokinesis there are variations in the duration of the cytokinesis process measured for different cells. For this reason, averaging of the measured cytokinesis durations should be done. In the current study the averaging was performed for the cytokinesis durations measured for the first 50 divisions within the specific tissue for each value of k_{cyto} . It can be seen that the value of the contractile spring constant equal to $2300 \left[\frac{g}{cm \cdot s^2} \right]$ yields the value of 30.09 minutes for the duration of cytokinesis process. The value of $k_{cyto} = 2300 \left[\frac{g}{s^2} \right]$ was chosen for all further calculations as it provides the best fit of the developed model to the observed experimental data [32], postulating that the average time typical of cytokinesis is $29.23 [min]$.

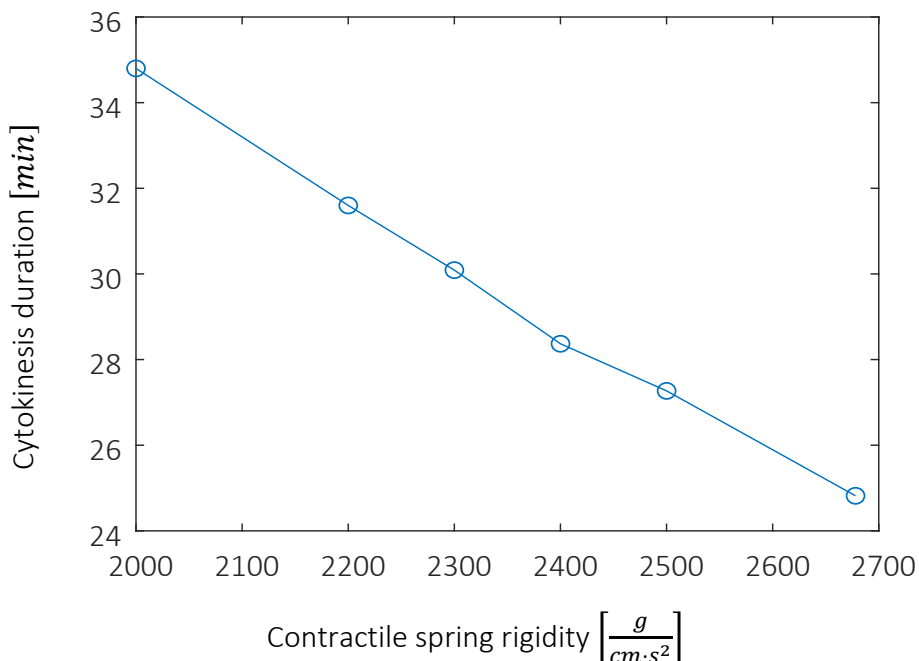


Figure 4.2 – The cytokinesis duration versus the contractile spring rigidity as obtained from the numerical simulations. $k_{cyto} = 2300 \left[\frac{g}{cm \cdot s^2} \right]$ yields the desired value for cytokinesis duration.

4.3. Cell growth calibration

In the next step the entire mitosis process has to be calibrated. According to [32] the average time that takes a cell to double its size is $5.57 [h]$, which determines the value of $s_{mitosis} \left[\frac{g}{s} \right]$. As shown in Figure 4.3, the doubling time value equal to $5.57 [h]$ is obtained by taking a value of the source strength equal to $6.7 \cdot 10^{-8} \left[\frac{g}{s} \right]$.

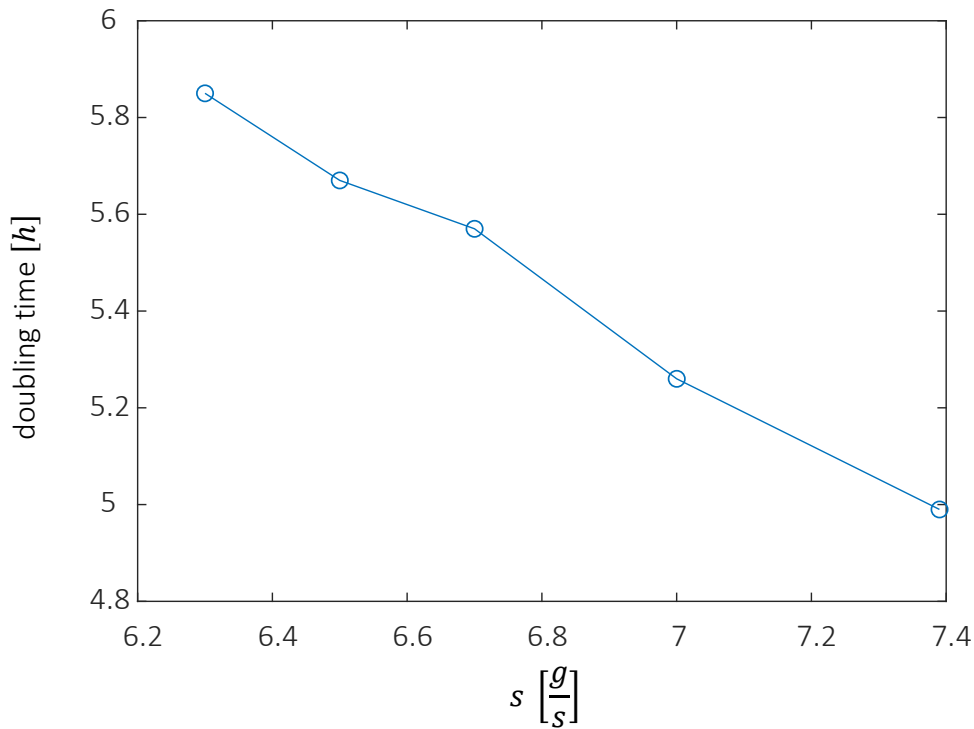


Figure 4.3 – the duration of the cell area doubling versus the source strength.

4.4. Governing parameters

We next establish both dimensional and non-dimensional values of the whole set of parameters, that fully determine the setup of the developed model. Similarly, to the methodology reported in [32], the presented model assumes that the cell cytoplasm is a homogeneous Newtonian fluid with constant properties. For the numerical simulations $\mu = 100 \left[\frac{g}{cm \cdot s} \right]$ and $k_{surface} = 500 \left[\frac{g}{cm \cdot s^2} \right]$ was used. These values were chosen in accordance

with the experimental results reported in [56] postulating that the viscosity and the rigidity values of the cytoskeleton (the complex network material in the cell cytoplasm, which gives the cell its mechanical properties) are in the range of $50 - 140 \left[\frac{g}{cm \cdot s} \right]$ and of $490 - 850 \left[\frac{g}{cm \cdot s^2} \right]$, respectively. According to [57], both phases that compose the cytoplasm (network and solution phase inside the cell membrane) can be treated as incompressible material with quite similar density. For this study, we assume that the fluid density is homogeneous and equal to $\rho = 1.35 \left[\frac{g}{cm^3} \right]$. The adhesion links are modeled by the linear springs with stiffness coefficient of $k_{adh} = 100 \left[\frac{g}{cm \cdot s^2} \right]$, same as used by Rejniak in [32]. In addition, the calibration process yielded the value of the source strength equal to $s_{mitosis} = 6.7 \cdot 10^{-8} \left[\frac{g}{s} \right]$ and the value of contractile spring stiffness equal to $k_{cyto} = 2300 \left[\frac{g}{cm \cdot s^2} \right]$.

In order to normalize the NS equations, we need to define the characteristic values of L, U and T for length, velocity, and time scales, respectively. For the verification purposes the characteristic scales were chosen in accordance with the study of Rejniak [32]. The characteristic length is equal to a diameter of a fully developed tumor $L = 0.0285 [cm]$ (according to figure in [32]). The time needed for one individual cell to progress to the tumor mentioned is $T = 153 [h] = 550800 [s]$ as also mentioned in [1]. Basing on all the above data, the characteristic velocity can be obtained by:

$$U = \frac{L}{T} = 5.174 \cdot 10^{-8} \left[\frac{cm}{s} \right]$$

providing the value of Reynolds number:

$$Re = \frac{\rho UL}{\mu} = 1.991 \cdot 10^{-11}$$

Table 4.1 - Summary of parameters value and its normalizing factor

<i>Parameter</i>	<i>Symbol</i>	<i>Dimensional value</i>	<i>Normalizing factor</i>
Viscosity	μ	$100 \left[\frac{g}{cm \cdot s} \right]$	-
Density	ρ	$1.35 \left[\frac{g}{cm^3} \right]$	-

Characteristic length	L	0.0285 [cm]	
Characteristic velocity	U	$5.174 \cdot 10^{-8} \left[\frac{cm}{s} \right]$	-
Source strength	$S_{mitosis}$	$6.7 \cdot 10^{-8} \left[\frac{g}{s} \right]$	$\frac{\rho U}{L}$
Contractile spring stiffness	k_{cyto}	$2300 \left[\frac{g}{cm \cdot s^2} \right]$	ρU^2
Adhesion spring stiffness	k_{adh}	$100 \left[\frac{g}{cm \cdot s^2} \right]$	ρU^2
Surface tension spring stiffness	k_{ST}	$500 \left[\frac{g}{cm \cdot s^2} \right]$	ρU^2

5. Validation study, results, and discussion

In this chapter we present a detailed validation study, quantitatively comparing 4 basic metrics typical of the tumor progression as proposed by Rejniak [32]. The purpose of this chapter is to validate that the currently implemented basic model produces realistic digital images of cell colonies.

All the simulations were performed in a quadratic domain of $[50d \times 50d]$, where d is the initial cell diameter. An open boundary condition was applied on each boundary of the domain. The simulations started with one individual cell and eventually reached a well-developed tumor containing about 700 cells (Figure 5.1).

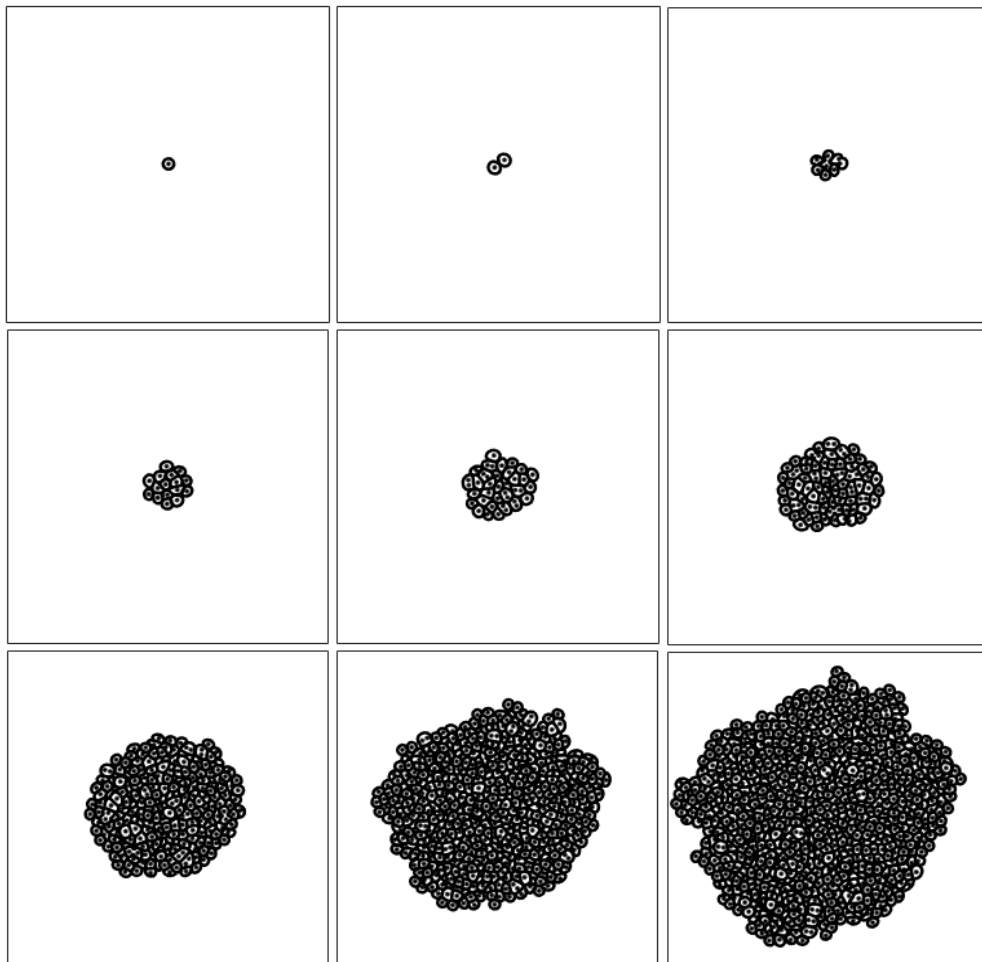


Figure 5.1 – Tumor development, from its very early stage to a well-developed tumor containing 680 cells.

5.1. Area conservation after the cell division

Following the study of Rejniak [32], the area of the daughter cells immediately after the mother cell division has been tracked. Quantitative comparison between the obtained results and the data reported in [32] is shown in Figure 5.2. As no preference is given to any of the daughter cells created in course of division of the corresponding mother cell, it would be reasonable to expect the same values (equal to $78.53 [\mu\text{m}^2]$) of both daughter cells areas right after the division process is completed. However, uneven discretization of the cell membrane and certain area loss are caused by the discretization errors. The discrepancy is quantified by measuring the area of each specific daughter cell and by calculating the average area of all the daughter cells as shown in Figure 5.2 (a).

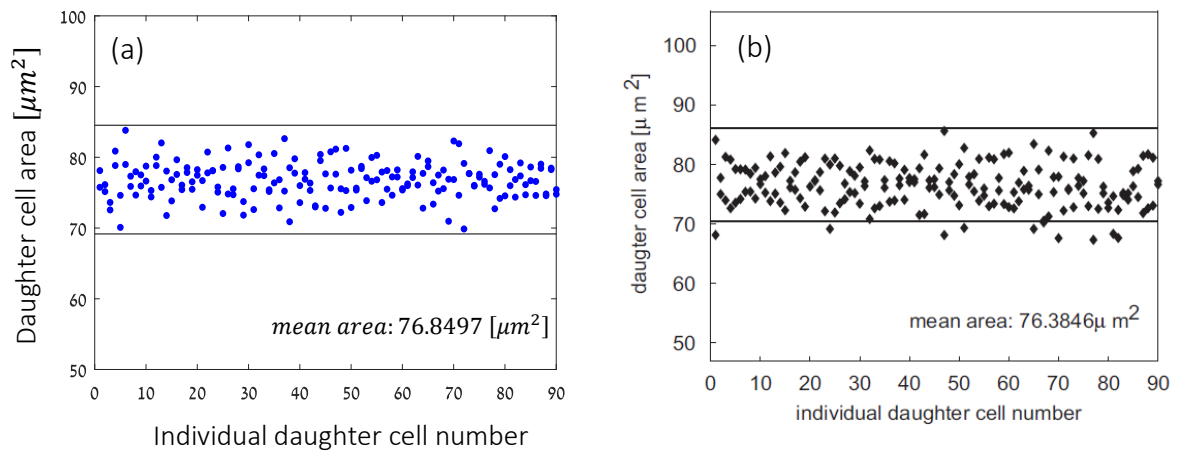


Figure 5.2 - Values of the daughter cell area measured immediately after division of the mother cell: (a) presently obtained results; (b) independent results [32].

It can be seen that all the obtained values of daughter cell areas are within the range of $\pm 10\%$ with respect to the calculated average value which is a bit lower than an expected value equal to $78.53 [\mu\text{m}^2]$. Nevertheless, the obtained results are consistent with the observations made in [1] (see Figure 5.2(b)) reporting the same order of scattering in area of daughter cells. Note also that the results obtained by the presently developed model provide a bit higher value of the average cell area, indicating a lower area loss.

5.2. The cell area doubling time

The next metrics chosen for validation of the developed model is the cell area doubling time, i.e., the time interval measured from the moment the cell mitosis has been initiated

until the moment the cell area has been doubled reaching the value of $2 \cdot 78.53 = 157.06 \mu\text{m}^2$.

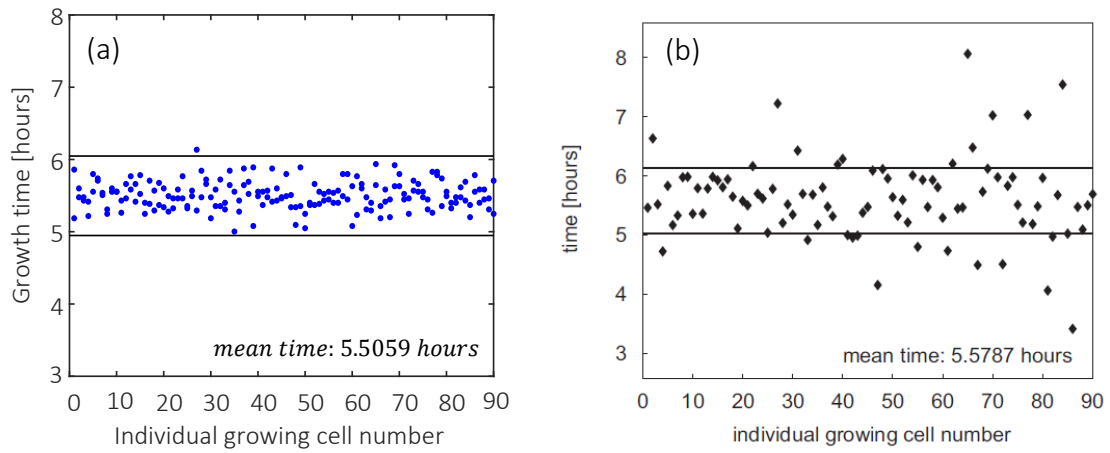


Figure 5.3 – Time required for doubling of individual cells: (a) presently obtained result; (b) independent results [32].

Comparison of the doubling time metrics between the present and the independent results reported in [32] can be seen in Figure 5.3. It can be seen that the presently obtained results are characterized by a lower variance compared to that reported in [32], which can be attributed to specifically developed procedure accurately preserving the symmetry when modeling the cytokinesis process.

5.3. The duration of the cytokinesis process

The third metrics chosen for validation of the developed model is the duration of the cytokinesis process, i.e., the time interval measured from the moment that a cell doubled its area to the moment of creating two daughter cells. Our simulation yielded quite similar results to these reported in Rejniak’s study [32], as can be seen in Figure 5.4.

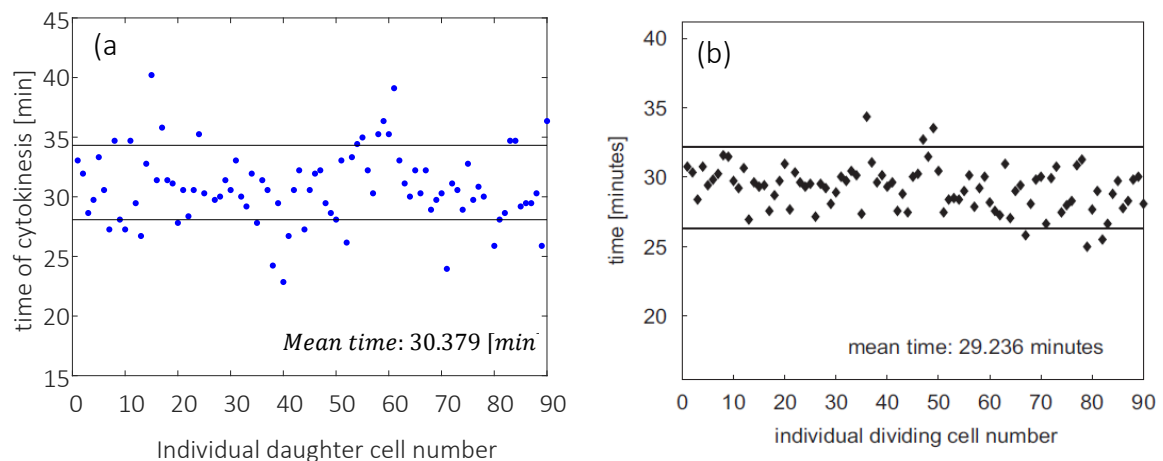


Figure 5.4 - Time required for completing the cytokinesis process: (a) presently obtained result; (b) independent results [32].

It can be clearly seen that the results provided by the developed model are characterized by a higher scatter compared to the previously discussed metrics. The reason for such a behavior is that the cytokinesis is affected by the transient forces exerted both from the division spring and from the cell environment (such as adhesive connections or another mitotic cells). This is in contrast with the cell doubling time, which is primarily governed by the source strength and the incompressibility constraint of the fluid.

5.4. Time evolution of the proliferation and the tumor area

Time evolution of the proliferation and the tumor area shown in Figure 5.5 was chosen as the last metrics for validation of the presently developed model. This validation metrics is of significant importance as it reflects the global impact of the whole tumor on cytokinesis duration of every specific cell. As has been already stated, the cytokinesis duration is affected by external forces exerted from the far cell environment, thus properly validated time evolution of the proliferation and the tumor area will provide correct picture of the tumor development in a long term.

The quantitative similarity between the obtained and the previously reported results [1] is quite evident. Remarkable that an initially observed exponential trend of growth of the cell population is further relaxed to a linear growth, which is a qualitatively typical clinical behavior of realistic tumors [58].

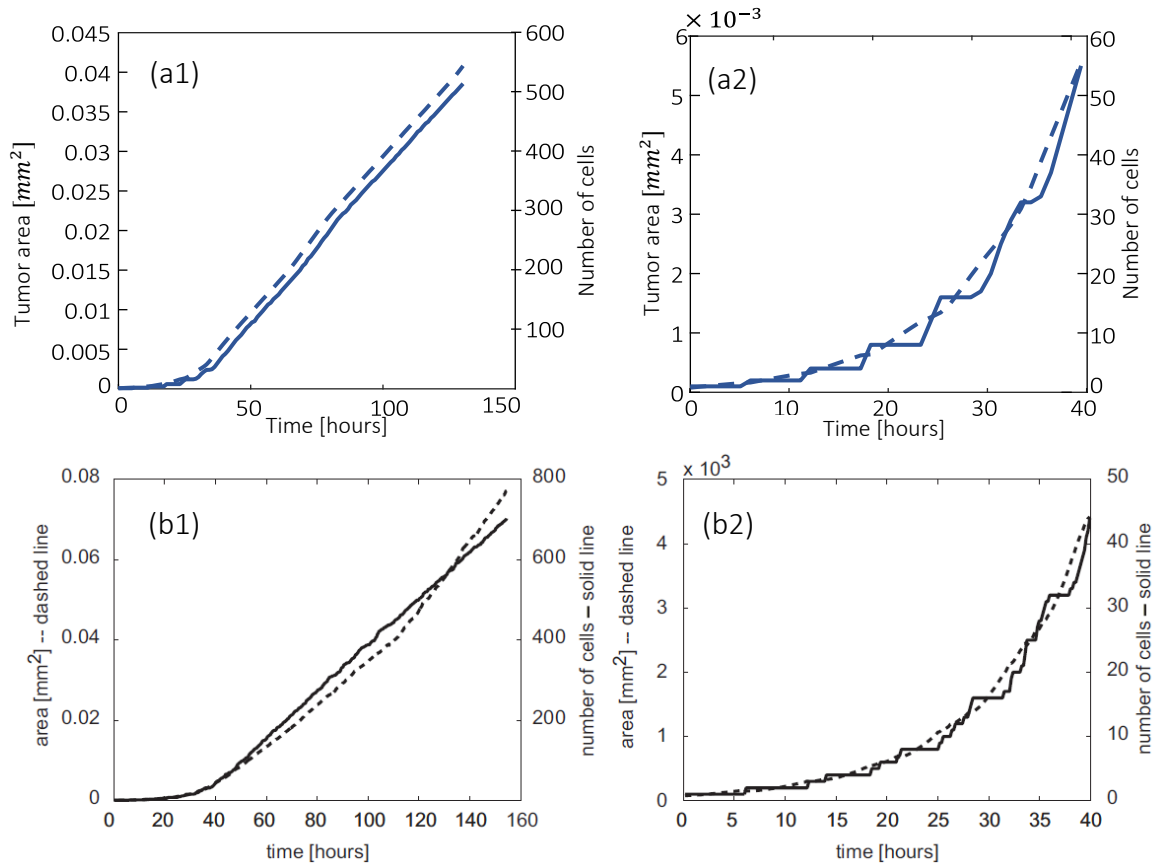


Figure 5.5 - Time evolution of the proliferation and the tumor area: presently obtained results (a1-a2); independent results (b1-b2) [1]. Initially exponential growth of the tumor has changed to linear growth at $t=40h$.

6. Numerical design and analysis of the biological tissue

In this chapter, an extension of the basic model validated in the previous chapter is presented. Numerical algorithms, based on minimization of mechanical energy, determining the tissue development and progress were developed. Most of the developed algorithms utilize the gradient descent method (see section 2.2.6) applied either to the prebuilt tumor tissue or to the growth rate of individual cells during the tumor development. Two types of objective functions i.e., minimizing of either potential or kinetic energies were examined in the framework of the current research.

6.1. Tumor energy relaxation

In this section, the potential energy stored in the linear springs connecting between adjacent cells of the tissue and modelling adhesion forces within it, will be monitored. The springs along with the fluid located between the cells model the ECM of the tissue (see Figure 2.1).

In order to build the tissue whose equilibrium state satisfies the local minimum of internal energy, an algorithm based on gradient descent method has been developed. At this stage the focus was on finding a local minimum of the potential energy stored in the adhesion springs, since it was assumed that it makes the main contribution to the overall energy stored within the tumor tissue. The energy stored in adhesion spring connecting between points \mathbf{X}_i and \mathbf{X}_j is defined as follows:

$$e_p(\mathbf{X}_i, \mathbf{X}_j) = \begin{cases} \frac{1}{2} (\|\mathbf{X}_i - \mathbf{X}_j\| - \ell_{adh})^2 & \|\mathbf{X}_i - \mathbf{X}_j\| \leq r_{adh} \\ 0 & \|\mathbf{X}_i - \mathbf{X}_j\| \geq r_{adh} \end{cases} \quad (6.1)$$

where e_p is the potential energy of the single adhesion spring, \mathbf{X}_i and \mathbf{X}_j are the coordinates of two boundary points belonging to two neighbor cells connected by the adhesion spring characterized by the free length ℓ_{adh} , and r_{adh} is the connection range (as defined in section 2.1). Therefore, the global internal energy stored within the tissue is given by:

$$E_p = \sum_{i,j} e_p. \quad (6.2)$$

We next introduce the coordinates of geometry center of an individual cell given by $\mathbf{x}_c = (x_c, y_c)$. The relative location of a pair of geometric centers of the neighbor cells determines the existence of an adhesive connection between them and the amount of energy stored in the connection if exists. Note that the coordinates \mathbf{X}_i and \mathbf{X}_j belonging to the boundaries of a pair of adjacent cells entering Eq. (6.1) are function of \mathbf{x}_c of each cell. Therefore, the gradient of the potential energy is given by:

$$\nabla E_p = \left(\frac{\partial E_p}{\partial x_{c_1}}, \frac{\partial E_p}{\partial y_{c_1}}, \dots, \frac{\partial E_p}{\partial x_{c_n}}, \frac{\partial E_p}{\partial y_{c_n}} \right) \quad (6.3)$$

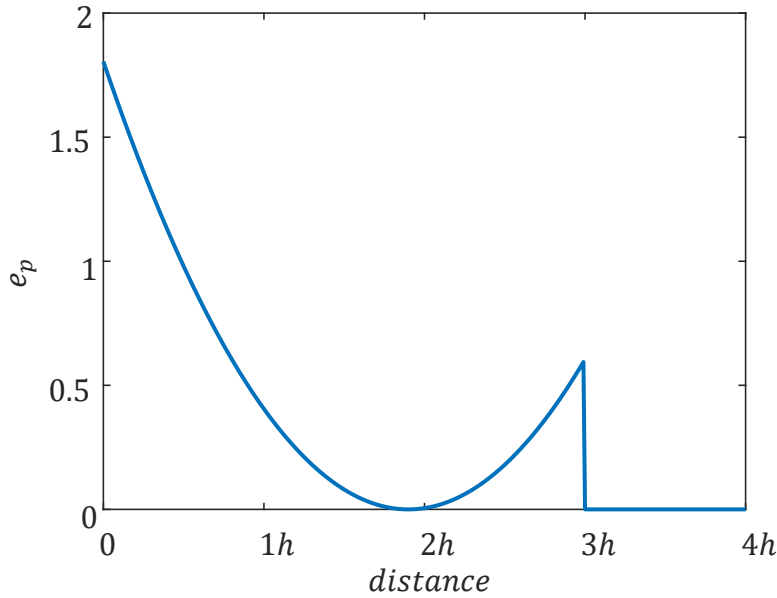


Figure 6.1 - Potential energy e_p stored in a adhesive spring as a function of $\|\mathbf{X}_i - \mathbf{X}_j\|$. At distance of $3h$ the adhesion links disconnect and the energy becomes zero.

For a given configuration of the tissue, the developed algorithm computes the gradient of the energy given by Eq. (6.3), and modifies the location of each cell in the opposite to the energy gradient direction:

$$\begin{bmatrix} x_{c_1} \\ y_{c_1} \\ \vdots \\ x_{c_n} \\ y_{c_n} \end{bmatrix}^{k+1} = \begin{bmatrix} x_{c_1} \\ y_{c_1} \\ \vdots \\ x_{c_n} \\ y_{c_n} \end{bmatrix}^k - \alpha \frac{\nabla E_p}{|\nabla E_p|}, \quad (6.4)$$

where k corresponds to the iteration number and α is a factor. In addition, no-overlapping constraint was enforced for all the cells entering the tissue.

The iterations were performed until the convergence of the overall energy to the local minimum with a given precision was reached. To estimate the optimal value of the coefficient α at each iteration four successive values of α were tested and the value providing the highest rate of convergence was chosen. The energy state obtained in the current iteration was used as an input to the next iteration. Note that the energy value determined by Eq.(6.1) is normalized by the value of the spring constant k_{adh} , as it allows to work with smaller numbers and does not affect the result provided by the gradient descent method.

To answer the question whether the developed methodology yields tissue whose structure is close to that characterizing the tissues with minimal internal energy we next define the relative change between the potential energy of the original configuration and its counterpart obtained after applying the gradient descent method:

$$\Delta_{E_p} = \frac{E_{p_{initial}} - E_{p_{final}}}{E_{p_{initial}}}, \quad (6.5)$$

and the tissue boundaries expansion in x and y directions:

$$\Delta_x = \frac{L_{final} - L_{initial}}{L_{initial}}, \quad (6.6)$$

$$\Delta_y = \frac{H_{final} - H_{initial}}{H_{initial}},$$

where:

$$L = \max(x_{cells\ membran}) - \min(x_{cells\ membran}) \quad (6.7)$$

$$H = \max(y_{cells\ membran}) - \min(y_{cells\ membran})$$

The images of original and optimized tissue built of 24 cells can be seen in Figure 6.2 (a) and 6.2 (b), respectively. The iteration evolution of internal energy after employing the gradient descent optimization to the original tissue is shown in Figure 6.2 (c). It can be seen that the process of converging energy to its local minimum (Figure 6.2 [c]) is characterized by the high-frequency fluctuations, which are the result of the non-overlapping constraint

and of the discontinuity characterizing the potential spring energy of a single spring (see Figure 6.1).

Note the striking similarity existing between the original and the optimized tissues, although the internal energy of the optimized tissue decreased by 76%. This observation indicates that the structure of the tissue built by the developed methodology is physically justified as it is very close to that characterized by the minimized internal energy.

Figure 6.3 shows that the impact of the optimization applied to the originally built tissue decreases with the tissue's growth and proportional to $\sim e^{-0.01N}$ where N is the current cells number. In fact, the relative decrease in the internal energy stored within the tissue dropped from 87% for the tissue built of 8 cells to 8% for the tissue built of 248 cells. Similar trend can be seen with respect to the rate of the spatial expansion of tumor proportional to $\sim e^{-0.027N}$ and $\sim e^{-0.039N}$ in x and y direction, respectively, although the quantitative decrease in the rate of spatial expansion amounted to a few percent.

Important, as the tissue grows the global internal energy of the obtained tissue stabilizes and gets closer to its local minimum characterizing the equilibrium state. The above observation can be explained by the decreasing ratio of the number of growing cells to the total number of cells as the tissue grows. As a result, relatively small regions of the entire tissue are affected by the forces driving its motion. Additionally, loaded springs by their very nature tend to reach their equilibrium by pushing or pulling nearby cells allthrough the tissue development.

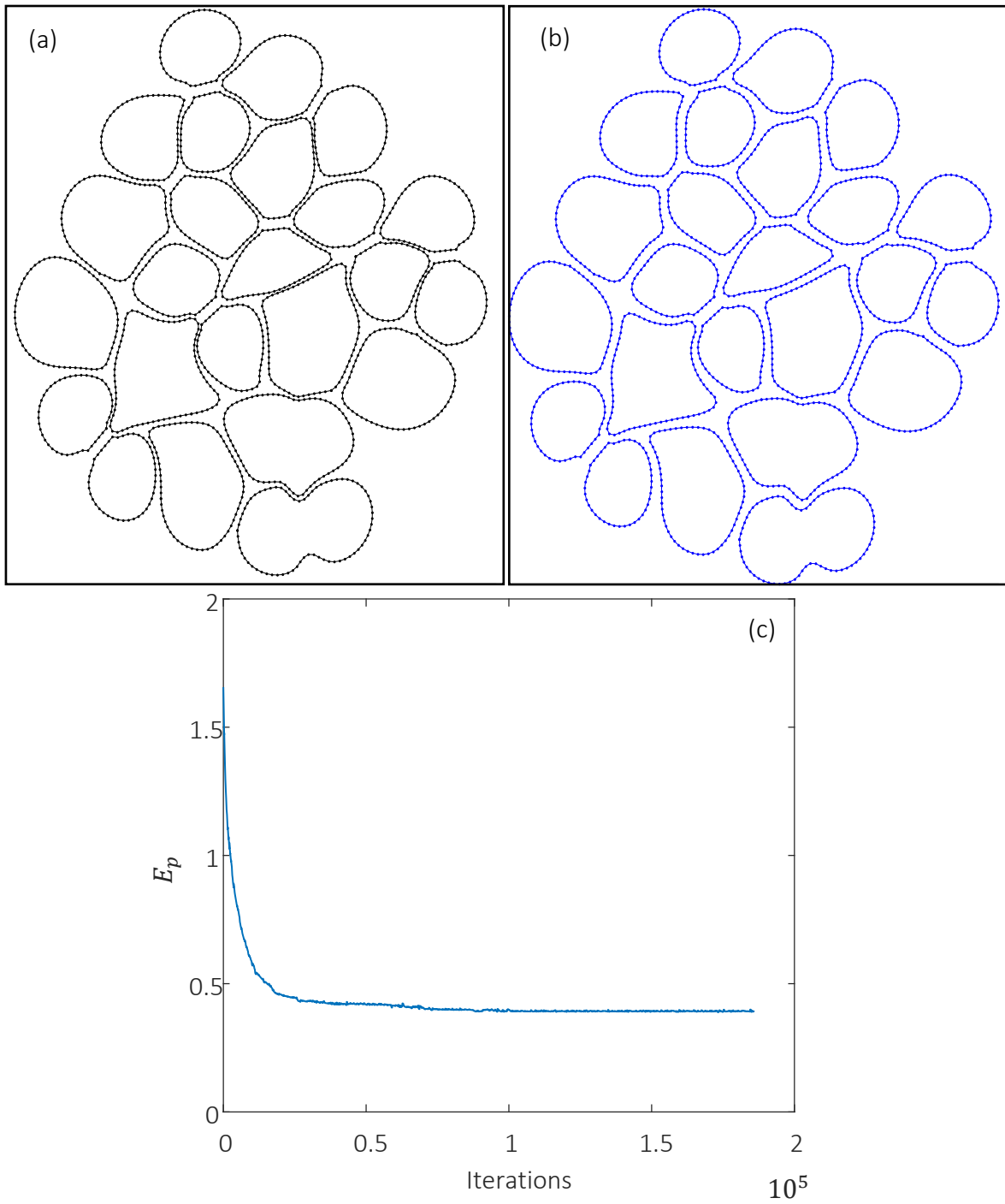


Figure 6.2 - Results obtained for the tissue consisting of 24 cells: (a) the structure of the tissue obtained without activating the optimization algorithm; (b) the structure of the tissue obtained as a result of activating the optimization algorithm. The potential energy stored within the tissue converged to its local minimum; (c) history of iteration evolution of the potential energy.

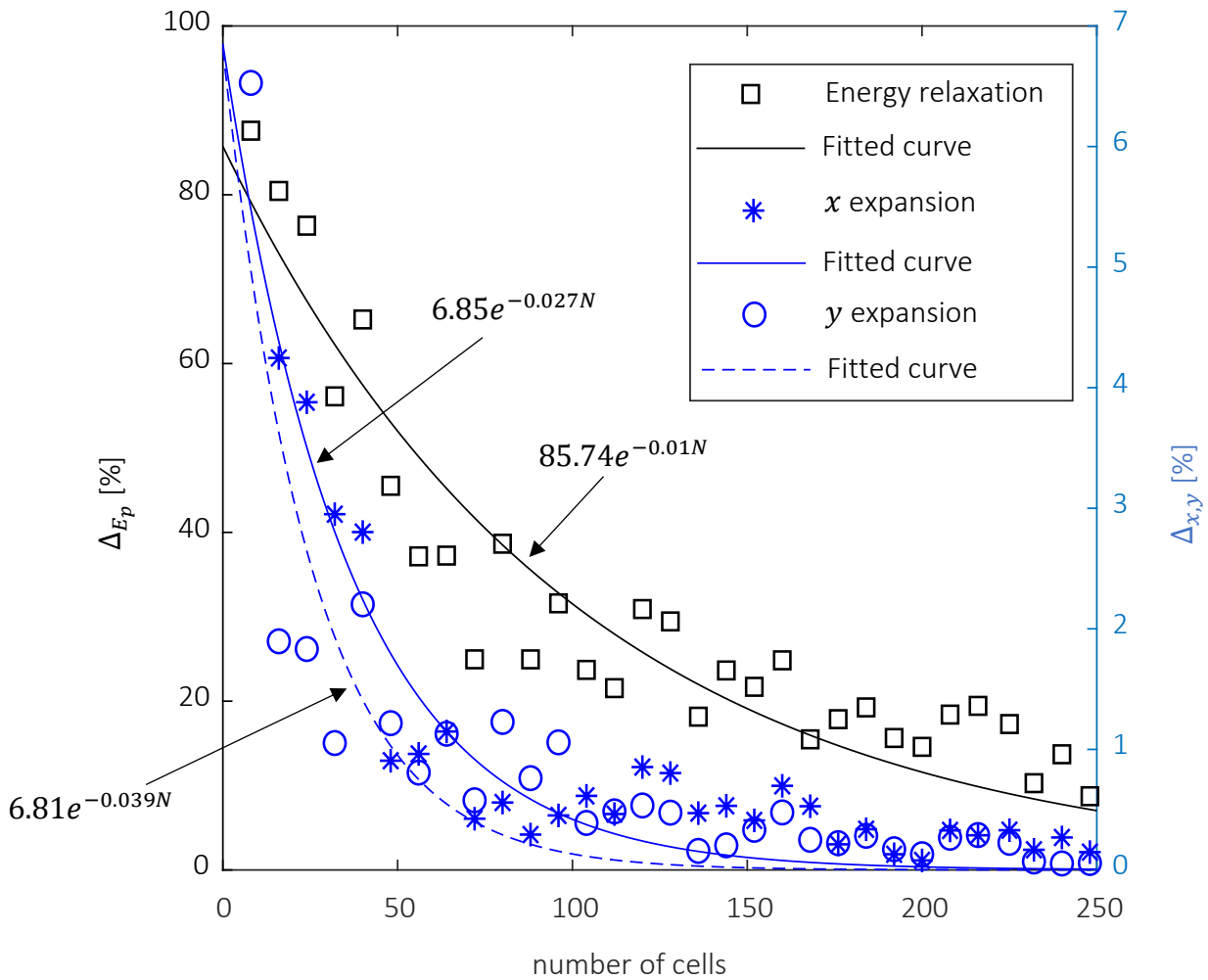


Figure 6.3 - The rate of energy decrease and the rate of spatial expansion of the tumor versus number of cells entering the tumor.

6.2. Numerical model for the cell heterogeneity

Experimental evidence provided by [42] indicates a small fraction of the tumor cells being involved into the cytokinesis process at any given time. Additionally, it has also been found that in big tumor the position of the cell within the tumor has an immediate impact on a probability of the cell to proliferate and on proliferation rate of the cell in a long term. At the same time in small tumors, the fraction of the mitotic cells was higher and their spatial distribution was more uniform compared to the corresponding characteristics observed in large tumors. Moreover, in large tumors, the cells characterized by high proliferating rate are more likely to be found next to the outer layer while in the intermediate

zone the slowly proliferating cells were recognized. In the current study we propose to correlate the proliferation rate of the mitotic cells with the criterion based on minimizing mechanical energy stored within the tumor and developed numerical framework supporting our hypothesis. In particular, we focussed on the analyzing the kinetic energy, since it was assumed that it makes the main contribution to the overall balance of internal energy during the active tumor development. Although the value of kinetic energy of a single cell may be very small (almost negligible) a criterion based on the value of kinetic energy is still meaningful as it is based on comparison of the kinetic energies of the neighboring cells, competing with each other for the growing space. Therefore the kinetic energy of a single cell is not negligible when compared to that of its neighbors.

6.2.1. Algorithm review

For a given tissue configuration, containing a given number of mitotic cells, we define the kinetic energy of each cell as follows:

$$e_{k_i} = \frac{1}{2} \rho A_i v_{c_i}^2, \quad (6.8)$$

where e_{k_i} is the kinetic energy of the i cell, ρ is the cell density, A_i is the area, and v_{c_i} is the velocity of the geometric center, respectively, of i^{th} cell. Note that we use the cell area instead of the cell volume because of 2D simulations. Therefore, the total kinetic energy of the entire tissue is given by:

$$E = \sum_{i=1}^N \frac{1}{2} \rho A_i v_{c_i}^2 \quad (6.9)$$

The kinetic energy is, among other things, an outcome of the source strength $\mathbf{s} = [s_1 \dots s_N]$ constituting the driven force throughout the simulation, where s_i has a binary value that is given by Eq. (2.2). Therefore, we use the gradient descent method to minimize the kinetic energy E_k by modifying the source terms. The gradient of the kinetic energy with respect to the source terms is given by:

$$\nabla E = \left(\frac{\partial E}{\partial s_1}, \dots, \frac{\partial E}{\partial s_i} \right) \quad (6.10)$$

For a given tissue configuration and mitotic state, the developed algorithm computes the energy gradient given by Eq.(6.10), and updates the source strength vector in a direction opposite to that of the energy gradient:

$$\begin{bmatrix} s_1 \\ \vdots \\ s_N \end{bmatrix}_{k+1} = \begin{bmatrix} s_1 \\ \vdots \\ s_N \end{bmatrix}_k - \alpha \frac{\nabla E}{|\nabla E|} , \quad (6.11)$$

where k is the iteration number.

We checked a number of successive values for α (see Eq.(6.12)) and continue to the next iteration with the value of α providing the fastest decrease of the kinetic energy.

$$\alpha = [0.1 \quad 0.5 \quad 1 \quad 2 \quad 4 \quad 8] \cdot \frac{s_{mitosis}}{20} \quad (6.12)$$

Note that the gradient ∇E_k is calculated for only currently active sources, i.e., the algorithm does not activate resting cells. For the i^{th} resting cell the gradient component ∇E_{k_i} is equal to zero. In addition, we applied two constraints on the source vector. The first constraint aims at limiting the maximum and minimum values allowed for individual source to 200% and 10% of the nominal value $s_{mitosis}$, respectively. The second constraint was introduced to preserve the constant value of the sum of all the source terms equal to its initial value when the algorithm was activated.

The first constraint is that an individual cell will not grow at an unrealistic rate. Indeed, an individual cell cannot grow with an infinite rate, regardless of energy considerations. Therefore, we restrict the upper bound of the source value. Additionally, in the current study we choose not to model shrinking of an individual cell ($s_i < 0$), which determines the lower bound of the source value. The second constraint is necessary to exclude convergence to the trivial solution $\mathbf{s} = [0 \dots 0]$ (or $|\mathbf{s}| \ll |\mathbf{s}_{initial}|$) satisfying the minimum of the kinetic energy. In addition, we want to preserve the global tumor growth rate (see Figure 5.5) that characterizes a realistic tumor proliferation.

The first constraint was implemented by defining the objective function $f(\mathbf{s})$, that needs to be minimized, with an additional penalty for individual sources that exceed the bottom and the upper limits:

$$f(\mathbf{s}) = E + \sum_i p_i, \quad (6.13)$$

where p_i is the penalty applied to exceeding sources given by:

$$p_i = \begin{cases} E_1 \cdot \frac{0.1 \cdot s_{mitosis} - s_i}{s_{mitosis}} & s_i < 0.1 \cdot s_{mitosis} \\ 0 & 0.1 \cdot s_{mitosis} \leq s_i \leq 2 \cdot s_{mitosis} \\ E_1 \cdot \frac{s_i - 2 \cdot s_{mitosis}}{s_{mitosis}} & s_i > 2 \cdot s_{mitosis}, \end{cases} \quad (6.14)$$

where E_1 is the total kinetic energy at the first iteration.

This penalty can affect the chosen value of α . If at any iteration one or more of the sources exceed one of the limits, the step along the gradient will be small so as not to exceed the bounds value even more. Once the source exceeds one of the limits, it will not participate in the next iteration, unless the corresponding gradient component returns the source back within the limits.

The second constraint was implemented by adding one more modification step to the basic algorithm. First, the sum of all the initial sources has been calculated before the algorithm activation:

$$s_{initial} \equiv \sum_i s_i^0 \quad (6.15)$$

Where s_i is the source term of the i cell, and the upper index 0 denotes the initial state.

The first step is similar to the basic gradient descent algorithm, the sources vector is updated in the opposite to gradient direction for each successive value of α_j , where the index j corresponds to one of the α values determined in Eq.(6.12). This time the obtained sources are stored in an intermediate array $\mathbf{s}_{k+\frac{1}{2}}^j$:

$$\mathbf{s}_{k+\frac{1}{2}}^j = \mathbf{s}_k - \alpha_j \frac{\nabla f_k}{|\nabla f_k|} \quad (6.16)$$

The obtained values $\mathbf{s}_{k+\frac{1}{2}}^j$ may not satisfy the constraint requiring constant value of sum of all sources, i.e.:

$$\sum_i \mathbf{s}_{k+\frac{1}{2}i}^j \neq S_{initial} \quad (6.17)$$

Then, the array of sources $\mathbf{s}_{k+\frac{1}{2}}^j$ is modified in order to maintain the constant value of sum of all sources $\sum_i \mathbf{s}_{k_i}^j = S_{initial}$. Two ways have been investigated for modifying the array of sources: the methodology of addition and multiplication. In the addition methodology the update has been made by adding to $\mathbf{s}_{k+\frac{1}{2}}^j$ the differences between the current sum $\sum_i \mathbf{s}_{k+\frac{1}{2}i}^j$ to $S_{initial}$:

$$\mathbf{s}_{k+1}^j = \mathbf{s}_{k+\frac{1}{2}}^j + \frac{S_{initial} - \sum_i \mathbf{s}_{k+\frac{1}{2}i}^j}{N} \cdot \boldsymbol{\delta} \quad (6.18)$$

Where N is the number of the participating sources and the addon is performed only to the components corresponding to the active sources using $\boldsymbol{\delta}$ vector, where:

$$\delta_i = \begin{cases} 1 & s_{k_i} \neq 0 \\ 0 & s_{k_i} = 0 \end{cases} \quad (6.19)$$

In the multiplication method the update has been made by multiplying $\mathbf{s}_{k+\frac{1}{2}}^j$ by the ratio between the $S_{initial}$ to the current sum $\sum_i \mathbf{s}_{k+\frac{1}{2}i}^j$:

$$\mathbf{s}_{k+1}^j = \mathbf{s}_{k+\frac{1}{2}}^j \cdot \frac{S_{initial}}{\sum_i \mathbf{s}_{k+\frac{1}{2}i}^j} \quad (6.20)$$

For both methods, after the modification step, the algorithm continues to the next iteration with the value of α_j providing the fastest decrease of the kinetic energy.

A comparison between the two methodologies can be seen in Figure 6.4. It can be seen that both methodologies provide similar results while utilizing the addition methodology provides much rapid convergence. For this reason, we used the addition methodology in all the further simulations.

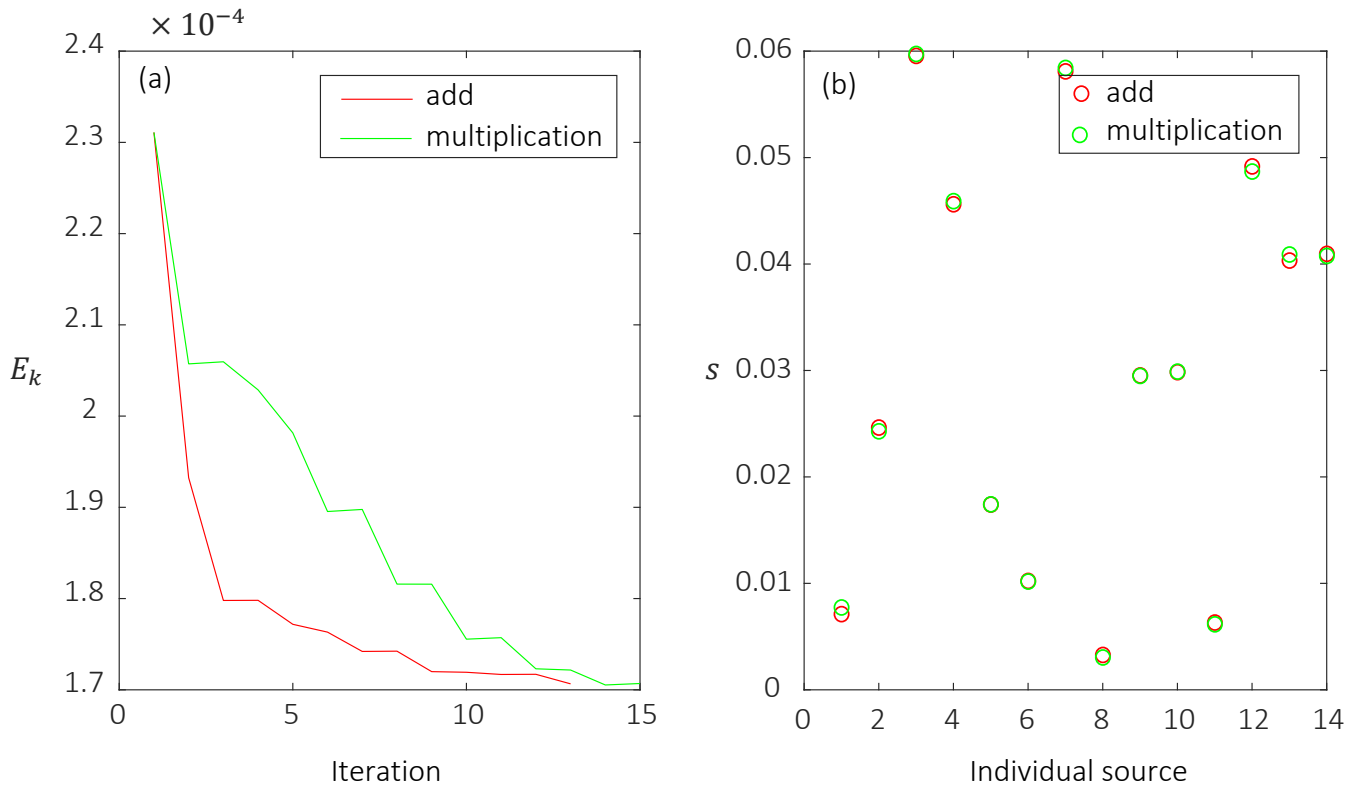


Figure 6.4 - Comparison between the addition and multiplication methodologies applied to the sources update: (a) convergence of the kinetic energy versus a number of iterations; (b) the final value of sources provided by both methodologies.

6.2.2. Algorithm summary:

Index legend:

- i index of a vector component
- k index for global iteration number
- j index for iterations on α value

Step 1: initializing:

$$E_1 = \sum_{i=1}^N \frac{1}{2} \rho A_i v_{c_i}^2$$

$$S_{initial} \equiv \sum_i s_i^0$$

Step 2: Global loop – promote \mathbf{s}_k using the constraint gradient descent algorithm:

Calculate the current objective function value:

$$f_k(\mathbf{s}_k) = \sum_{i=1}^N \frac{1}{2} \rho A_i v_{c_i}^2 + \sum_i p_i$$

Calculate the objective function gradient:

$$\nabla f_k = \left(\frac{\partial f_k}{\partial s_1}, \dots, \frac{\partial f_k}{\partial s_i} \right)$$

Inner loop – choose ($1 < j < 6$):

Step in the opposite to gradient direction:

$$\mathbf{s}_{k+\frac{1}{2}}^j = \mathbf{s}_k - \alpha_j \frac{\nabla f_k}{|\nabla f_k|}$$

Modify $\mathbf{s}_{k+\frac{1}{2}}^j$ for sum correction:

$$\mathbf{s}_{k+1}^j = \mathbf{s}_{k+\frac{1}{2}}^j + \frac{S_{initial} - \sum_i s_{k+\frac{1}{2}}^j}{N} \cdot \boldsymbol{\delta}$$

Calculate the obtained target function:

$$f_{k+1}^j(\mathbf{s}_{k+1}^j) = \sum_{i=1}^N \frac{1}{2} \rho A_i v_{c_i}^2 + \sum_i p_i$$

Continue to the next step with $(\mathbf{s}_{k+1}^j)_{min}$ that provides the minimum value for f_{k+1}^j :

$$\mathbf{s}_{k+1}^j = (\mathbf{s}_{k+1}^j)_{min}$$

Check convergence of E_k .

6.2.3. Results

The presently used set-up is similar to that used in chapter 5. The simulations were initiated with a single cell, and once the cell population reached more than 30 cells, the algorithm, detailed in the previous section, was activated. The algorithm modified the strength of the mitotic cells sources each time the cell population increased by 8 new cells. Simultaneously, the mitosis process continued in the growing tissue by activating the source of a randomly selected resting cell of the colony every 10 min, similar to the simulations in chapter 5.

The results yielded by a single activation of the algorithm are presented in *Figure 6.5*. At the time the algorithm was activated the tumor contained 232 cells in total, of which 35 were actively growing ($s_i > 0$) cells. When using the algorithm, the energy of the entire tissue converged after 4 iterations (see *Figure 6.5 (a)*). The source strengths before and after activation of the algorithm are shown in *Figure 6.5 (b)*. *Figure 6.5 (c)* shows the final state of entire tissue in which the resting cells and cells with accelerating and decelerating

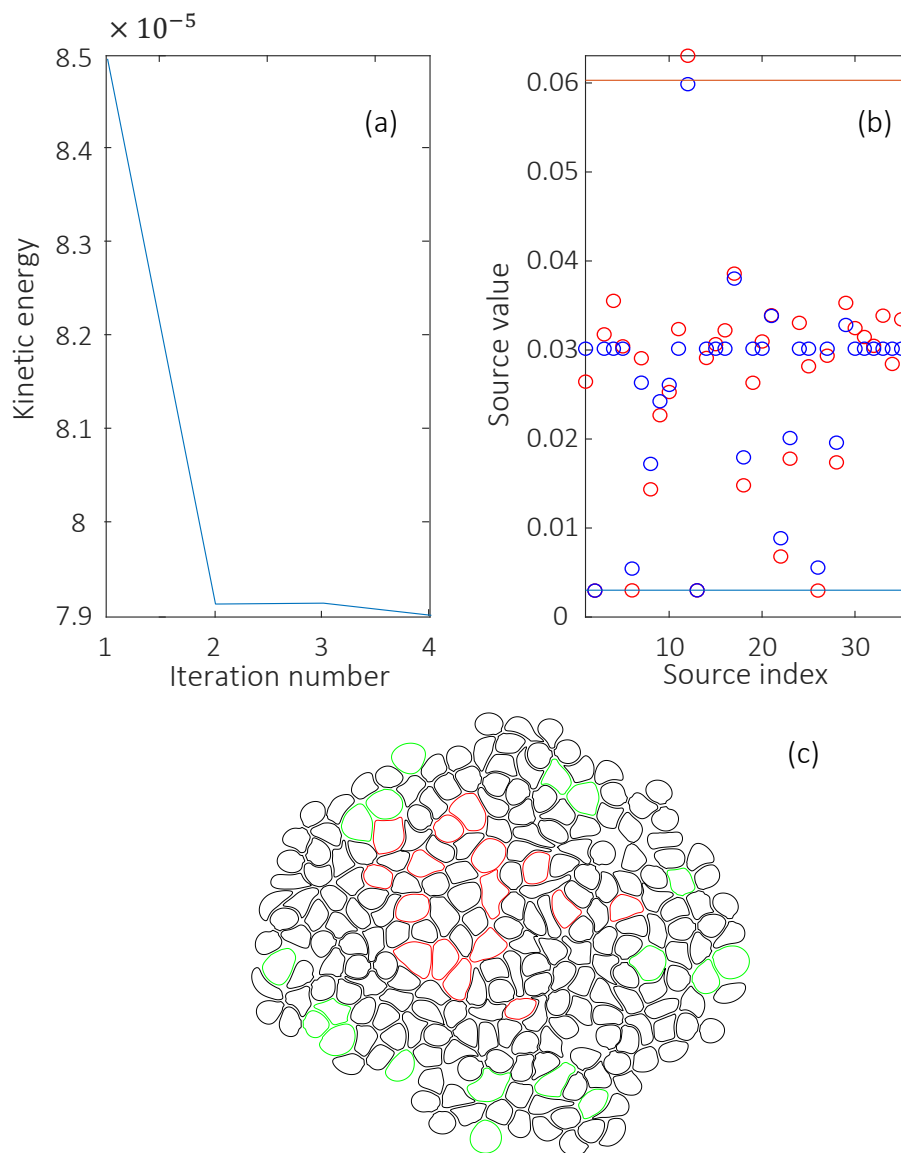


Figure 6.5 - Results yielded by a single activation of the algorithm for the tumor built of 232 cells: (a) kinetic energy versus number of iterations; (b) initial (blue circles) and terminal (red circles) values of the sources strength; (c) spatial distribution of the resting cells and the cells characterised by increased and decreased growth rate. Black, green and red cells are resting, accelerated and decelerated cells, respectively.

growth are highlighted in black, green, and red, respectively. It can be clearly seen that in general, the growth rate of cells located on the periphery of the tumor increased, while the growth rate of cells located in the center of the tumor decreased.

It should be noted that all the simulations of the tumor progression, performed in the framework of the current study, can be classified as an open system (i.e., system whose rigid boundaries do not contact with the periphery of the cell colony and the boundary effect on the cell colony is negligible). In such systems the cells at the periphery are larger than those deep inside the colony and can be characterized by using a cell size distribution function (SDF) [59]. The principles underlying the developed methodology do not allow to directly obtain a realistic SDF, since for simplicity we have not introduced a large scatter in the cell division criteria (a cell necessarily divides when its area is doubled). Instead, in order to validate the obtained numerical results with the experimental data we next introduce and analyze two equivalent quantitative metrics, namely, the time required for the cell to double its size (the doubling time hereafter) and the fraction of area occupied by mitotic cells relative to the total area of the tumor. Specifically, we investigate how both metrics depend on a distance from the tumor center which will allow us, albeit indirectly, to validate the developed methodology against experimental evidence.

Prior to taking each measurement, the entire tumor was bounded by an outer circle and partitioned into N regions, by circles of decreasing radius as shown in Figure 6.6 (which presents a specific example when the entire tumor is partitioned into 5 different regions). Throughout the simulation, the time that took for a cell to double its size and the location of that specific cell within the tumor have been monitored. The partition of the entire region occupied by tumor was performed each time one of the cells doubled in size. The average time, \bar{t}_k , needed for a specific cell to double its size as a function of its normalized distance (x/R) to the tumor center is shown in Fig. 6.7. Each point shown in Figure 6.7 corresponds to the doubling time value averaged over eight independently performed simulations. The scatter of the data at each point is indicated by the corresponding error bars.

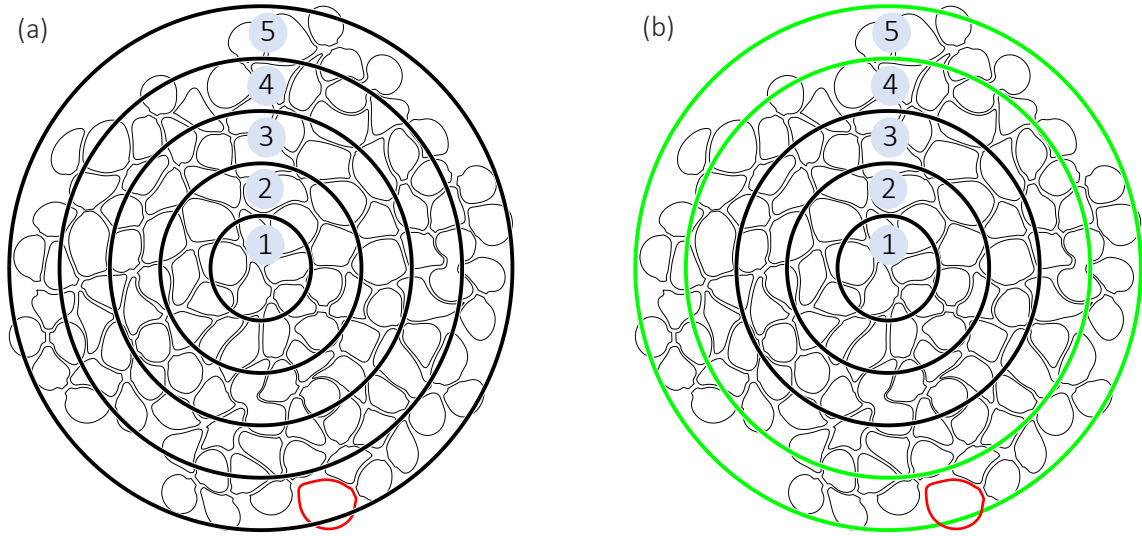


Figure 6.6 – Sample example for post-processing: (a) right after an individual cell doubled in size (red cell) the tumor is partitioned into n regions ($n=5$ in this example); (b) the algorithm detects in which region the cell center of mas is located (highlighted in green), and measures the time required to the cell to double in size (i.e. the doubling time). The measurement is then used to calculate the average doubling time in the detected region.

The scaling of the doubling time, $\bar{t}_{doubling}$ to the distance of the cell x from the tumor center normalized by the external radius of the tumor, R , was found by using the best fit to the decaying exponential function:

$$\bar{t}_{doubling} = 11.93e^{-1.073\frac{x}{R}} [h], \quad (6.21)$$

Note that R value changes all through the simulation.

It can be seen that the doubling time decreases with distance from the center of the tumor. Also, as shown in Figure 6.7, the scattering (error bars) of the doubling time values close to the tumor center is much higher than that typical of the tumor periphery. The above observation is consistent with the results obtained by applying an algorithm for a single activation of the tumor cell shown in Figure 6.5. In fact, the accelerating sources (belong to the cells at the periphery) are characterized by a lower scattering compared to that observed for the decelerating sources (belong to the cells close to the tumor center).

The scattering nonuniformity is apparently a consequence of the incompressibility constraint imposed on the liquid filling the cells and the ECM. In fact, it is clear that while growing, a mitotic cell located close to tumor center directly affects a much larger number of cells compared to its counterpart located at the periphery of the tumor. As a result, the

influence of a centrally located mitotic cell on the global energy of a tumor can differ significantly from tumor to tumor depending on the structure of a particular tumor. This observation explains the higher doubling time scatter, typical of centrally located mitotic cells.

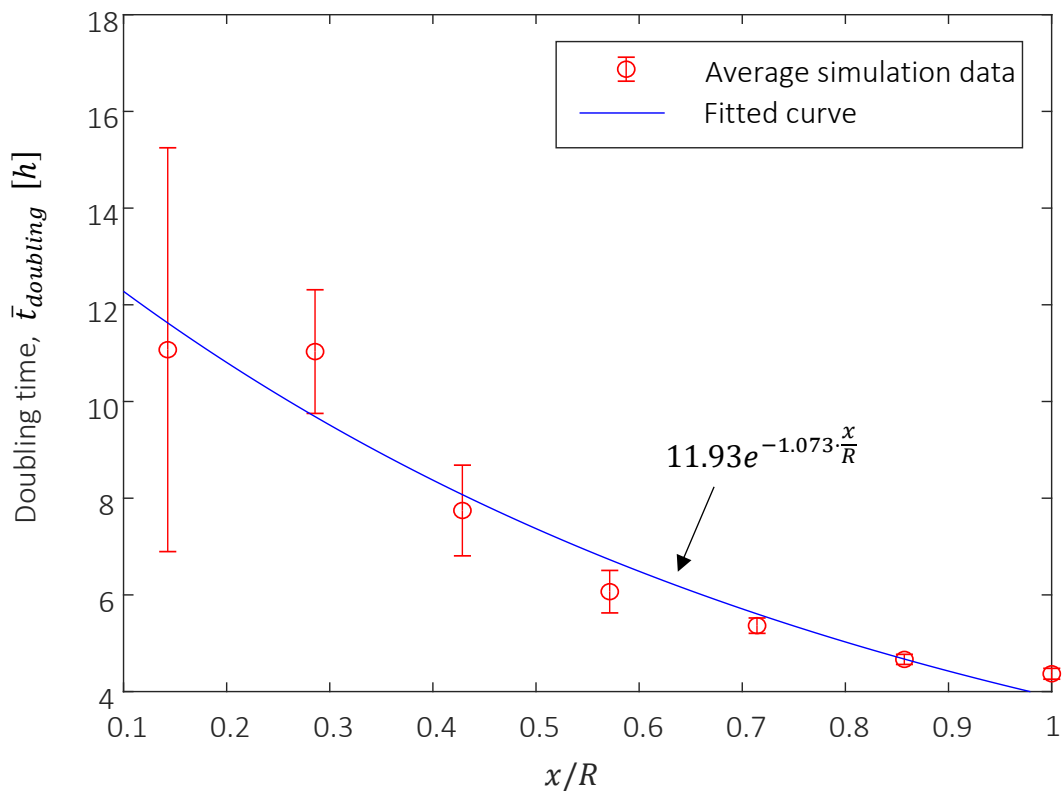


Figure 6.7 – Average doubling time obtained for 8 different simulations at different locations within the tumor (\circ), while the error bars represent the standard deviation of the results. The locations are normalized by the tumor radius, and the exponential fitted trendline (-).

We start with analyzing the number of cell divisions that occurred in each region, as a function of the normalized distance x/R of the region to the center of the tumor. The analysis is performed in order to demonstrate that the developed model can adequately reproduce the experimental results according to which, in open systems, cells located close to the tumor periphery have tendency to divide more frequently than cells located in the center.

Since each region has different area, it is reasonable to expect more divisions as the area of particular region increases, as a region with a larger area is more likely to contain more cells. However, at some distance, the number of cells per unit area decreases with the distance from the center of the tumor, which is sparser at its periphery (see Figure 6.8).

For this reason, the absolute number of cell divisions occurring in each region must be adequately normalized.

We next introduce universal normalization, which will allow us to compare between different regions in different tumors at any given time. Normalization of the absolute number of divisions, N_k that has occurred in region k , could be based on the total number of cells within that specific region $N_{k_{total}}$. However, the absolute number of cells within a specific region changes with time as the cells proliferate and the tumor expands. For this reason, the normalization based on the total number of cells only will not provide the ability to compare different tumors at different stages of development. Therefore, constant in time characteristic values should be sought for normalizing a number of cell divisions. The first characteristic value is the tissue fractional area ρ_k determined as the ratio of the area occupied by the tumor cells (highlighted in red in Fig. 6.8) to the total area of ring k (contains both cells and ECM, highlighted in blue in Fig. 6.8). In fact, during the tissue growth ρ_k approximately remains constant as shown in Figure 6.8 (b). The second characteristic value is the ratio between areas of different regions (rings) into which the tumor was partitioned. We therefore use both characteristics values to normalize the total number of cells $N_{k_{total}}$ within any region k in such a way that we can eliminate the dependence in time when comparing one region to another.

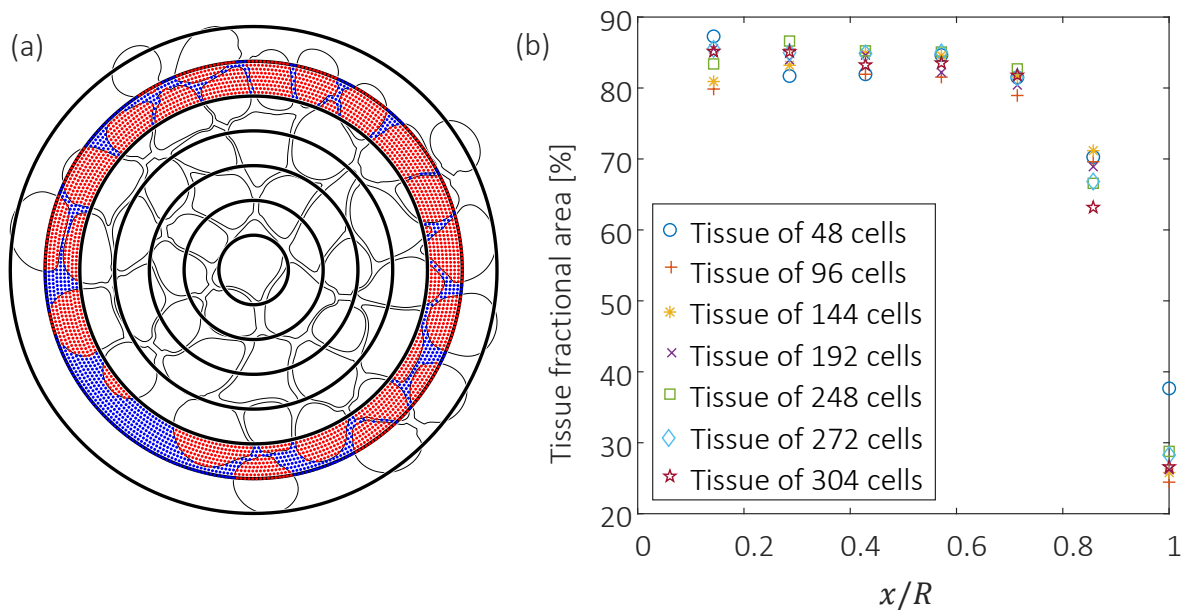


Figure 6.8 – (a) Visualization of the tissue fractional number with respect to a given partition. The area occupied by cells is highlighted in red, the area occupied by the ECM is highlighted in blue. The tissue fractional area ρ_k determined as the ratio of the area highlighted in red to the total

area of ring. (b) Tissue fractional area versus the distance from the center of the tumor. Results were obtained for tumor progression overtime for a single tumor.

First, we will establish the ratio between the area of two given regions (rings). When dividing the tumor into N regions, as described in Figure 6.6, the area of each region is given by:

$$s_k = \pi \left(\left(\frac{R}{N} k \right)^2 - \left(\frac{R}{N} (k-1) \right)^2 \right), \quad (6.22)$$

where R is the maximum radius of the tumor and $k = 1, 2 \dots N$.

Then, the ratio of the area of region k to the area of the first region ($k = 1$):

$$\frac{s_k}{s_1} = 2k - 1, \quad (6.23)$$

therefore, the area of region k (which is changing over time) is given by:

$$s_k(t) = (2k - 1)s_1(t). \quad (6.24)$$

The area occupied by the cells within region k (highlighted in red in Figure 6.8), can next be calculated by using the cells fractional area ρ_k and the region area $s_k(t)$:

$$s_{tissue_k} = s_k(t)\rho_k, \quad (6.25)$$

which can be rewritten by using Eq. (6.24) as:

$$s_{tissue_k}(t) = s_1(t)(2k - 1)\rho_k. \quad (6.26)$$

The total number of cells within the region k can be evaluated as a ratio between the area occupied by the cells and the average cell area \bar{s}_{cell} :

$$N_{k_{total}}(t) = \frac{s_{tissue_k}(t)}{\bar{s}_{cell}}, \quad (6.27)$$

which can be rewritten by using Eq. (6.26) as:

$$N_{k_{total}}(t) = \frac{s_1(t)(2k - 1)\rho_k}{\bar{s}_{cell}} \quad (6.28)$$

Next the number of mitotic cells per number of the total cells within region k at a specific time $n_k(t)$ can be calculated as:

$$n_k(t) = \frac{N_k}{N_{ktotal}(t)} = \frac{N_k}{\frac{s_1(t)(2k-1)\rho_k}{\bar{s}_{cell}}} \quad (6.29)$$

Normalizing the value obtained by Eq. (6.29) by the total number of mitotic cells summed over all the tumor eliminates the dependence on time (by $s_1(t)$), and the dependence on the average cell area \bar{s}_{cell} and yields the relative number of mitotic cells per total number of cells, as only a function of the distance from the center of the tumor:

$$\frac{n_k}{\sum_k n_k} \cdot 100\% = \frac{\frac{N_k}{s_1(t)(2k-1)\rho_k}}{\frac{\bar{s}_{cell}}{\sum_k \frac{N_k}{s_1(t)(2k-1)\rho_k}}} \cdot 100\% = \frac{\frac{N_k}{(2k-1)\rho_k}}{\sum_k \frac{N_k}{(2k-1)\rho_k}} \cdot 100\% \quad (6.30)$$

Relative part of mitotic cells per tumor area versus the distance from the center of the tumor is shown in Figure 6.9 . It can be recognized that despite the random mitosis initiation, the relative number of mitotic cells per total number of cells increases with the distance from the center of the tumor and was found by using the best fit to the quadratic function:

$$\frac{n_k}{\sum_k n_k} = -3.4 \left(\frac{x}{R}\right)^2 + 11.87 \left(\frac{x}{R}\right) + 8.92 \quad (6.31)$$

The obtained result is consistent with experimental observations indicating that there are more mitotic cells at the tumor periphery compared to its center.

To sum up, it was demonstrated that the developed model can consistently reproduce two major experimental observations indicating, higher growth rate of the cells and higher number of mitotic cells at the tumor's periphery compared to its center. Note that the obtained trends were reproduced by solely basing on principles of finding a local minimum of the mechanical energy of the tumor and not an outcome of any explicitly made assumptions. This insight suggests a strong correlation between purely mechanistic characteristics and biologic events determining the tumor cells progression and proliferation.

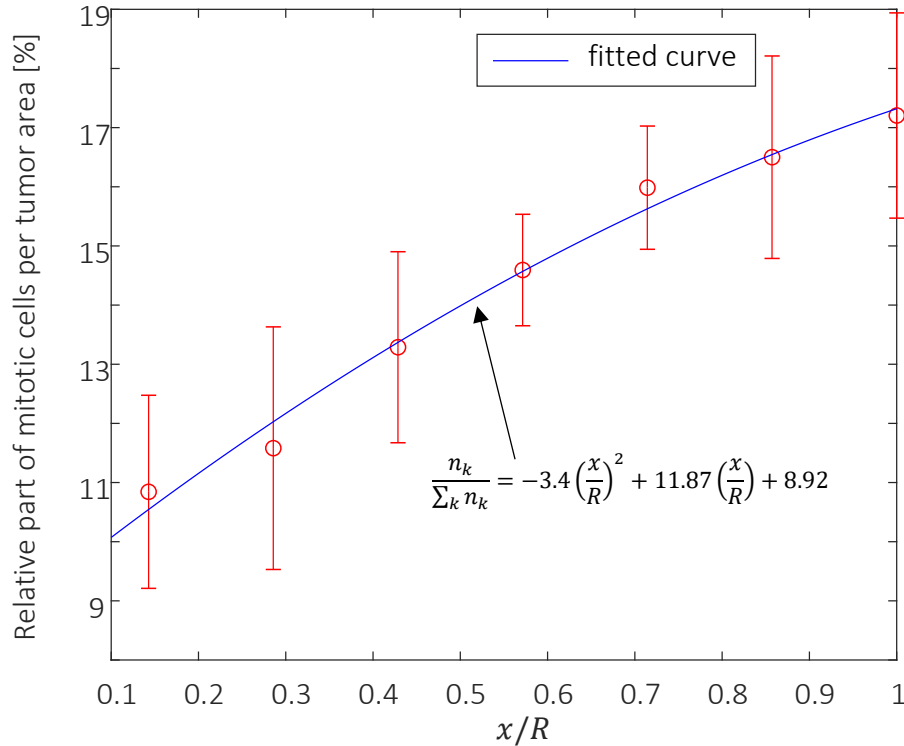


Figure 6.9 – Relative part of mitotic cells per tissue area as a function of the distance from the center of the tumor. Results represent the average value of 6 simulations.

6.3. Energetic prioritization for mitosis initiation

In addition to the spatial variability in the growth rate of individual cells, a biological data points to the formation of fingers as one of the main characteristics of growing tumor [60], [17], [61] and plays a key role in the tumor invasive ability. The cells developing within the tumor are divided into two groups: “followers” and “leaders” [62], [17]. Leader cells are more often located on the periphery of the tumor and orient the direction and speed of the tumor development. The mechanism responsible for the selection of these cells remains to be elucidated.

In [32] a nutrient-driven-grow is presented as a mechanism that creates the fingering formation. A uniform distribution of nutrients is set at the beginning of the simulation inside the computational domain, and the growth rate of each individual cell depends on the nutrient concentration level around it. As a cell grows, the nutrient stock around it decreases as a limited resource. This setup, at some point, allows only to the peripheral cells to grow because nutrients are available only near the outside boundaries of the tumor.

In the current study we propose an alternative model for the fingering formation observed at the periphery of a growing tumor. The key idea is that the unevenness of mitosis initiation during tumor growth is not a random process, as was previously assumed, rather it correlates with the energetic state of the entire tumor, tending to minimum increase in its kinetic energy. As in the previous simulations, in our model mitosis is initiated every 10 minutes, with the only difference being that the cell undergoing mitosis at the given moment is chosen to provide the minimum increase in the kinetic energy of the growing tumor.

Results provided by using the above algorithm can be seen in Figure 6.10. Along the periphery of the tumor a fingering pattern can be clearly recognized, which is a direct consequence of mitosis initiation by cells located on the periphery of the tumor.

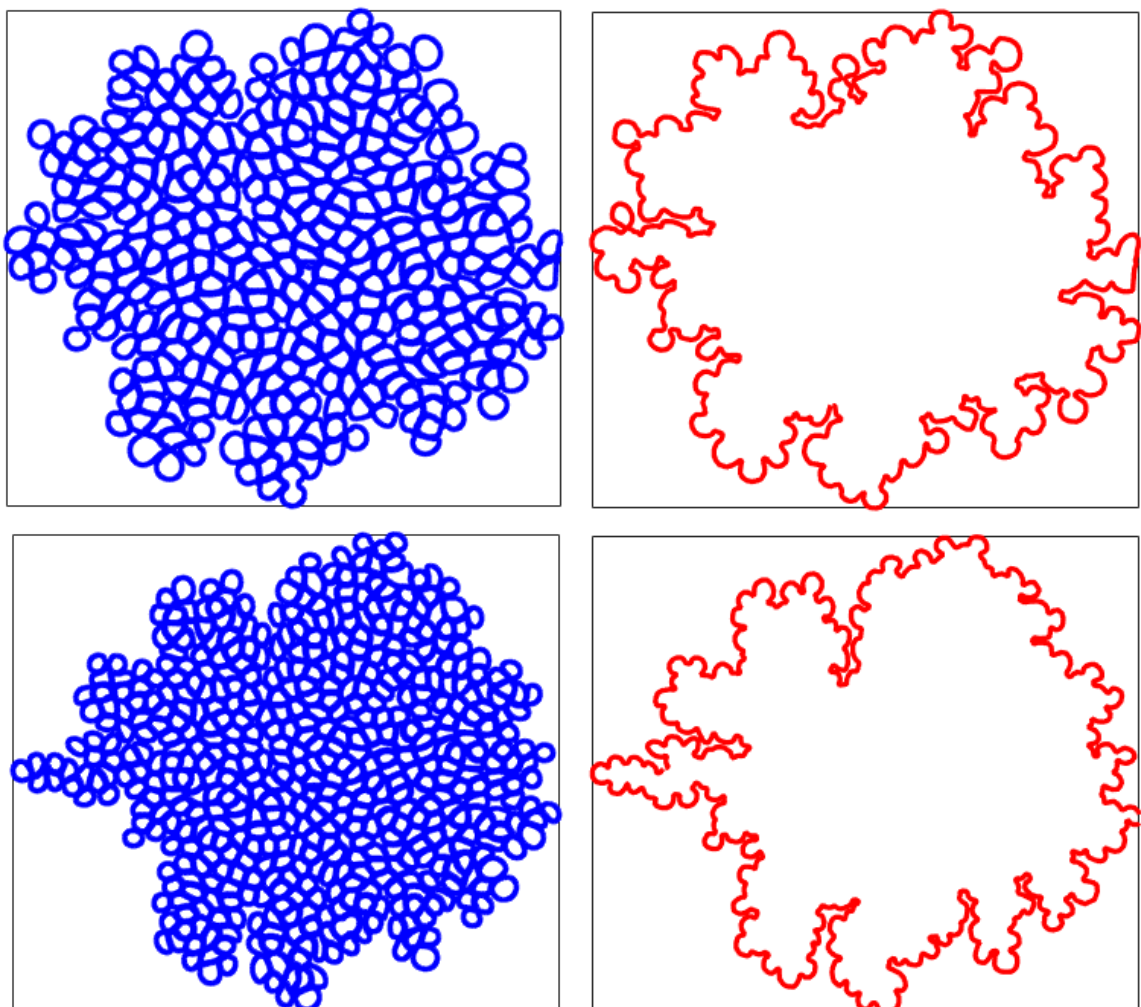


Figure 6.10 - Digital image of the tumor obtained using the mechanism of mitosis initiation based on ensuring the minimum increase in tumor kinetic energy. Top row: tumor containing 359 (left)

and the outer contour of the tumor (right). Bottom row: tumor containing 521 (left) and the outer contour of the tumor (right).

Summing up, the obtained fingering pattern is a direct consequence of a biased initiation of mitosis, which mainly occurred at the periphery of the tumor. Important that in the current study such a biased initiation is determined solely by the energy considerations, namely, by finding a local minimum of the kinetic energy of the developing tissue. In fact, as a result of incompressibility constraint cells located close to the tumor center would have to affect much more neighboring cells when growing compared to their counterparts located close to the periphery of the tumor. Therefore, mitosis initiation of cells within the center of the tumor will result in higher contribution to the total kinetic energy of the tumor compared to the contribution of cells located at the tumor's periphery.

7. Summary and conclusions

In the framework of the current study, a rheological model for the tumor cell progression was developed. The developed model includes a deformable cell model (DCM), based on the solution of the Navier-Stokes equations for an incompressible Newtonian fluid filling the cells and the ECM. Intercellular interactions as well as the elastic behavior of the cell membrane are modeled at the mesoscale level by utilizing IBM.

The developed model is able to simulate the growth and proliferation of cells. Cell growth is carried out by introducing distributed fluid sources in the geometric center of the growing cell, which leads to expansion of the cell membrane due to the incompressibility of the fluid. Surface tension, cytokinesis, and mechanosensory interaction with the environment are modelled by basing on constitutive body forces, generated by linear springs connecting both the points that form the cell membrane and neighboring cells in order to mimic cohesive forces within tumor tissue.

The incompressible Navier-Stokes equations were solved by in-house developed solver incorporating IBM capabilities. The solver utilizes standard second order finite volume and second order backward finite difference schemes for spatial and temporal discretization, respectively. The pressure-velocity coupling was performed by utilizing the SIMPLE approach. The developed solver was extensively verified by comparing the results obtained for several representative one and two-phase flows with the corresponding data available in the literature.

The model based on the developed solver has been extensively validated by comparing the characteristics of numerically modelled tumors with data available in the literature. In particular, the focus was on validating area conservation after cell division, the amount of time required for cell area doubling, the duration of the cytokinesis process, and the temporal evolution of the proliferation process and tumor area. All the above characteristics are closely related to accurate imposing the incompressibility constraint of the developed NS solver, and to the adequate implementation of cell growth, as well as the cytokinesis and division algorithms utilized in our model.

Finally, a novel self-consistent approach based on finding the local minimum of mechanical energy stored in the tumor tissue using the gradient descent method was

developed to control cell proliferation within a tumor. The minimum of mechanical energy of the tissue was sought by basing on two different criteria. The first criterion is a local minimum of the kinetic energy calculated by basing on the source strength values distributed over already growing individual cells within the tumor. The second criterion is to a local minimum of the kinetic energy calculated by basing on the choice of specific cells for mitosis initiation. It has been shown that cells located near the borders of the tumor grow and divide at a much higher rate than those located within the center of the tumor.

The numerical results obtained by using the first criterion consistently confirm the experimental results postulating that, in open systems, cells at the periphery proliferate at higher rate and are larger than cells deep inside the colony. At the same the numerical data obtained by using the second criterion has successfully reproduced fingering formation for the tumor periphery, being an inherent feature of the tumor and characterizing its invasive ability. The results obtained provide an alternative explanation based on the fully mechanistic approach of not yet fully understood mechanism responsible for the choice of the “leader” cells that determine the direction of tumor growth.

8. Bibliography

- [1] R. Rosen, "Biological Systems as Paradigms for Adaptation," in *Adaptive economic models*, Academic Press, 1975, pp. 39-72.
- [2] D. Ishay-Ronen and G. Christofori, "Targeting Cancer Cell Metastasis by Converting Cancer Cells into Fat," *Cancer Research*, vol. 79, no. 21, pp. 5471-5475, 2019.
- [3] A. N. Brooks, S. Turkarslan, K. D. Beer, F. Yin Lo and N. S. Baliga, "Adaptation of cells to new environments," *Wiley Interdiscip Rev Syst Biol Med*, vol. 10.1002/wsbm.136, p. 544–561, 2011.
- [4] J. Berg, J. Tymoczko and L. Stryer, *Biochemistry*. 5th edition., New York: W H Freeman, 2002.
- [5] S. Valastyan and R. Weinberg, "Tumor Metastasis: Molecular insights and evolving paradigms," *Cell*, vol. 147(2), p. 275–292, 2011.
- [6] A. Lambert, D. Pattabiraman and R. A. Weinberg, "Emerging biological principles of metastasis," *Cell*, vol. 168(4), p. 670–691, 2017.
- [7] M. L. De Ieso and A. J. Yool, "Mechanisms of Aquaporin-Facilitated Cancer Invasion and Metastasis," *frontiers in chemistry*, vol. 6, no. 135, 2018.
- [8] M. Nieto, R. Huang, . R. Jackson, and J. Thiery, "EMT:2016," *Cell*, vol. 166, p. 21–45, 2016.
- [9] O. Ocana , R. Corcoles , A. Fabra , G. Moreno-Bueno, H. Acloque, S. Vega, A. Barrallo-Gimeno, A. Cano and M. Nieto, "Metastatic colonization requires the repression of the epithelial-mesenchymal transition inducer Prrx1," *Cancer Cell*, vol. 22, p. 20, 2012.
- [10] J. Tsai, J. Donaher, D. Murphy, S. Chau and J. Yang , "Spatiotemporal regulation of epithelial-mesenchymal transition is essential for squamous cell carcinoma metastasis,," *Cancer Cell*, vol. 22, p. 725–736, 2012.

- [11] J. Tsai and J. Yang, "Epithelial–mesenchymal plasticity in carcinoma metastasis," *Genes Dev*, vol. 27, p. 2192–2206, 2013.
- [12] R. Kalluri and R. A. Weinberg, "The basics of epithelial-mesenchymal transition," *the journal of clinical investigation*, vol. 119, no. 6, pp. 1420-1428, 2010.
- [13] E. Gomez, Q. Chen , N. Gjorevski and C. Nelson, "Tissue geometry patterns epithelial-mesenchymal transition via intercellular mechanotransduction," *J. Cell Biochem.*, vol. 110, p. 44–51., 2010.
- [14] A. Puliafito, L. Hufnagel, P. Neveu, S. Streichan, A. Sigal, D. Fygenson and B. Shraiman, "Collective and single cell behavior in epithelial contact inhibition," *Proc. Nat. Ac. Sci.*, vol. 109, p. 739–744, 2012.
- [15] B. Rouzair-Dubois, M. Malo, J. Milandri and J. Dubois, "Cell size-proliferation relationship in rat glioma cells," *Glia Vol.*, vol. 45, p. 249–257, 2004.
- [16] T. E. Angelini, E. Hannezo, X. Trepap, . J. J. Fredberg and D. A. Weitz, "Cell Migration Driven by Cooperative Substrate Deformation Patterns," *PHYSICAL REVIEW LETTERS*, 2010.
- [17] M. Reffay, L. Petitjean, S. Coscoy, E. Grasland-Mongrain, F. Amblard, A. Buguin and P. Silberzan, "Orientation and Polarity in Collectively Migrating Cell Structures: Statics and Dynamics," *Biophysical Journal*, no. 100, p. 2566–2575, 2011.
- [18] X. Trepap, M. Wasserman,, T. Angelini, E. Millet, D. Weitz, J. Buler and J. Fredberg, "Phusical forces firing collective cell migration," *Nature Phys*, vol. 5, p. 426–430, 2009.
- [19] D. Tambe, U. Croutelle, X. Trepap, C. Park, J. Kim, E. Millet, K. Butler and J. Fredberg , "Monolayer stress microscopy: Limitations, artifacts, and accuracy of recovered intercellular stresses," *PLoS One*, no. 8:e55172., 2013.
- [20] D. Tambe, U. Croutelle, X. Trepap, C. Park, J. Kim, E. Millet, K. Butler and J. Fredberg, "Monolayer stress microscopy: Limitations, artifacts, and accuracy of recovered intercellular stresses," *PLoS One*, p. 8:e55172, 2013.

- [21] J. Zimmermann, R. Hayes, M. Basan, J. Onuchic, W. Rappel and H. Levine, "Intercellular stress reconstitution from traction force data," *Biophys J.*, vol. 107, pp. 548-554., 2014.
- [22] S. Ishihara and K. Sugimura, "Bayesian inference of force dynamics during morphogenesis," *J. Theor. Biol.*, vol. 313, p. 201–211, 2012.
- [23] V. Nier, S. Jain, C. Lim, S. Ishihara, B. Ladoux and P. Marcq, "Inference of internal stress in a cell monolayer," *Biophys. J.*, vol. 110, p. 1625–1635, 2016.
- [24] M. Basan, T. Risler, J. Joanny, X. Sastre-Garau and J. Prost,, "Homeostatic competition drives tumor growth and metastasis nucleation.," *HFSP J.*, vol. 3, p. 265–272., 2009.
- [25] X. Yang, M. Manning and M. Marchetti, "Aggregation and segregation of confined active particles," *Soft Matter*, vol. 10, p. 6477–6484, 2014.
- [26] B. Álvarez-González, E. Bastounis, R. Meili, J. Álamo, R. Fritel and J. Lasheras, "Cytoskeletal mechanics regulating amoeboid cell locomotion," *Appl. Mech. Rev.*, vol. 66, p. 050804, 2014.
- [27] A. Harris, L. Peter, J. Bellis, B. Baum, A. Kabla and G. Charras,, "Characterizing the mechanics of cultured cell monolayers," *Proc. Natl Acad. Sci.*, vol. 109, p. 16449–16454, 2012.
- [28] N. Khalilgharibi, J. Fouchard, N. Asadipour, R. Barrientos, M. Duda, A. Bonfanti , A. Yonis, A. Harris, P. Mosaffa, Y. Fujita, A. Kabla , Y. Mao, B. Baum, J. Munoz, M. Miodownik and G. Charras, "Stress relaxation in epithelial monolayers is controlled by the actomyosin cortex.," *Nat. Phys*, vol. 15, p. 839–847, 2019.
- [29] J. Colombelli and J. Solon, "Force communication in multicellular tissues addressed by laser nanosurgery," *Cell Tissue Res.*, vol. 352, p. 133–147, 2013.
- [30] M. Gómez-González, E. Latorre, M. Arroyo and X. Trepap, "Measuring mechanical stress in living tissues," *Nature Phys*, vol. 2, p. 300–317, 2020.

- [31] P. Liedekerke, M. Palm, N. Jagiella and D. Drasdo, "Simulating tissue mechanics with agent-based models: concepts, perspectives and some novel results," *Comp.Part.Mech.*, vol. 2, p. 401–444, 2015.
- [32] K. K. Rejniak, "An immersed boundary framework for modelling the growth of individual cells: An application to the early tumour development," *Jurnal of Theoretical Biology*, no. 247, pp. 186-204, 2007.
- [33] K. Rejniak and A. Anderson, "A Computational Study of the Development of Epithelial Acini: I. Sufficient Conditions for the Formation of a Hollow Structure," *Bulletin of Mathematical Biology*, vol. 70, pp. 677-712, 2008.
- [34] R. Dillon and M. Owen, "A single-cell-based model of multicellular growth using the immersed boundary method," *AMS Contemp Math*, vol. 466, p. 1–15, 2008.
- [35] D. Staple, R. Farhadifar, J. Roper, B. Aigouy, S. Eaton and F. Julicher, "Mechanics and remodeling of cell packings in epithelia," *Eur. Phys. J. E. Soft Matter*, vol. 33, p. 117–127, 2010.
- [36] R. Farhadifar, J. Roper, B. Aigouy, S. Eaton and F. Julicher, "The influence of cell mechanics, cell-cell interactions, and proliferation on epithelial packing," *Curr. Biol.*, vol. 17, p. 2095–2104., 2007.
- [37] D. Barton, S. Henkes, C. Weijer and R. Sknepnek, "Active vertex model for cell resolution description of epithelial tissue mechanics," *PLoS Comput. Biol.*, vol. 13, p. e1005569., 2016.
- [38] D. Bi, X. Yang, M. Marchetti and M. Manning, "Motility-driven glass and jamming transitions in biological tissues.," *Phys. Rev. X*, vol. 6, p. 021011, 2016.
- [39] X. Yang, D. Bi, M. Czajkowski, M. Merkel, M. Manning and M. Marchetti, "Correlating cell shape and cellular stress in motile confluent tissues," *Proc. Natl. Acad. Sci.*, vol. 114, p. 12663–12668., 2017.

- [40] D. Fedosov, B. Caswell and G. Karniadakis, "Systematic coarse-graining of spectrin-level red blood cell models," *Comput. Methods Appl. Mech. Eng.*, vol. 199, p. 1937–1948., 2010.
- [41] G. Tryggvason, R. Scardovelli and S. Zaleski, Direct numerical simulations of gas-liquid multiphase flows, Cambridge University Press, 2011.
- [42] R. SUTHERLAND, . J. McCREIDIE and . R. INCH, "Growth of Multicell Spheroids in Tissue Culture as a Model of Nodular Carcinomas," *Journal of the National Cancer Institute*, no. 46, pp. 113-120, 1971.
- [43] M. Glotzer, "The Molecular Requirements for Cytokinesis," *SCIENCE*, no. 307, pp. 1735-1739, 2005.
- [44] G. Batchelor, An Introduction to Fluid Dynamics, Cambridge: Cambridge Mathematical Library Edition, Cambridge University Press, 2000.
- [45] T. J. Chung, Computational fluid dynamics, Cambridge university press, 2010.
- [46] P. Charles, "The immersed boundary method," *Acta Numerica*, pp. 479-517, 2002.
- [47] A. M. Roma, C. S. Peskin and M. J. Berger, "An Adaptive Version of the Immersed Boundary Method," *Journal of Computational Physics*, vol. 153, p. 509–534, 1999.
- [48] U. Ghia, K. N. Ghia and C. Shin, "High-Re Solutions for Incompressible Flow Using the Navier-Stokes Equations and a Multigrid Method*," *Journal of Computational Physics*, no. 48, pp. 387-411, 1982.
- [49] T. Kuniyiko and C. Tim, "The immersed boundary method: A projection approach," *Journal of Computational Physics*, no. 225, pp. 2118-2137, 2007.
- [50] P. Koumoutsakos and A. Leonard, "High-resolution simulations of the flow around an impulsively started cylinder using vortex methods," *J. Fluid Mech*, no. 296, pp. 1-38, 1995.

- [51] G. Cottet, P. Koumoutsakos and M. Salihi, "Vortex methods with spatially varying cores," *J. Comput. Phys.*, no. 162, p. 164–185, 2000.
- [52] X. Yang, Z. Xing, L. Zhilin and H. Guo-Wei, "A smoothing technique for discrete delta functions with application to immersed boundary method in moving boundary simulations," *Journal of Computational Physics*, vol. 228, p. 7821–7836, 2009.
- [53] C. S. O'Hern, L. E. Silbert, A. J. Liu and S. R. Nagel, "Jamming at zero temperature and zero applied stress: The epitome of disorder," *PHYSICAL REVIEW*, no. 68, 2003.
- [54] T. Chinyoka, Y. Renardy, M. Renardy and D. Khismatullin, "Two-dimensional study of drop deformation under simple shear for Oldroyd-B liquids," *Journal of Non-Newtonian Fluid*, no. 130, pp. 45-56, 2005.
- [55] A. Spizzichino, S. Avihai and Y. Feldman, "The Immersed Boundary Method: Application to Two-Phase Immiscible Flows," *Commun. Comput. Phys.*, no. 25, pp. 107-134, 2018.
- [56] V. M. Laurent, E. Planus, R. Fodil and . D. Isabey, "Mechanical assessment by magnetocytometry of the cytosolic and cortical cytoskeletal compartments in adherent epithelial cells," *Biorheology*, no. 40, pp. 235-240, 2003.
- [57] M. Dembo and H. Francis, "Cell motion, contractile networks, and the physics of interpenetrating reactive flow," *Biophys. J.*, vol. 50, pp. 109-121, 1986.
- [58] Ultman, James; Baskaran, Harihara; Saidel, Gerald;, *Biomedical Mass Transport and Chemical Reaction: Physicochemical Principles and Mathematical Modeling*, New Jersey: Wiley, 2016.
- [59] E. Khain and L. Tsimring, "Effective pressure and cell area distribution in a confined monolayer," *Fluid Dynam. Res.*, vol. 50, p. 051413, 2018.
- [60] A. Anderson, K. Rejniak, P. Gerlee and V. Quaranta, "Microenvironment driven invasion: a multiscale multimodel investigation," *Journal of mathematical biology*, vol. 54, pp. 579-624, 2009.

- [61] M. J. Bogdan and T. Savin, "Fingering instabilities in tissue invasion: an active fluid model," *Royal Society open science*, 2018.
- [62] S. A. Vilchez Mercedes, F. Bocci, H. Levine, J. N. Onuchic, M. K. Jolly and P. K. Wong, "Decoding leader cells in collective cancer invasion," *Nature*, no. 21, pp. 592-603, 2021.
- [63] V. Labi and M. Erlacher, "How cell death shapes cancer," *Nature*, 2015.
- [64] S. Hysing, S. Turek, D. Kuzmin, N. Parolini, E. Burman, S. Ganesan and L. Tobiska, "Quantitative benchmark computations of two-dimensional," *INTERNATIONAL JOURNAL FOR NUMERICAL METHODS IN FLUIDS*, no. 60, p. 1259–1288, 2009.

תוכן עניינים

3	תקציר
4	תודות
5	תוכן עניינים
7	רשימת איורים
9	רשימת טבלאות
10	רשימת סימנים
12	1. מבוא
19	2. רקע תיאורטי
20	2.1. מידול של תא בודד בתוך רקמה מתפתחת
21	2.1.1. גדילה של תא בודד
26	2.2. משוואות שולטות
28	2.1.4. נרמול של קבועי הקפיצים
29	2.2. שיטות נומריות
29	2.2.1. פונקציית הדלתא של דיראק הדיסקרטית
30	2.2.2. אינטרפולציה ורגולריזציה
31	2.2.3. אלגוריתם SIMPLE
32	2.2.4. דיסקריטיזציה בשימות שיטת נפחים סופיים
35	2.2.5. Immersed boundary method (IBM)
37	2.2.6. Gradient decent
37	2.2.7. מודל לזרימה דו-פאזית
44	3. חקר וריפיקציה
44	3.1. LID-DRIVEN CAVITY FLOW
50	3.2. זרימה סביב גליל
52	3.3. GRADIENT DESCENT
57	3.4. זרימה דו-פאזית – בועה בגזירה
59	4. חקר פרמטרי

59	חזלוציית רישות	4.1.
61	כיוול ציטוקינזיס	4.2.
62	כיוול קצב גדילת תא	4.3.
62	פרמטרים שולטים	4.4.
65	חקר ולידציה, תוצאות ומסקנות	5.
66	שימור שטח לאחר חלוקת התא	5.1.
66	זמן הכפלת שטח של תא בגדילה	5.2.
67	משך תהליך הציטוקינזיס	5.3.
68	ריבוי התאים והתפתחות הגידול לאורך זמן	5.4.
70	תכנון ואנליזה נומרית של הרקמה הביולוגית	6.
70	רילקסציה של אנרגיית הגידול	6.1.
75	מודל נומרי להטרוגניות התאים	6.2.
76	פיתוח האלגוריתם האלגוריתם	6.2.1.
80	סיכום אלגוריתם	6.2.2.
81	תוצאות	6.2.3.
89	תיעדוף אנרגטי עבור תחילת תהליך המיטוזה	6.3.
92	סיכום ומסקנות	7.
94	ביבליוגרפיה	8.

תקציר

שגשוג של גידול תאי ושליחת גרורות הן תופעות מורכבות, הכוללות שינויים מולקולריים ותאיים מתמשכים. למרות התקדמות משמעותית שהושגה בהבנת התהליכים הביולוגיים והגנטיים המניעים את התופעות הללו, ישנו פער גדול הנדרש לגישור לטובת הבנת ההשפעה של המיקרו-סביבה המכאנית על תחילת הגידול, שגשוגו והתגובה לטיפול. לכן, פיתוח תיאוריה המקשרת בין שגשוג של גידול תאי ושליחת גרורות לבין חריגות ביו-מכאניות בגידול ובסביבתו, כתוצאה מהתפתחות מתמשכת של מאמצים מכאניים, הכרחי ובעל חשיבות רבה.

המטרה המרכזית של מחקר זה הינה פיתוח של כלי נומרי, מציאותי, פיסיקלי ורב-תכליתי, המבוסס על מכניקת הזורמים ונשלט על ידי משוואות Navier-Stokes, שיאפשר הדמיית תרחישים דינאמיים שונים של תאי סרטן ויספק תיאוריה המקשרת בין תופעות ביולוגיות לבין תהליכים ריאולוגיים מתמשכים המתרחשים בתוך מושבת התאים הסרטניים.

על ידי שימוש בכלי הנומרי שפותח, אנחנו מציעים תיאוריה אשר מספקת תובנה חדשה הנוגעת למנגנוני התפתחות הגידול. התיאוריה מסבירה תופעות ביולוגיות מורכבות כמו מתן עדיפות לקצב גדילה שונה עבור תאים שונים באמצעות מונחים של צמצום אנרגיה מכאנית האגורה בגידול. בנוסף המחקר המוצג מספק תובנה חדשה בנוגע למנגנון הלא מובהר של בחירת תאי ה- "leaders" ותאי ה- "followers" המתוארים בספרות, על ידי שחזור של מבנה "אצבעות", המאפיין את האזור החיצוני של הגידול, תוך שימוש בעקרון של מינימום אנרגיה מכאנית בלבד.

אוניברסיטת בן-גוריון בנגב
הפקולטה למדעי ההנדסה
המחלקה להנדסת מכונות



מודל ריאולוגי להתפתחות גידול-תאי ושליחת
גרורות

חיבור זה מהווה חלק מהדרישות לקבלת תואר מגיסטר בהנדסה

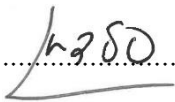
מאת : ליאב דרף

מנחה : ד"ר יורי פלדמן

תאריך : 08/06/2022

..... חתימת המחבר : 

תאריך : 08/06/2022

..... אישור המנחים : 

תאריך :

..... אישור יו"ר ועדת תואר שני מחלקתית :

יוני 2022

אוניברסיטת בן-גוריון בנגב
הפקולטה למדעי ההנדסה
המחלקה להנדסת מכונות



מודל ריאולוגי להתפתחות גידול-תאי ושליחת
גרורות

חיבור זה מהווה חלק מהדרישות לקבלת תואר מגיסטר בהנדסה

מאת : ליאב דרף

מנחה : ד"ר יורי פלדמן

יוני 2022